NASA/TP-

An Assessment of the Role of Solid Rocket Motors in the Generation of Orbital Debris

Mark Mulrooney
GB Tech, Inc.
Houston, TX

National Aeronautics and Space Administration

Johnson Space Center
Houston, TX 77058-3696

August 2004

Acknowledgments

This work would not have been possible without the generous support of Nick Johnson, Eugene Stansbery, Mark Matney, and J.-C. Liou. I also wish to thank David Yoel (Ecliptic Enterprises), Mark Tobias (ATK/Thiokol), Robert Reed (AEDC), Terry Boardman (ATK/Thiokol), and Robbie Robinson (KSC- Johnson Controls) and Greg Byrne (NASA-JSC) for supplying critical imagery data. I wish to thank Roger Boisjoly and Allan MacDonald (formerly with Morton Thiokol) for sending me in the right direction. I also wish to thank Al Jackson, Paula Krisko, Kira Jorgensen, Bill Rochelle, Phillip Anz-Meador, Lee Foster, Fred Horz, and Marilyn Garber, for their support and illuminating discussions.

Table of Contents

Acronyms

AEDC	USAF Arnold Engineering and Development Center
AMU	Atomic Mass Unit
AP	Ammonium perchlorate
ATK	Alliant Techsystems Incorporated
B.P.	Boiling Point
BSM	Booster Separation Motor
CCD	Charge-Coupled Device
CDR	Critical Design Review
DOAMS	Distant Object Attitude Measurement System
ET	[Space Shuttle] External Tank
FASP	Fly-Away-Sensor Package
fps	Frames per Second
G	Force of gravity at Earth's (fiduciary) surface (9.81 m/s^2)
GEM	Graphite Epoxy Motor
GEO	Geosynchronous Orbit
GTO	Geo Transfer Orbit
HMX	Tetramethylene tetranitamine
HTPB	Hydroxyl-terminated polybutadiene
IFR/TUBS	Institute of Flight Mechanics/Technical University of Braunschweig
IUS	Inertial Upper Stage
JANNAF	Joint Army-Navy-NASA-Air Force Interagency Committee
LDEF	Long Duration Exposure Facility
LEO	Low Earth Orbit
M.P.	Melting Point
MWIR	Mid-Wave Infrared
PBAN	Polybutadiene acrylic acid acrylonitrile
PC	Personal communication
psia	Absolute Pressure (pounds-per-square inch)
rpm	Revolutions per minute
RTI	Range-Time-Intensity
RTR	Real-Time Radiography

SEM-EDS	Scanning Electron Microscope – Energy Dispersion Spectroscopy
SICBM	Small Intercontinental ballistic missile
SRB	Solid Rocket booster
SRM	Solid Rocket Motor
SRMU	Solid Rocket Motor Upgrade

An Assessment of the Role of Solid Rocket Motors in the Generation of Orbital Debris

Mark Mulrooney

Abstract

Through an intensive collection and assimilation effort of SRM related data and resources, the author offers a resolution to the uncertainties surrounding SRM particulate generation, sufficiently so to enable a first-order incorporation of SRMs as a source term in space debris environment definition. The following five key conclusions are derived:
1) the emission of particles in the size regime of greatest concern from an orbital debris hazard perspective (D > 100 μm), and in significant quantities, occurs only during the Tail-off phase of SRM burn activity,
2) the velocity of these emissions is correspondingly small - between 0 and 100 m/s,
3) the total Tail-off emitted mass is between approximately 0.04 and 0.65% of the initial propellant mass,
4) the majority of Tail-off emissions occur during the 30 second period that begins as the chamber pressure declines below approximately 34.5 kPa (5 psia) and
5) the size distribution for the emitted particles ranges from 100 μm <D< 5cm.

I. Introduction:

Since 1958 Solid Rocket Motors (SRMs) have been employed in various configurations for orbital payload emplacement. Beginning with their use as LEO insertions stages for Vanguard 1 and 2, to their role as Perigee and Apogee Kick Motors for achieving GEO Transfer orbit (GTO) and GEO circularization, SRMs have been a mainstay of the expendable launch vehicle complement. This is also true for both re-useable and expendable launch vehicles via their role as boosters – the Space Shuttle Re-useable Solid Rocket Boosters (SRB) being a notable example of the former, Delta II Graphite Epoxy Motors (GEM) the latter. The Pegasus launch platform also uses SRMs in all three stages - the 3rd being orbital.

Although their use in expendable systems is gradually declining in favor of liquid propellant systems - where among other advantages the same stage can perform multiple roles (eg. both GTO and circularization), approximately 10-20 orbital firings still occur annually (down from a peak of 40). However since the average SRM size has trended upward, the actual amount of propellant burned and ejected annually has remained relatively unchanged (Reynolds et al., 1996). The United States remains the dominant source - historically accounting for 90% of SRM implementations, whereas the Russian Federation uses SRMs only rarely. Usage by smaller space faring nations has increased marginally due to SRM low cost and simplicity.

SRM exhaust consists of two phases – gaseous and solid particulate. The quantity, size, and relative proportion of the solid component, expressed as the time-dependent size distribution function, varies as the SRM progresses from ignition, through its main burn, to Tail-off and eventual termination. The solid propellant consists of an oxidizer (typically ammonium perchlorate (AP) or tetramethylene tetranitramine (HMX)), powdered aluminum fuel (Al), and a combustible hydrocarbon binder (eg. Polybutadiene acrylic acid acrylonitrile (PBAN) for the SRBs or Hydroxyl-terminated polybutadiene (HTPB) for the majority of smaller SRMs). These ingredients are mixed in a semi-liquid state and then cast into the rocket motor, solidifying into various predetermined configurations chosen to yield various burn rates and profiles (Figures 1 and 2). The primary combustion products are gaseous oxides of carbon (CO and $C0_2$), water vapor, and solid particulates of aluminum oxide (Al_2O_3). It is the latter solid component, which can range from sub-micron to centimeter sized particles, that is of concern from an orbital debris perspective.

II. Background

It has been known for some time that SRM effluent contributes to the orbital debris environment. Heretofore, the attention has primarily been focused on the very smallest components of the solid emissions – the main burn phase exhaust. It is also this phase that drives SRM design and consequently it is the products of this phase that are best understood. Since aluminum constitutes normally between 16 and 18 % of the propellant, its oxidation product (Al_2O_3) accounts for 30-34% of the combusted and then ejected propellant mass (based upon the molecular weights of Al and O: 27 and 16 amu respectively). Understanding the role of what can amount to several tons of solid particulate emissions per SRM firing (e.g. 3200 kg

for an Type-1 IUS (Inertial Upper Stage) SRM) has been critical to assessing the orbital debris environment.

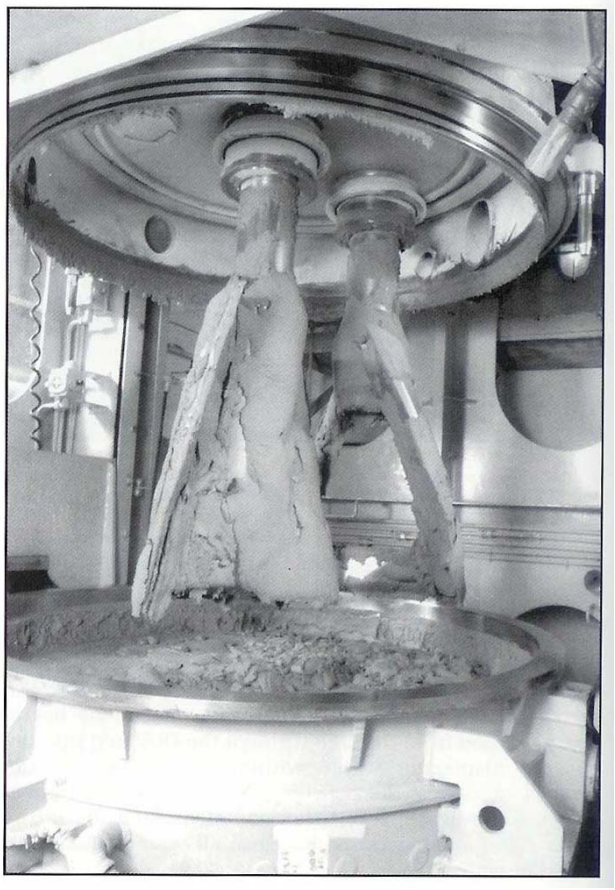

Figure 1: Solid propellant preparation. Courtesy ATK/Thiokol Photo 80110-01

Figure 2: Interior chamber of an early 260-inch diameter SRM illustrating clearly the cast propellant grains in a 3-point configuration. This SRM was a developmental prototype of the SRBs used on the Space Shuttle. Aerojet-General Photo 2-66-SP-000.

Starting with high-altitude sampling of SRM exhaust plumes by Brownlee et al. (1976) and static test collection by Girata et al. (1981), the main burn phase plumes were found to be dust-like: consisting of typically 5 um diameter Al_2O_3 spheres with aggregates as large as 35 μm. Using size data from these and other sources (Varsi 1977) with plume topology data (Burris 1978), Mueller and Kessler (1985) calculated orbital lifetimes for exhaust particles arising from apogee kick stages and found that, due primarily to solar radiation pressure, 95% of the smaller particles (D<10 μm) had orbital lifetimes of less than one year. Later, Horz et al. (1993) found Al_2O_3 residues in impact craters on LDEF's trailing surfaces (Figure 3). Kessler (1992) had attributed the parent particles to a GTO SRM exhaust population in highly eccentric orbits whose velocity near perigee exceeded that of LDEF in its nearly circular orbit – thus passing it and striking from behind. Based upon the small crater sizes (D<60 μm), the impactors were constrained in size to < 35 μm diameter - thus supporting the theory of SRM exhaust (main burn phase) as the probable causative agent.

Although early analysis indicated that only a few percent of LDEF aft impacts were specifically attributable to Al_2O_3 (most showed only Al), recent re-analysis (Horz et al. 2002) with higher sensitivity Scanning Electron Microscope – [X-Ray] Energy Dispersion Spectroscopy (SEM-EDS) attributes fully two-thirds (66%) of all trailing-edge orbital debris impact craters in the <60 μm diameter regime (< 35 μm impactor) to Al_2O_3 parent particles. Even allowing for < 1 year orbital lifetimes, this result affirms the significant contribution of the SRM main burn phase exhaust component to the micro-particle environment.

Extensive analysis of impact data from numerous space shuttle missions is also consistent not only with a SRM small particulate exhaust source but also with larger Al_2O_3 impactors which could also arise from SRMs but via a different physical process. STS-73 in particular suffered Al_2O_3 impacts from particles large enough to generate craters as large as 3.4 mm diameter (Bernhard and Christiansen, 1995). Ground based radar (Stansbery et al., 1996) and optical observations corroborate the existence of a large population of small (1mm<D< 1 cm) particles for which no source term is rigorously ascribed. Physical mechanisms which occur within SRMs at the conclusion of their main burn can generate particles within this size regime and in sufficient quantity to partially account for the observed small particle environment. It is the nature of these particles and the process of their generation that is the focus of this investigation.

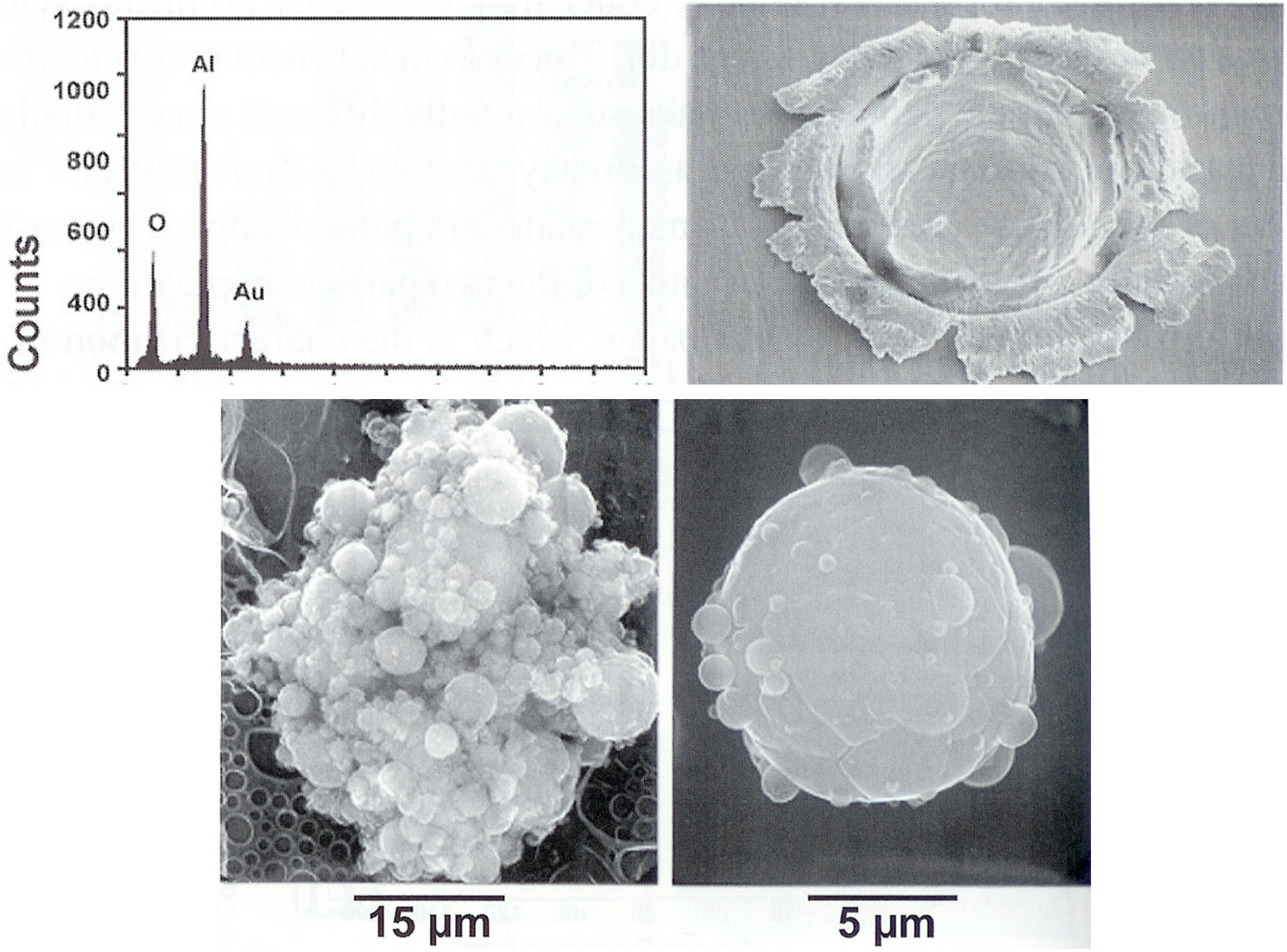

Figure 3. (Top) An LDEF trailing-surface impact crater (D=9 µm) on a gold substrate with a high oxygen and aluminum (Al_2O_3) content as determined by newer SEM-EDS methods. (Bottom) SRM dust-like exhaust particles from the main burn phase. Particles like these caused the impact above. (Horz et al. 2002).

III. Mechanisms of SRM Particulate Generation:

A. Propellant Combustion –

During an SRM main burn, chamber pressures are typically 5.5-6.9 MPa (800-1000 psia), temperatures are of order 3000 ^{o}K (5500 ^{o}F), and nozzle exit velocities are 2-3 km/s. These temperatures and pressures arise from the oxidation reaction of both aluminum and polymerized hydrocarbons with the oxidizer. As seen in Figure 4, obtained via micro-cinematography, the reacting propellant particles are continuously liberated from the grain surface. Hydrocarbon binder oxidation (pyrolysis) produces gaseous CO_2, CO and H_2O and aluminum combustion (in the form of 50-500 μm diameter agglomerate complexes) produces solid particulates of various sizes (Figure 5). These processes taken together generate the high temperature and consequently high chamber pressure which concurrently entrains the particles in the high speed flow exiting the nozzle. Importantly, because shearing forces at the nozzle throat greatly exceed the surface tension of the large aluminum agglomerates, they are shattered and disrupted upon exit. The resultant size distribution of main burn phase exhaust particles is small with a maximum cut-off diameter of approximately 100 μm.

To understand in more detail the processes which lead to the formation of particulates in an SRM it is necessary to follow closely the evolution of the aluminum component of the propellant. Aluminum combustion in an SRM is a complicated process which includes six steps: aluminum accumulation, aluminum agglomeration, ignition, condensed phase oxidation, vapor phase oxidation and droplet shedding. Figure 6 illustrates the four spatial regions associated with the progression of an aluminum particle from its initial liberation from the propellant surface (Region 1: Agglomeration), to entrainment in the chamber flow (Region 2: Oxidation), to nozzle entrance (Region 3: Disruption/Coalescence) to nozzle exit (Region 4: Cooling/Solidification). These processes in their entirety transform the aluminum component of the propellant into a bimodal log-normal size distribution of Al_2O_3 particulates. Specifically, the aluminum is concurrently oxidized to form several classes of particles with distinct sizes. Figure 7 illustrates the complex properties associated with one of the burning aluminum particles as it leaves the burning propellant and traverses the first two regions. The particle

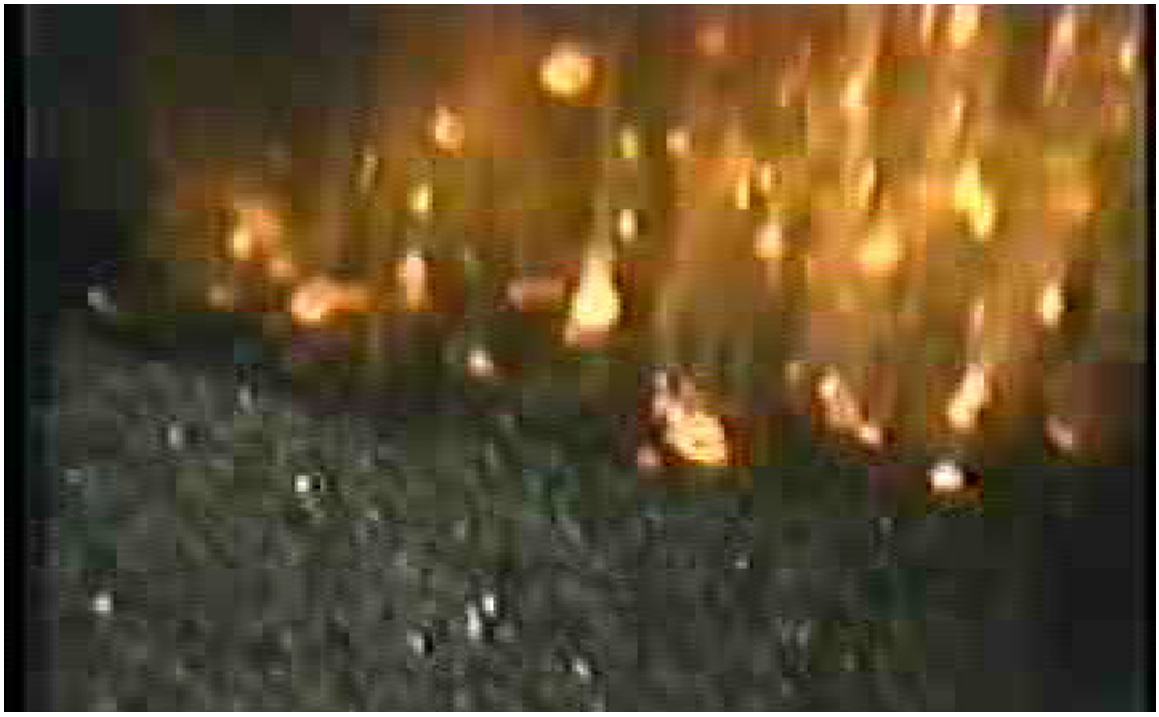

Figure 4. Image from high speed film of SRM burning propellant grain (19% Al, HTPB, AP). Agglomerates of approximately 50-500 μm diameter are continuously liberated from the surface and then entrained in the flow exiting the nozzle. (United Technologies).

Figure 5. Dual Plumes. Pyrolysis gas and large (D>500 μm) solid particulates are easily distinguished in this Tail-off image from an STS-103 in-situ camera. Differential atmospheric drag has separated the plumes according to area-to-mass ratios. During static ground testing, the two components are not visually differentiated.

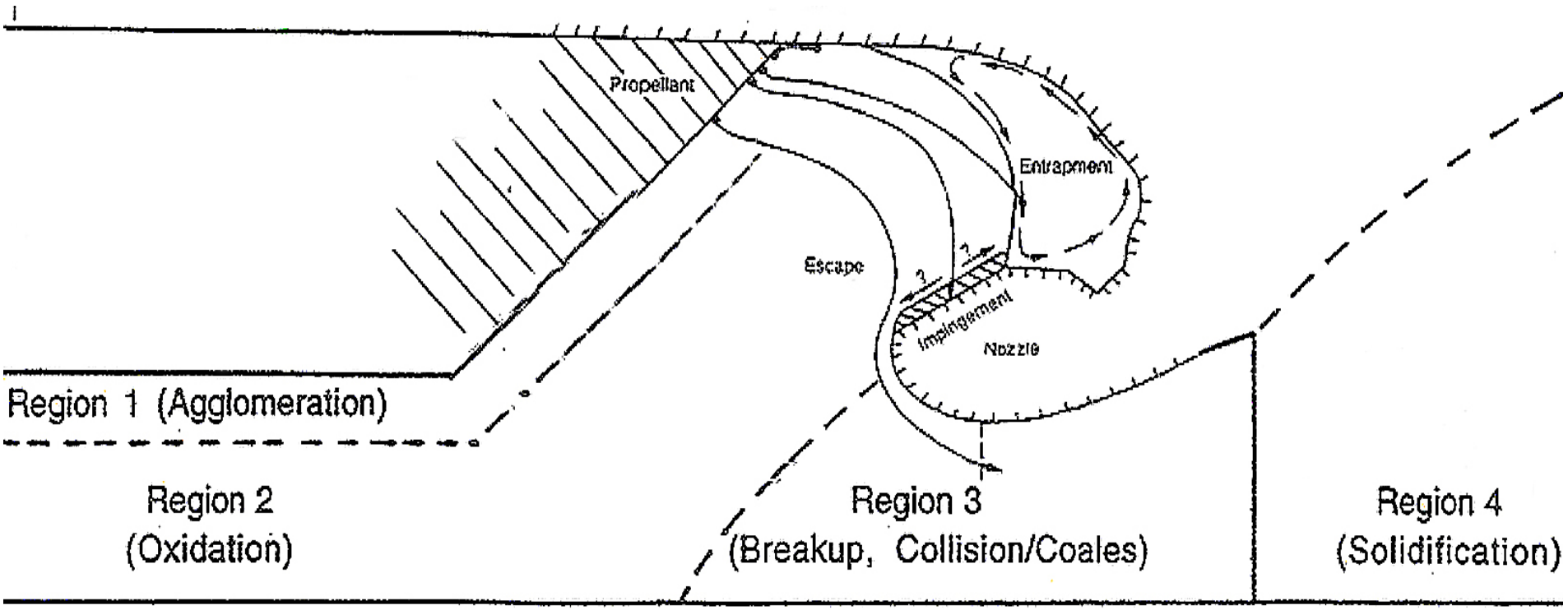

Figure 6. The four primary regions associated with the progression of an aluminum particle from its initial liberation from the propellant surface (Region 1: Agglomeration), to entrainment in the chamber flow (Region 2: Oxidation), to nozzle entrance (Region 3: Disruption/Coalescence) to nozzle exit (Region 4: Cooling/Solidification). (Salita 1994, 1995)

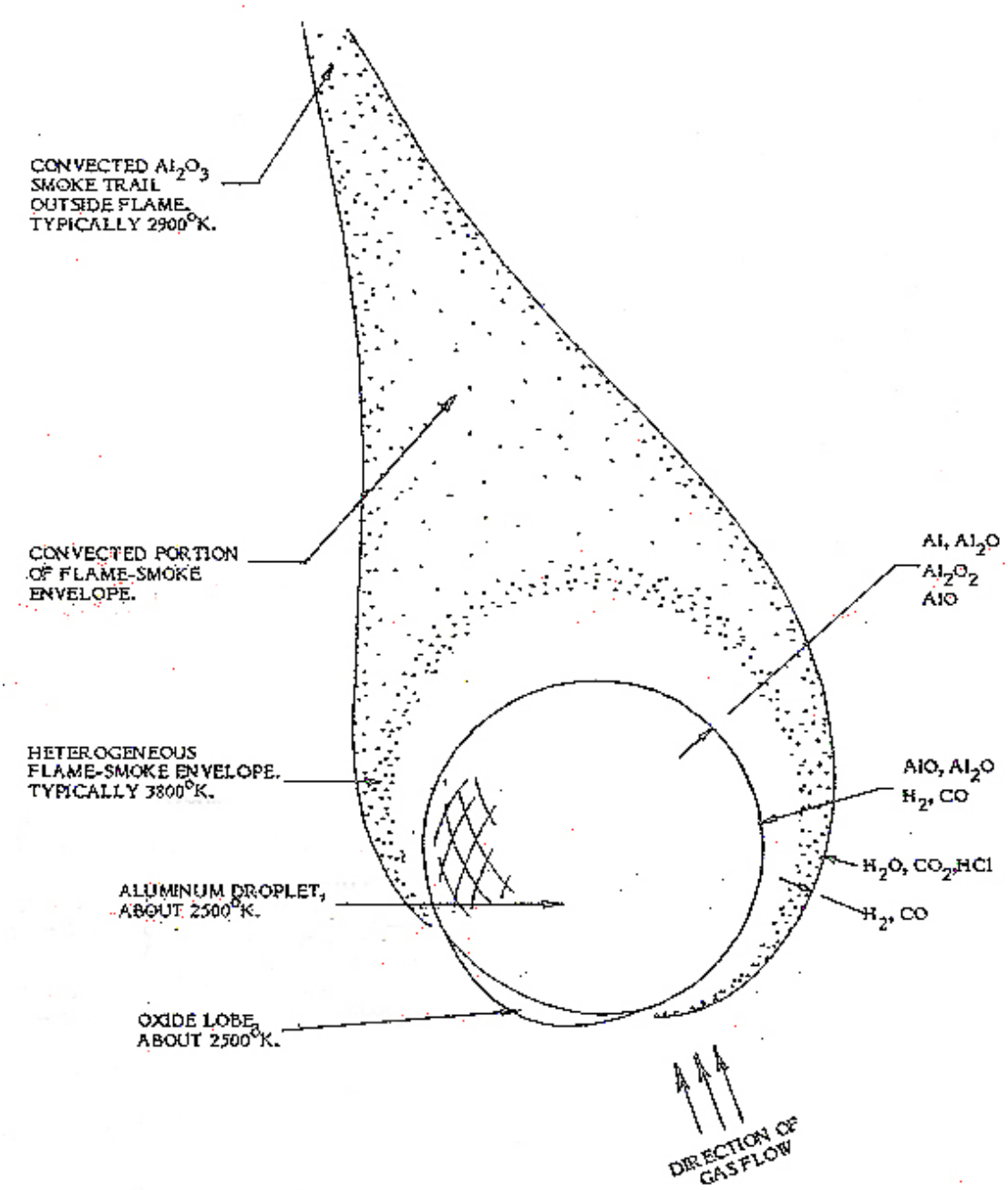

Figure 7. Detailed schematic of the morphology of a burning Aluminum Agglomerate. The oxide envelope, comprised of dust-like ($0.1<D<100$ μm) particles is continually swept away by the exhaust flow and exits the nozzle giving rise the plume's characteristic white color. The aluminum droplet is gradually consumed by oxidation unless it and its oxide cap (or lobe) are either trapped or escape intact as described in the text. (Price and Sigman 1994.)

itself, an agglomerate at this stage, is typically 50-500 μm diameter and its dominant feature is the oxide smoke liberated from it as it burns. This oxide is the primary combustion product and is comprised of extremely fine alumina dust which exits the nozzle generally unhindered and is responsible for the bright white plume seen emanating from SRMs – the most notable example being the large and persistent Space Shuttle SRB plumes. The dust is typically an ensemble of 0.1-10 μm diameter particles. Despite the fact that it constitutes 30-35% of the initial propellant mass, it is not a significant orbital debris hazard (although it can be a source of surface erosion), and its high area-to-mass ratio give it generally short orbital lifetimes (eg,. < 1 year for GTO stages).

In addition to the oxide smoke, there are oxidized regions of the agglomerates which are much larger. These regions are called caps or lobes and represent areas undergoing oxidation but which do not stream from the agglomerate like the oxide. These caps may survive the disruption, collision, and coalescing process which occurs in Region 3 and may be responsible for the somewhat large particulates that are measured in SRM main phase plumes. Although their diameters while resident in the SRM chamber are 50-500 μm, main phase disruption reduces them to an approximately 100 μm diameter maximum exhaust size – still small by orbital debris standards.

Main burn phase exhaust particles have been collected in numerous, high-altitude samplings, ground tests, including quench bomb fuel burns, and their distribution is well documented (Brownlee et al., 1976; Chuan and Woods, 1977; Cofer et al., 1978; Girata et al., 1981, Price and Sigman, 1994; Salita 1995). In the space environment, it is particles with the smaller signature that struck LDEF's trailing surfaces. Because of their small size, these particulates do not pose a significant orbital debris threat.

Although SRM thrust may be tailored somewhat by varying the propellant geometry, the main burn phase is characterized by a high chamber pressure maintained within a stable range. The particle efflux arising directly from propellant combustion is thus fairly predictable – it is distributed amongst a range of very small sizes. As the propellant nears exhaustion however, the burning surface area diminishes quite rapidly and consequently the chamber pressure drops precipitously. This phase of the SRM burn is called Tail-off and within it chamber pressures decline from >3.5 MPa (>500 psia) to that of the ambient environment within a few seconds. When this occurs, the large agglomerates, which are normally disrupted by high shearing forces during nozzle passage, are able exit the SRM intact. Consequently, during Tail-off burning, SRMs produce

particles ranging from oxide smoke to intact agglomerates with a corresponding size range from 0.1 to 500 μm (Reed 1997). Additionally, because the agglomerates can cool more rapidly in the Tail-off environment, they do not necessarily fully oxidize and therefore Tail-off exhaust can contain small amounts of elemental aluminum (Al) in addition to the normal Al_2O_3. Particles at the upper end of this range (500 μm) could be considered a minor orbital debris hazard to astronauts and some spacecraft.

It is important to note that the aforementioned analysis should be adjusted somewhat to include spin-stabilized SRMs. While the oxide smoke emissions are unaffected, the large caps may be driven outward to the chamber walls by centrifugal force (e.g. 2 Gs for a 1 m diameter motor spinning at 60 rpm), thus reducing their ability to escape through the nozzle. SRM spin probably plays the largest inhibitory role during Tail-off where large agglomerates that would otherwise be liberated are captured. This is corroborated by aluminum oxide slag accumulation versus spin rate measurements (Salita 1995) which shows dramatic increases in residual slag content with increasing motor spin in static ground tests (Section VI.) Specifically additional slag accumulates due to the capture of agglomerates that would otherwise escape. The issue of SRM slag accumulation is critical to understanding the orbital debris hazard posed by SRMs and is addressed in the following section.

Along with Tail-off propellant derived emissions, there are also portions of the SRM chamber liner which burn when exposed to the high chamber temperatures by the retreating propellant grain (Kavanaugh and Nichols 1980). The extent to which this occurs is subject to the vagaries of SRM materials and construction techniques and as such varies widely and is difficult to assess. The contribution of this material to the orbital debris environment is believed minimal – based both upon the fact that it constitutes a small portion of the SRM total mass and the general absence of its signature in impact studies and static or in-situ plume imagery.

B. Slag Generation and Emission -

SRMs are generally designed to yield a smooth thrust profile with maximum integrated impulse within as compact and efficient a package as possible. Although the burn rate may to tailored to provide variable thrust (eg. Space Shuttle SRB thrust is decreased during maximum dynamic pressure), it is imperative that output be well-behaved - absent any anomalous pressure pulses or deficits. With this unanimity of focus, engineers optimize those performance

parameters associated solely with the main phase of the SRM burn. What occurs after this phase has generally been considered ancillary and of marginal interest from a design perspective. Consequently behaviors can and are introduced which are undesirable from an orbital debris perspective. Specifically, the almost ubiquitous use of re-entrant or immersion nozzles, wherein thrust continuity is improved and motor length is reduced by moving the forward end of the motor nozzle well inside the motor chamber, has deleterious consequences.

In the immersion nozzle design, the point where the nozzle nosetip penetrates the combustion chamber is surrounded by a toroidal shaped volume which acts as a catchment basin that entraps burning propellant particles in the aft end of the SRM. The resultant flow of dual-phase exhaust gas and particulates into and out of this reservoir has been extensively modeled in the viscous and inviscid regimes and is well documented (Salita 1995). While the re-entrant nozzle does inhibit the ability of large condensates to exit the nozzle intact (and thereby reduces pressure pulsing), the resultant circulation zone enables the accumulation of molten aluminum oxide and unburned aluminum in the form of slag around the nozzle (Figure 8). Based on empirical measurements acquired via dozens of static ground tests (Salita 1995), the resultant slag pool can collect between 0.12 and 1.9% of the Al_2O_3 emissions - corresponding to between 0.04 and 0.65% of the initial propellant mass. For a large SRM such as the Titan IV boosters, this can amount to a mass of 2000 kg and a volume of roughly 1100 liters (40 cubic feet). The slag pool is readily and consistently measured in static-ground tests (after quenching) for all re-entrant style SRMs as a solid annular slug of material (Figure 9). It is important to emphasize that although the degree of accumulation varies wildly (even for SRMs of the same type) for reasons which are still not understood, the accumulation of slag is ubiquitous - regardless of SRM orientation relative to the gravity vector – indicating recirculation zone hydrodynamic processes dominate.

SRM design is a delicate compromise between slag accumulation and thrust continuity. Immersing the nozzle creates an impingement zone which inhibits large agglomerates from escaping and creating pressure oscillations, but as a corollary, the accumulated slag reduces SRM specific impulse by representing an excess load and lost propellant conversion efficiency. In fact for some flight tests it is via telemetry that slag accumulation has been assessed by comparing the deviation between the actual track and that predicted in the absence of slag formation. The sloshing slag pool has also been identified as the likely cause of large coning errors in some spin-stabilized SRMs. Overall the trade-off in terms of performance and motor size reduction appears to favor the immersion design,

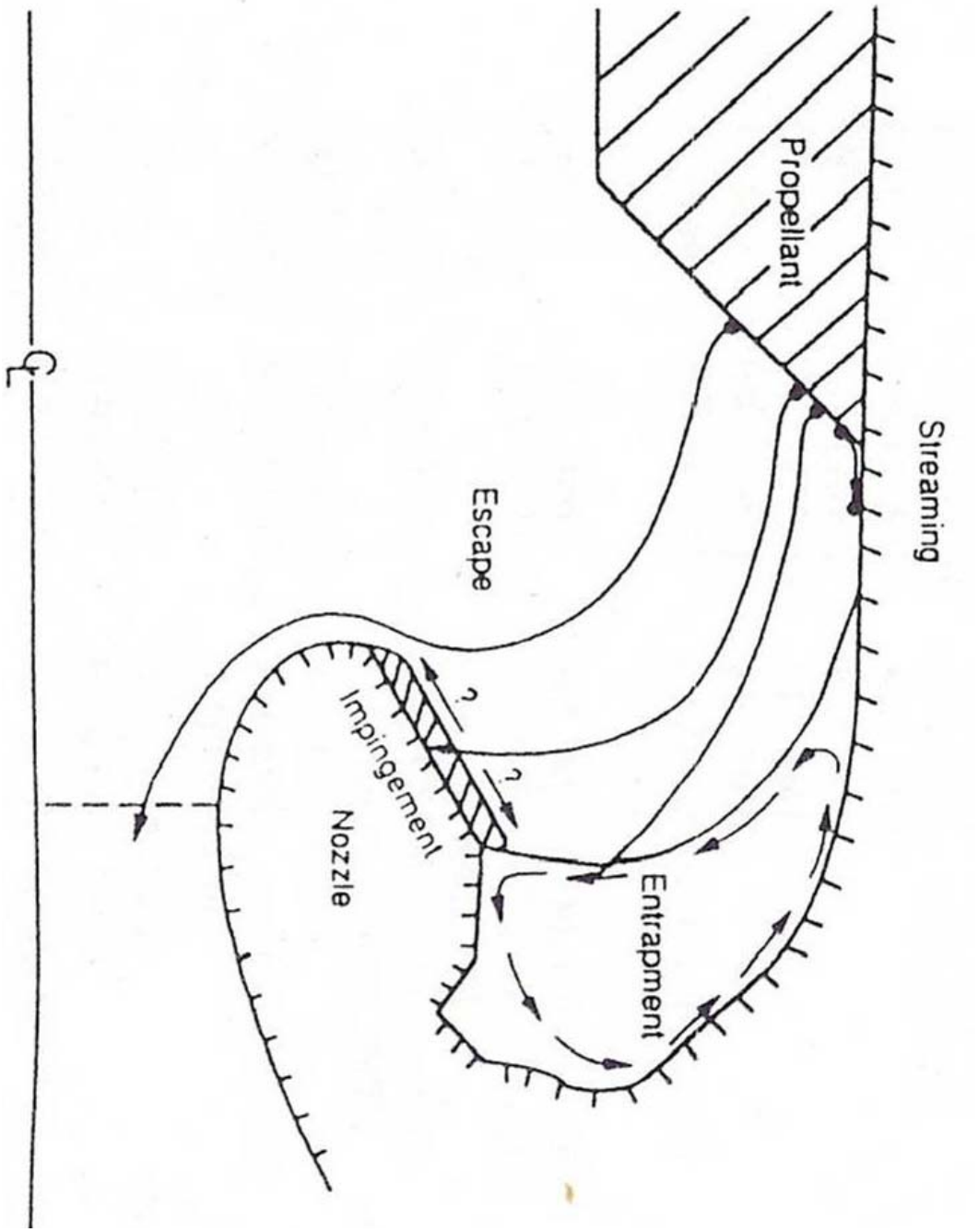

Figure 8. Streamlines illustrating the trajectory of combustion gas and burning aluminum agglomerates. Most particles escape the chamber unhindered, while others impinge on the walls, interior portion of the nozzle, or enter the circulation zone in the immersion reservoir. The net result is the formation of a slag pool which accumulates from the start of the main burn phase. (Salita 1995).

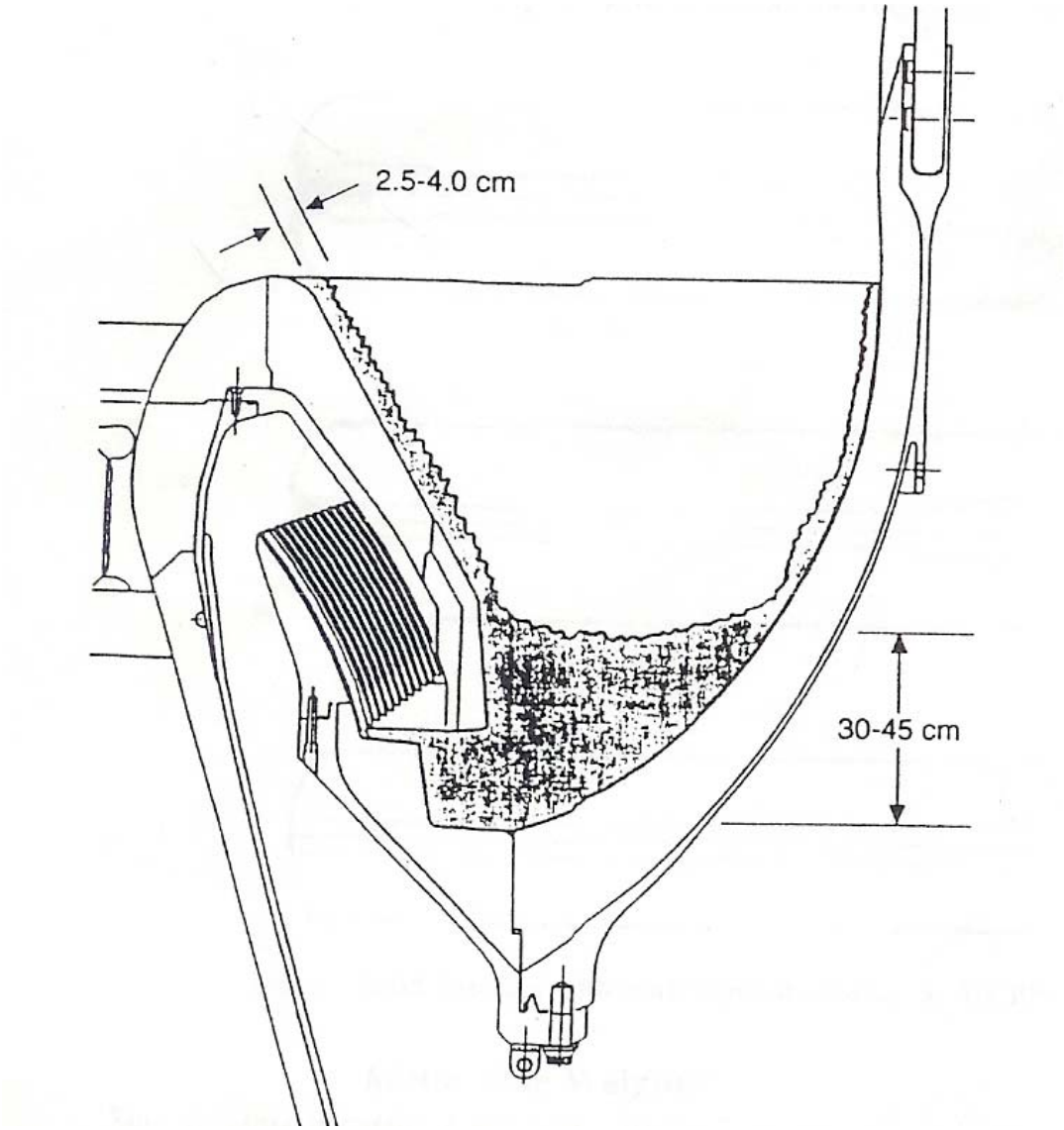

Figure 9. Cross-sectional view illustrating the solidified Al_2O_3 slag generated in a SRB during a static test. The slag mass was 0.6% of the available propellant mass. A similar result is found for essentially all static SRM tests which are conducted at atmospheric pressure – and regardless of SRM orientation. (Salita 1995).

however from an orbital debris perspective the residual slag represents the primary source term for the generation of objects of sufficient size and quantity to qualify as an orbital debris hazard. Although the detailed mechanism of ejection is still being researched, the preponderance of available evidence indicates that in space firings the accumulated slag is ultimately liberated from SRMs in the form of numerous 100 μm to 5 cm diameter debris objects.

From a space environment standpoint there are two identifiable processes by which slag is transformed into orbital debris. The first involves the loss of slag during the SRM main burn phase due to the onset of instabilities in the slag pool. The second occurs during the Tail-off phase and is due to boil-over of the slag pool in the ambient low pressure Tail-off environment. The support for these particulate generation mechanisms and their regimes of operation come from a variety of sources including theoretical modeling, static ground-test imagery (vacuum and non-vacuum, covering all spectral regions from X-Ray through Infrared (IR)), static ground-test particle collection, ground-based imagery of sub-orbital SRM firings, and in-situ imagery of sub-orbital and orbital insertion SRMs.

Beginning with Real Time [X-Ray] Radiography (RTR), the behavior of the slag pool within the SRM chamber itself has been studied extensively during static-ground tests. Figures 10 and 11 illustrate the gradual accumulation of slag as the main burn progressed for two SRMs – a large Titan IV Booster SRMU (QM-2) and a moderate SICBM (DS-8). The data, which is comparable to numerous other examples, show a roughly linear increase in the volume of the pool for the first 75% of the main burn (or action time). A volumetric plateau is then reached wherein 20-30% of the available immersion space is filled. This stasis persists for the remaining 25% of the action time and then subsequently, at the initiation of the Tail-off phase, there is a rapid twofold increase in volume of the pool to approximately 55% of the available volume. This expanded state persists for a few seconds and then the pool begins to collapse toward its former state. The duration of the cycle correlates with the size of the slag pool, being greater for larger residual slag mass (or volume). It is important to note that current models can accurately predict all aspects of accumulation and Tail-off expansion, but do not predict the plateau formation and therefore it is the subject of some debate.

Both the plateau formation and expansion/contraction behavior of the slag pool each have consequences for the generation of orbital debris. The plateau in pool volume may be due to slag loss via vortex streaming up the side walls, to diminution of the zone of

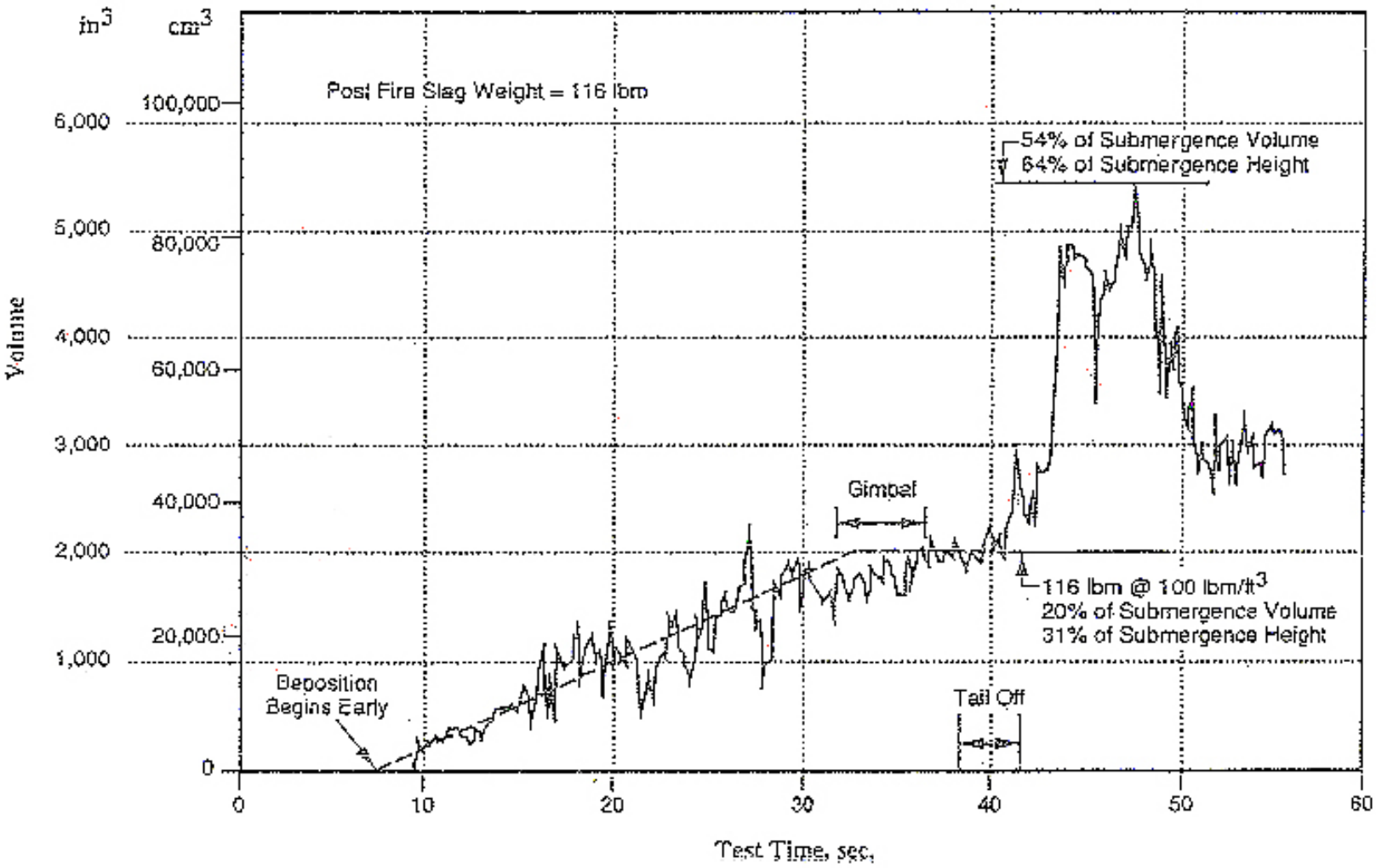

Figure 10. Time history of slag pool volume growth from RTR of vertically fired SICBM (DS-8) with a 11,300 kg propellant mass. Linear growth until approximately 75% of the action time is evident as is the rapid expansion at Tail-off due to boiling. (Salita, 1995)

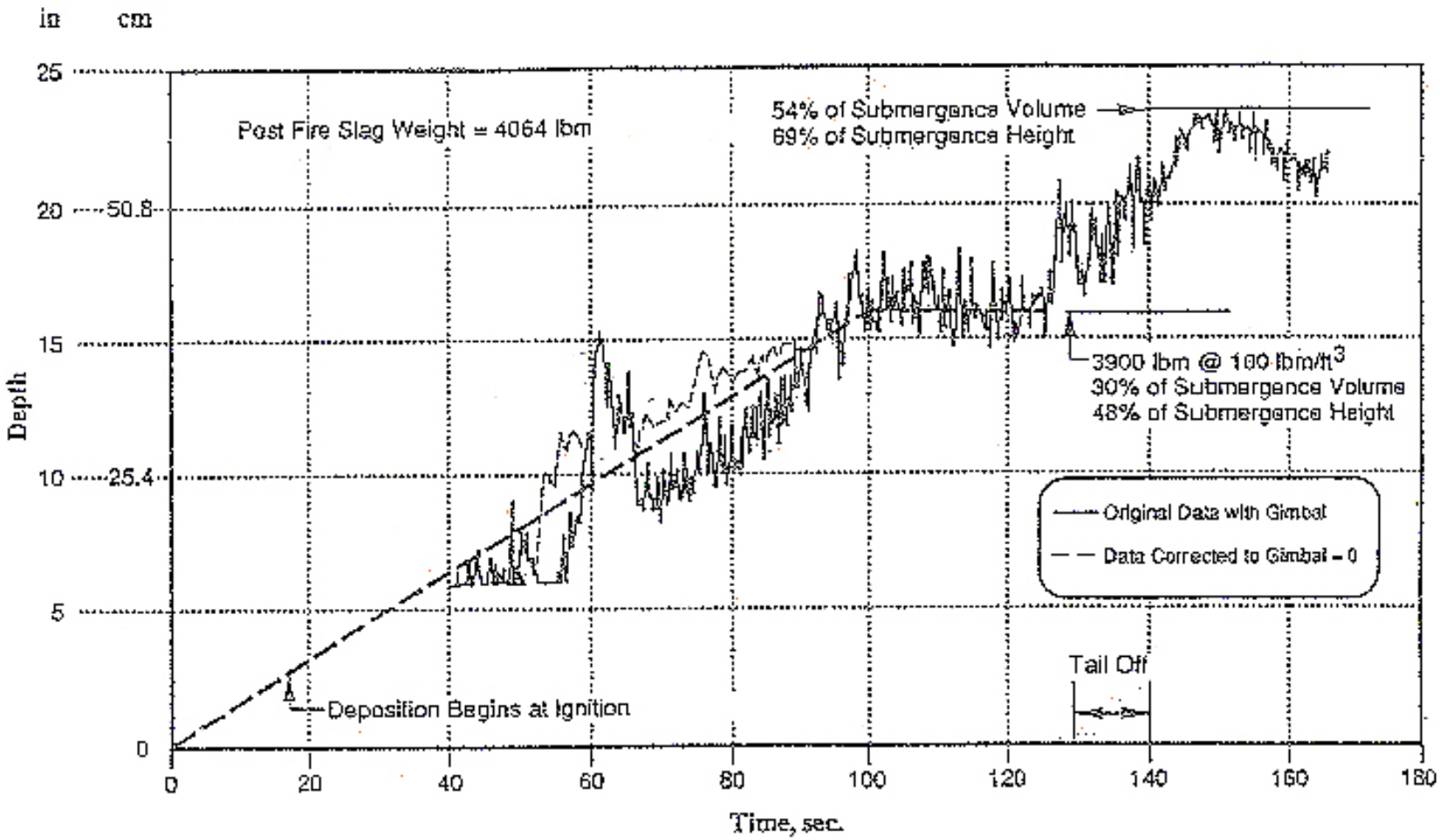

Figure 11. Time history of slag pool volume growth from RTR of vertically fired Titan IV Booster SRMU (QM-2) with a 318,000 kg propellant mass. Linear growth until approximately 75% of the action time is evident as is the plateau and then rapid expansion at Tail-off due to boiling. Despite the factor of thirty variation in size relative to DS-8 (Figure 10), the same behavior is observed. (Salita, 1995).

re-circulation (and thus loss of capture efficiency), or it may be due to an ejection/deposition process wherein slag is continually depleted by ejection from the nozzle and replenished by fresh capture and deposition. Evidence for the latter scenario comes in the form of some RTR observations which appear to show portions of accumulated slag entering the nozzle during the main burn (Reed PC 1991). If the surface of the slag grows sufficiently high, instabilities (eg. Rayleigh-Taylor) might be able to arise in the pool and slugs of molten material could be swept from the surface, over the nosetip, and exit the nozzle. This does not occur in all RTR SRM imagery (which is considered difficult to visually interpret), and the extent to which this phenomenon occurs in space firings (if at all) is difficult to assess and has not been quantified. The large axial forces (10+ G) experienced by the slag pool during a space firing should act to inhibit the instability by suppressing wave growth and impeding the upward movement of slag material.

Nonetheless, if slag does enter the nozzle during the main burn, it will issue forth as solid particulates. Although it is still subject to high dynamic shearing forces which disrupt the material, the distribution contains sizes that are almost certainly larger than the normal main burn exhaust particulates because shearing forces cannot shatter bulk macroscopic slag samples as effectively as small agglomerates. The high-altitude sampling reported in the literature does not reveal any measurable large particulates (D>500 μm), so if they occur they are almost certainly infrequent. Additionally, because of the tremendous disruption these bulk emissions would cause to the thrust profile of the main burn, it is reasonable to assume that this phenomenon is extremely rare. While large anomalous thrust discontinuities occur, (eg. STS-54 experienced a 110 kPa (16 psia) pressure pulse between 67.0 and 67.8 seconds into flight which has been postulated to have been due to slag ejection momentarily obstructing a small portion of the nozzle) they are infrequent and therefore bulk main burn phase slag emission probably does not occur with sufficient frequency to constitute a measurable orbital debris threat.

Unlike the plateau phenomenon the Tail-off expansion behavior is indicative of another physical process which has much more serious consequences for orbital debris generation. The observed expansion is consistent with the idea that the rapidly decompressing Tail-off environment of the SRM chamber is initiating the onset of boiling in the slag pool. Under such a scenario slag can be readily liberated from the pool and ejected from the SRM either by being swept up in the outflow or by simple diffusion and

scattering. A general consensus that slag was ejected at Tail-off by boiling related processes was reached as early as 1994 (Salita 1994).

The ejected mass depends on the extent to which the slag pool has been disseminated by boiling. To evaluate this for various scenarios consideration must be given to the pressure and temperature within the chamber and the vapor pressure of the slag (neglecting to first order gas infusion and pure aluminum content). During the main burn phase of an SRM, the chamber temperature (flame temperature of the combusting propellant) is of order 3300 ^{o}K and the chamber pressure is normally >4.1 MPa (>600 psia). Under these conditions the boiling point (B.P.) for pure Al_2O_3 is much greater than 4000 ^{o}K and therefore, as is generally accepted, boiling is probably not occurring (although trapped gasses my be continually infused and effused). As the Tail-off phase begins however the chamber pressure declines precipitously and the temperature gradually. At approximately 138 kPa (20 psia), the boiling point of Al_2O_3 is now near 3300 ^{o}K and boiling can commence. But because this process lowers the chamber temperature via the heat of Al_2O_3 vaporization (there is only a finite reservoir of heat from which to draw), boiling is limited if the chamber pressure has a lower bound. In a static-ground test, conducted at local atmospheric, that lower bound is typically 90-101 kPa (13-14.7 psia; corresponding to a B.P. of 3000 ^{o}K) and boiling is necessarily brief and incomplete. Specifically, the loss of heat due to vaporization quickly drops the chamber temperature below 3000 ^{o}K and boiling is halted within a few seconds. While some particles may be emitted during the brief episode, all available evidence shows that the loss is small. For static-ground tests RTR, measurements of main phase accumulated slag normally agree with post-firing solidified slag pool measurements – indicating no significant loss between main burn and termination.

For a space firing the situation is quite different. There is no lower bound on the chamber pressure so the boiling process can continue unabated. Termination only occurs when the chamber temperature declines below approximately 2300 ^{o}K (Al_2O_3 solidification and vapor pressure is negligible), by which time much or all of the slag has boiled. A wealth of empirical evidence indicates that by the time the chamber pressure has declined to below 6.9 kPa (1 psia), the slag pool has boiled, its contents have spread throughout the chamber, and they have begun to diffuse out the nozzle. Because in the low pressure Tail-off environment these particles are not subject to shearing forces (and may already have cooled below the melting point), they leave the SRM undisrupted and can be of very large (cm) size. Unlike any of the ejection mechanisms described previously, this mode of SRM

particle generation is capable of producing very large quantities (>10^5 per event) of orbital debris in a size range (500 μm <D<5cm) which poses a significant debris hazard.

IV. Evidence Supporting Tail-off Vacuum Emission Scenario:

Based upon both physical arguments and empirical evidence there is general agreement within the propulsion community that large Tail-off slag ejections are occurring under vacuum conditions. There is also general consensus that static-ground tests do not accurately emulate space firings (unless conducted in vacuum) and therefore ground-test data while useful is limited in its applicability. From an orbital debris perspective, the major identifiable difference between static and space/vacuum conditions is in the manner which slag accumulates and is retained or ejected. Consequently the size distribution function cannot be accurately assessed by a static-ground test unless conducted under vacuum conditions. Assembled below is a collection of specific examples assembled by the author to support these conclusions.

A. SRB Data: Static-Ground Tests at Atmospheric Pressure –

Among several data acquisition strategies available for the investigation of SRM emissions, ground tests can provide insight into the operative physical mechanisms. Interpretation of the data must be tempered however by recognizing that there are fundamental differences between the operating environment of an orbital or sub-orbital SRM and that of a static test. The effects on a space motor of axial acceleration and deceleration are not emulated in ground testing, nor is the vacuum environment normally duplicated. Despite these differences, ground tests can provide useful data about SRM behavior which can be applied by extension to space motor events. As already discussed, ground based RTR data has elucidated the probable response of SRMs to vacuum conditions. Additionally, measurements of residual slag as a percentage of initial propellant mass give an estimate of the available material for orbital debris generation. Calculations of oxide dust and of aluminum agglomerate size distributions are also generally applicable to space events.

The static test images that follow (Figures 12-17) were selected from various static Space Shuttle SRB tests conducted by ATK/Thiokol (formerly Morton Thiokol). The first two figures are optical images acquired from viewpoints orthogonal to the plume and along

the rocket body facing aft. Saturation in the first two frames of Figure 12 prevents any qualitative assessment and they are only supplied to be illustrative. The last frame of Figure 12 however is particularly interesting because it clearly shows the hot gaseous Tail-off plume billowing upwards but is absent any visible solid ejecta (which would appear as streaming embers following roughly horizontal trajectories). The last frame of Figure 13 is also absent any obvious Tail-off ejecta.

Figures 14-17 are infrared images exactly analogous to the optical images described above. They are unsaturated and show the full dynamic range of the plume – from the coolest portions near 780 ^{o}C (1400 ^{o}F) to the hottest at 1800 ^{o}C (3250 ^{o}F). The sequence progresses from the main burn phase – where the plume is relatively cool and laminar (Figure 14) – to the Tail-off phase – where chamber pressures decline and the plume begins to become hot and turbulent (Figure 15). Figure 16, acquired in Tail-off with a chamber pressure near atmospheric, shows the same billowing gaseous plume seen optically in Figure 12. Notably absent from this and Figure 17 are any Tail-off emissions – which should appear as luminous ensembles with horizontal or downward trajectories.

With the exception of one small low temperature object, which appears to exit near the end of Tail-off, there are no particulate emissions visible in any portion of the parent video sequence and thus no evidence of slag ejection. Despite the coarse spatial resolution, the high IR luminosity of Tail-off ejecta would make them appear as bright red or yellow luminous masses. This IR luminosity derives from the fact that they exit quickly and generally unencumbered and thus they sample the 2700+ ^{o}C SRM chamber directly. The appearance of the low luminosity object is interesting, but its temperature of approximately 350 ^{o}C (650 ^{o}F) indicates it probably did not emanate from within the SRM chamber and thus is not slag.

It is known categorically that SRBs emit prodigious quantities of particulates during Tail-off at altitude - wherein the pressure of the ambient environment at SRB separation (50 km altitude) is just 76 Pa (0.011 psia) . However there is no evidence in any of the acquired static ground tests imagery of significant Tail-off emissions in any SRB static test (or those of two there SRM tests investigated). This result is entirely consistent with the idea expressed earlier – in non-vacuum conditions, slag boiling is curtailed and significant slag ejection is not possible. This behavior underscores a fundamental phenomenological difference between testing at atmospheric pressure and that of vacuum and thus the care which must be exercised in drawing universal conclusions from the results of SRM static tests.

Figure 12. Optical imagery of Static SRB test. Slag expulsion is not evident at Tail-off (last frame). (Thiokol Photos).

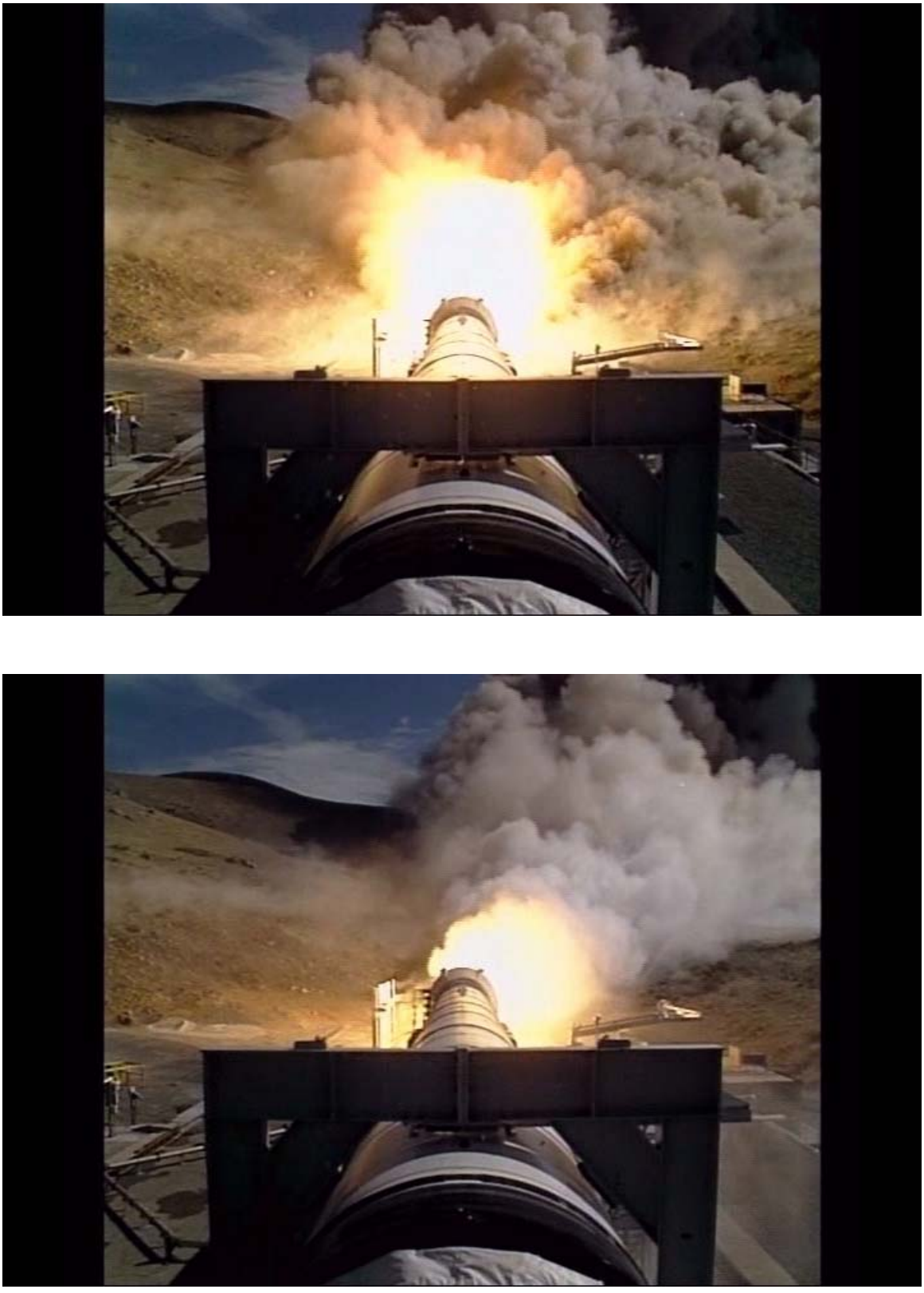

Figures 13. Optical imagery of Static SRB test (facing aft). Slag expulsion is not evident at Tail-off (lower frame). (Thiokol Photos).

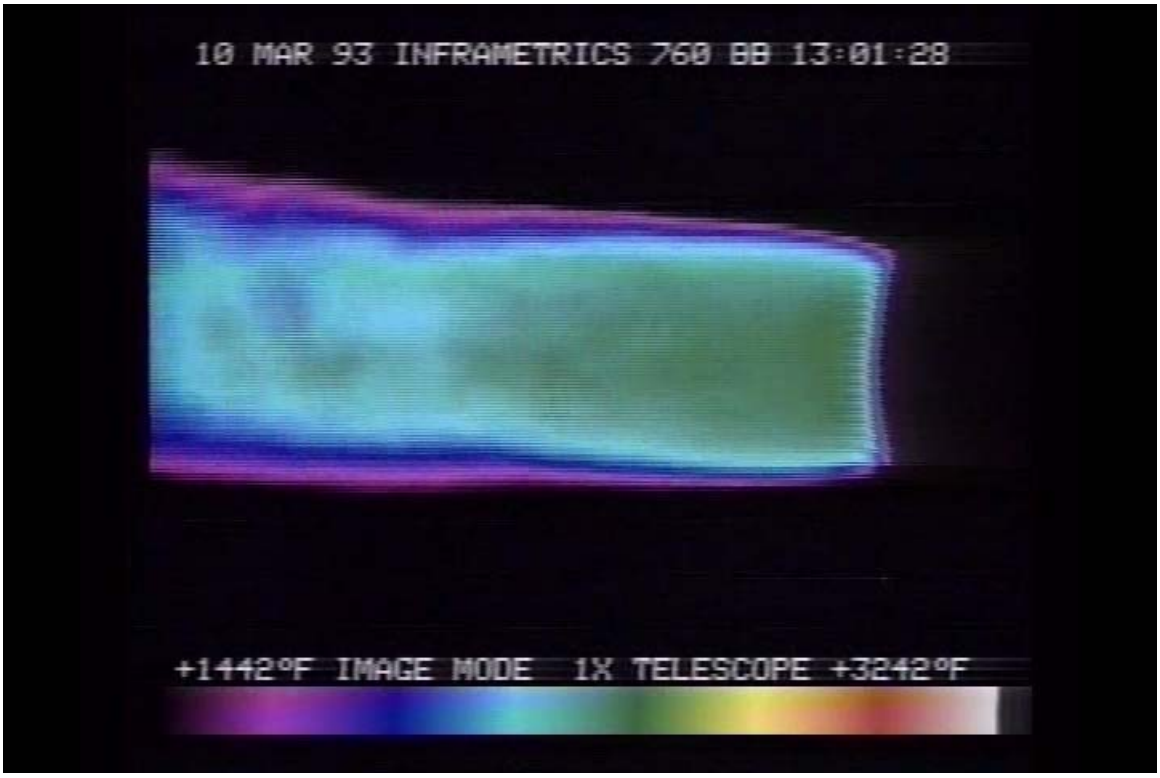

Figure 14. IR imagery of SRB (non-vacuum) Static test. Main burn phase - rapid expansion at the nozzle results in a relatively cool laminar plume (~2500F). (Thiokol).

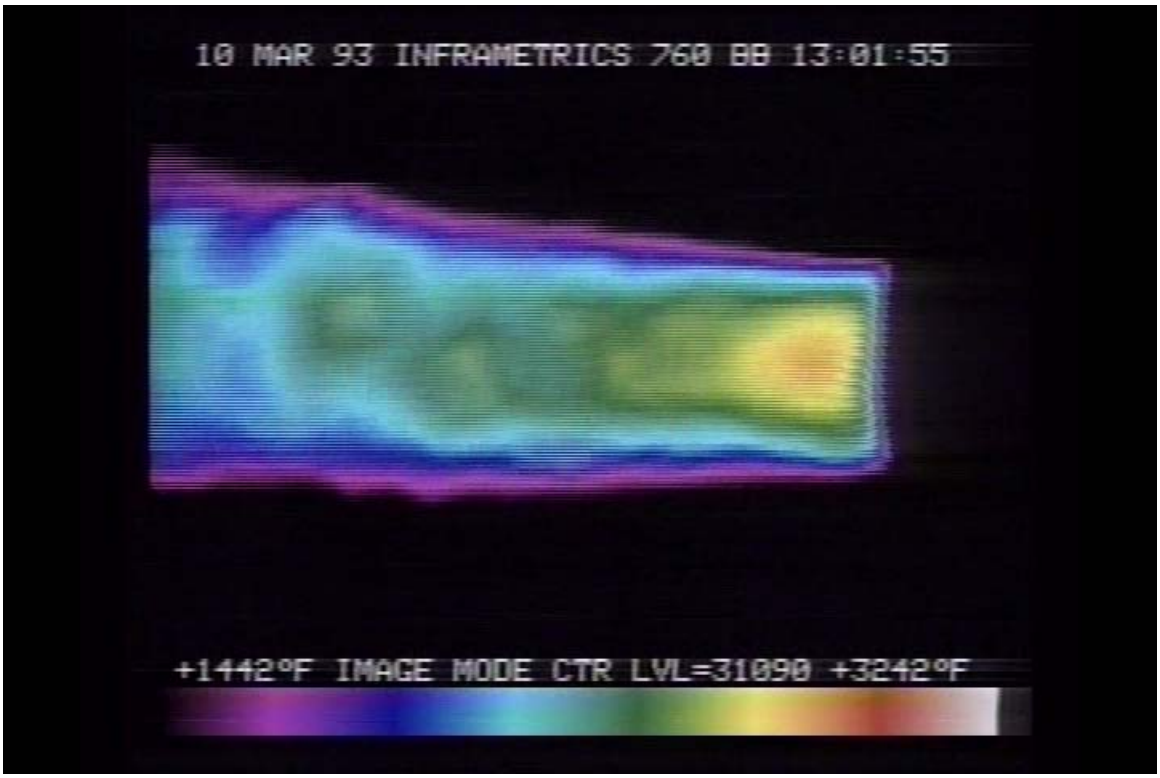

Figure 15. SRB Static test (non-vacuum) - beginning of Tail-off phase (ie. declining chamber pressure) revealed by turbulent flow and less expansive plume resulting in higher plume temp (~3000F). No solid particulates are discernable. (Thiokol photo).

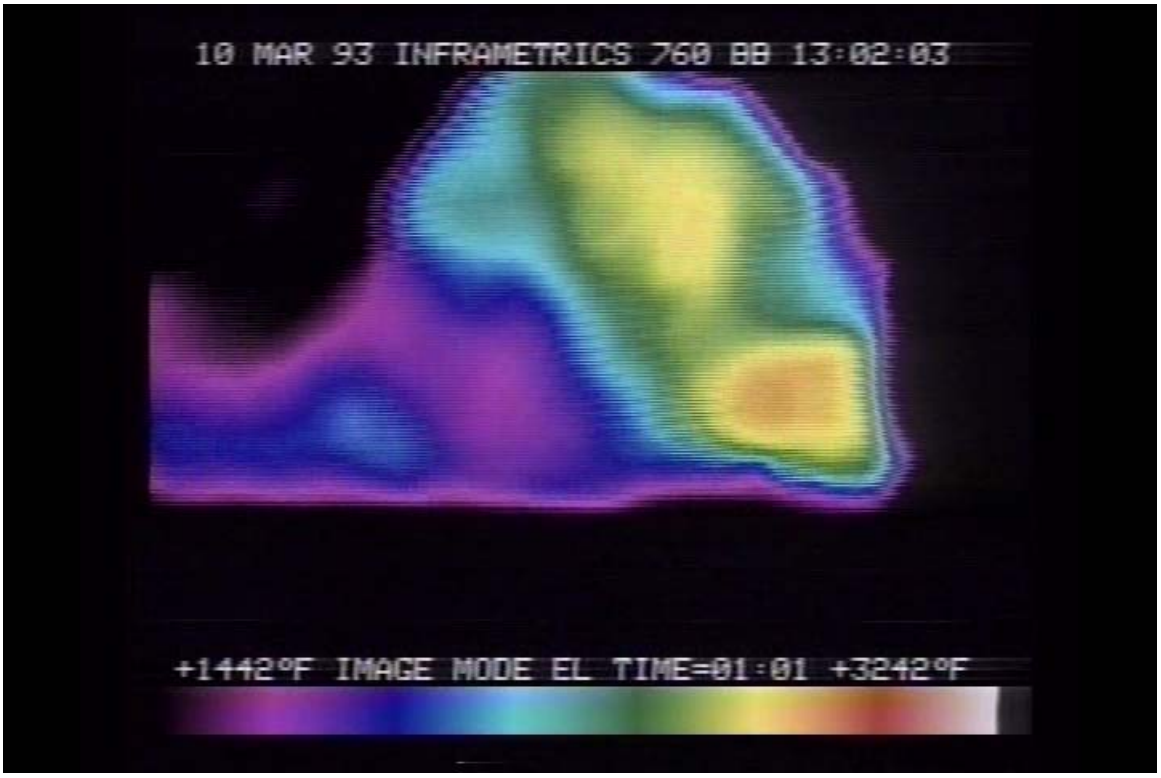

Figure 16. SRB Static test (non-vacuum) - Tail-off progression. Chamber pressures are near ambient atmospheric. No solid particulate emissions are discernable. (Thiokol photo).

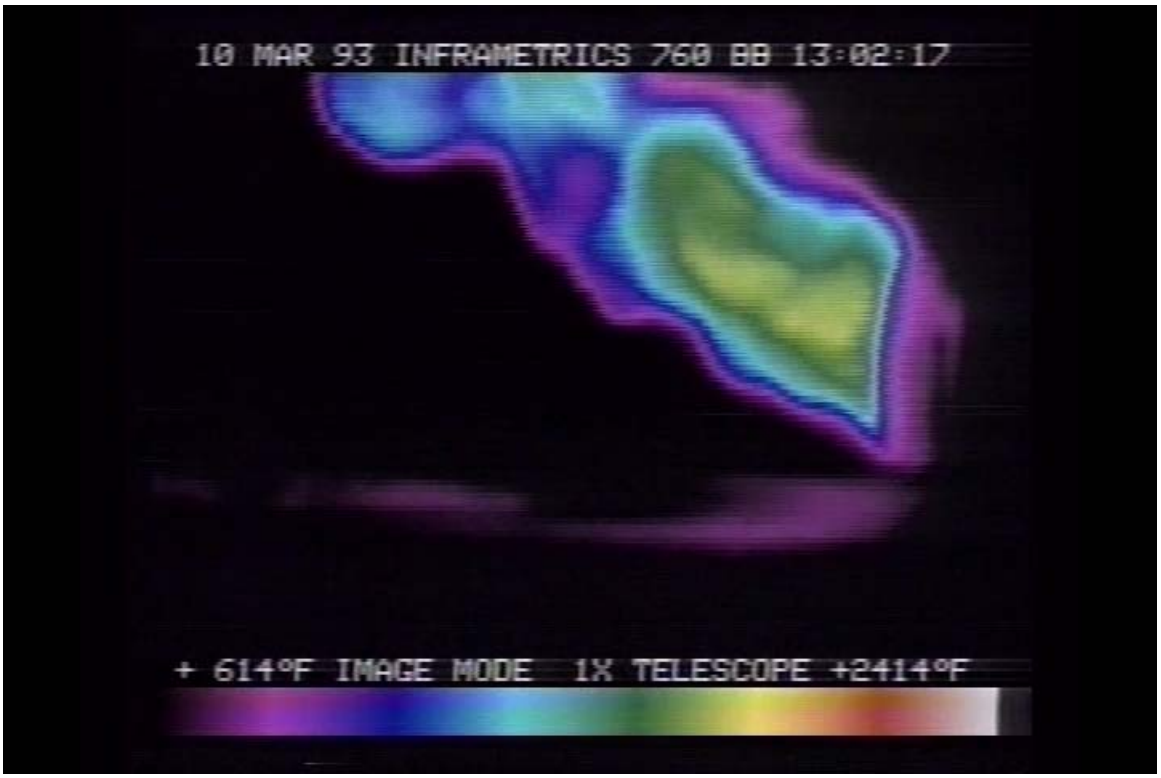

Figure 17. SRB Static test (non-vacuum) – Late Tail-off. Chamber pressures are near ambient atmospheric. No solid particulate emissions are discernable. (Thiokol photo).

B. SRB Data: Shuttle Base Heating –

An early indicator that SRM's exhibited behavior that was not predicted or understood came during the first few Space Shuttle launches. The assessment of Solid Rocket Booster flight performance generated for the Critical Design Review (CDR) predicted that the convective and radiative heat load experienced by the Space Shuttle due to the SRB exhaust plumes would decline steadily throughout the main burn phase and Tail-off and then drop sharply as the boosters separated and terminated. The empirical flight data however revealed unexpected behavior (Greenwood, et al., 1983). As measured for STS-1 through 5, rather than declining steadily, a large radiative heating spike occurred as the SRBs progressed through Tail-off (Figure 18). Specifically, immediately prior to separation, at internal chamber pressures near 69-138 kPa (10-20 psia), radiation from the SRB exhaust plume was twice what was originally predicted as measured at the aft dome of the External Tank (ET) (Figure 19). Similar measurements acquired at the aft skirt of the SRBs also showed the radiative excess (Figure 20).

A convective increase was also measured which was ascribed to diminished exhaust velocity and attendant stagnation. The large radiative component, however, indicated that there was an additional thermal source causing the loading. The probable explanation lies in the ejection of slag particles during the Tail-off phase (Greenwood, et al., 1983). The emissions of tens of kilograms of high temperature (3000 ^{o}K) particulates in the immediate vicinity of the Space Shuttle is at least qualitatively consistent with the observations.

Interestingly, the fifteen second time duration of the radiative excess as measured at the SRB aft skirt (Figure 20) is consistent with the duration of intense Tail-off emissions as observed in both the ground-based optical and in-situ SRB imagery. Numerous glowing particles are seen issuing from the SRBs beginning at the separation event and for tens of seconds afterwards. This imagery will be discussed in detail in the subsequent two sections.

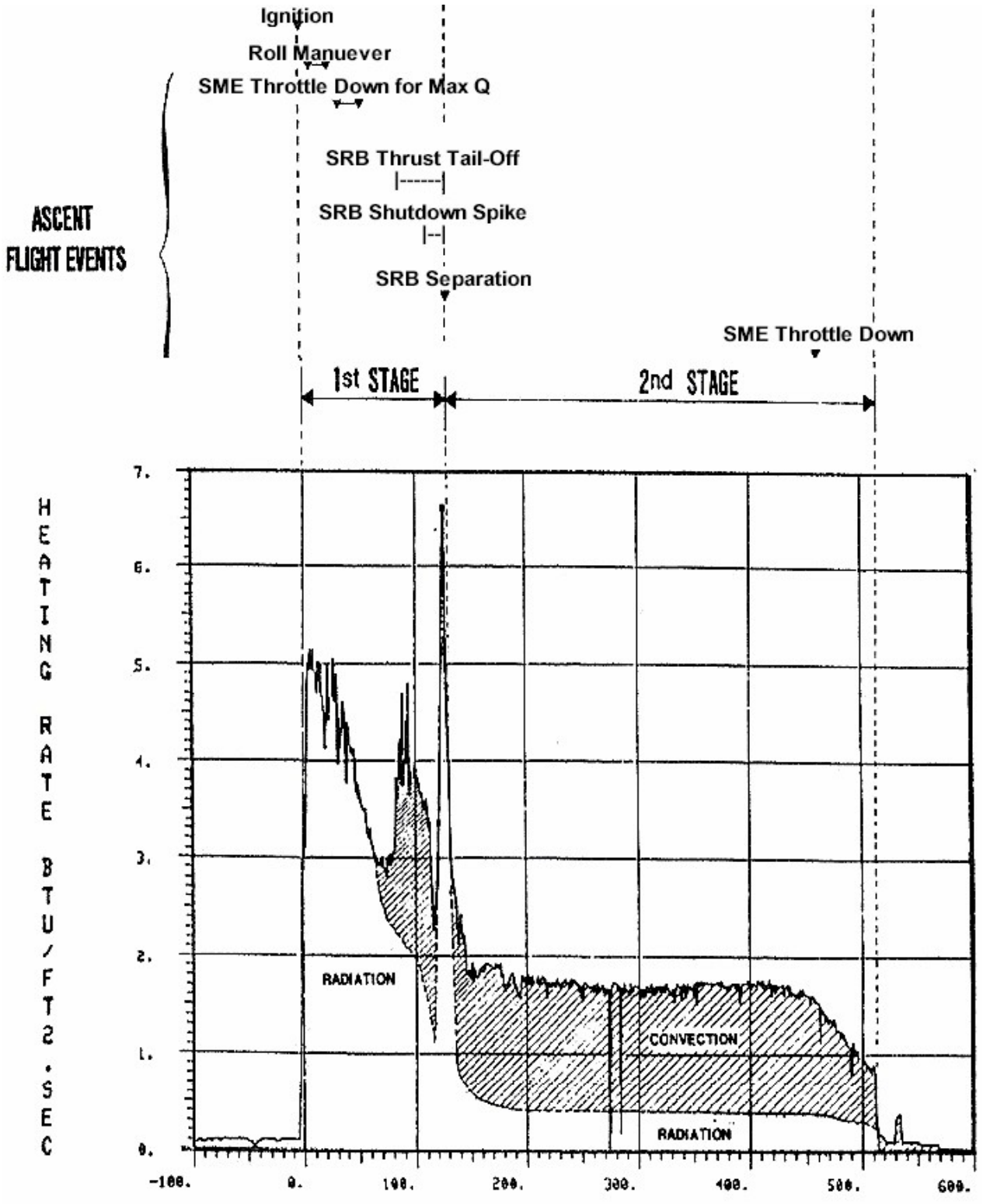

Figure 18. Typical Space Shuttle orbiter heat shield environment during flight. The radiative pulse at Tail-off is clearly evident at approximately 120 seconds into flight. (Greenwood et al., 1983).

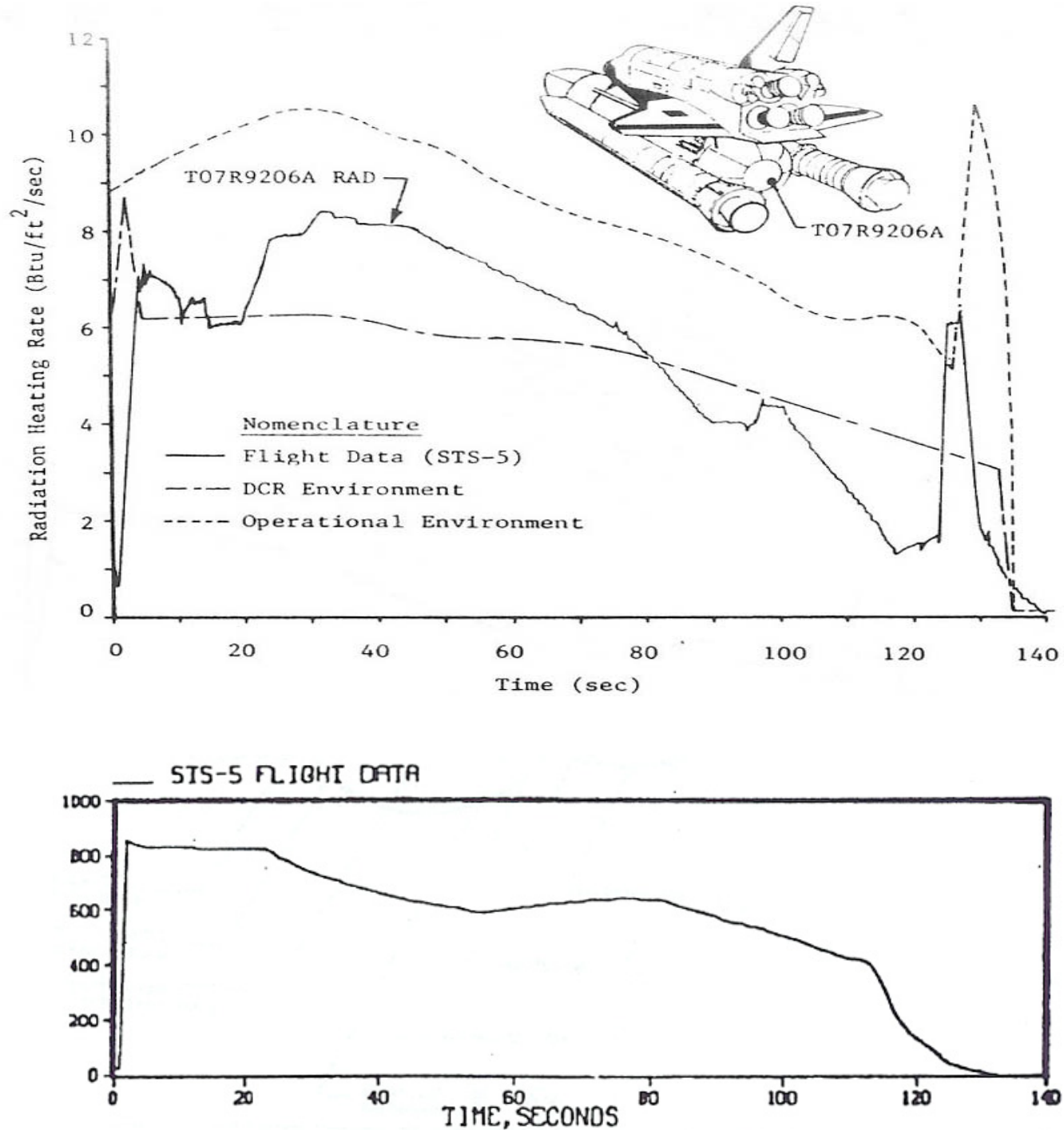

Figure 19. External Tank (ET) radiation base heating and the chamber pressure profile for comparison. The radiation spike occurs during Tail-off at chamber pressures below 344 kPa (50 psia) and extends to vacuum conditions. This behavior is consistent with slag ejection from low pressure boiling as a causative agent.

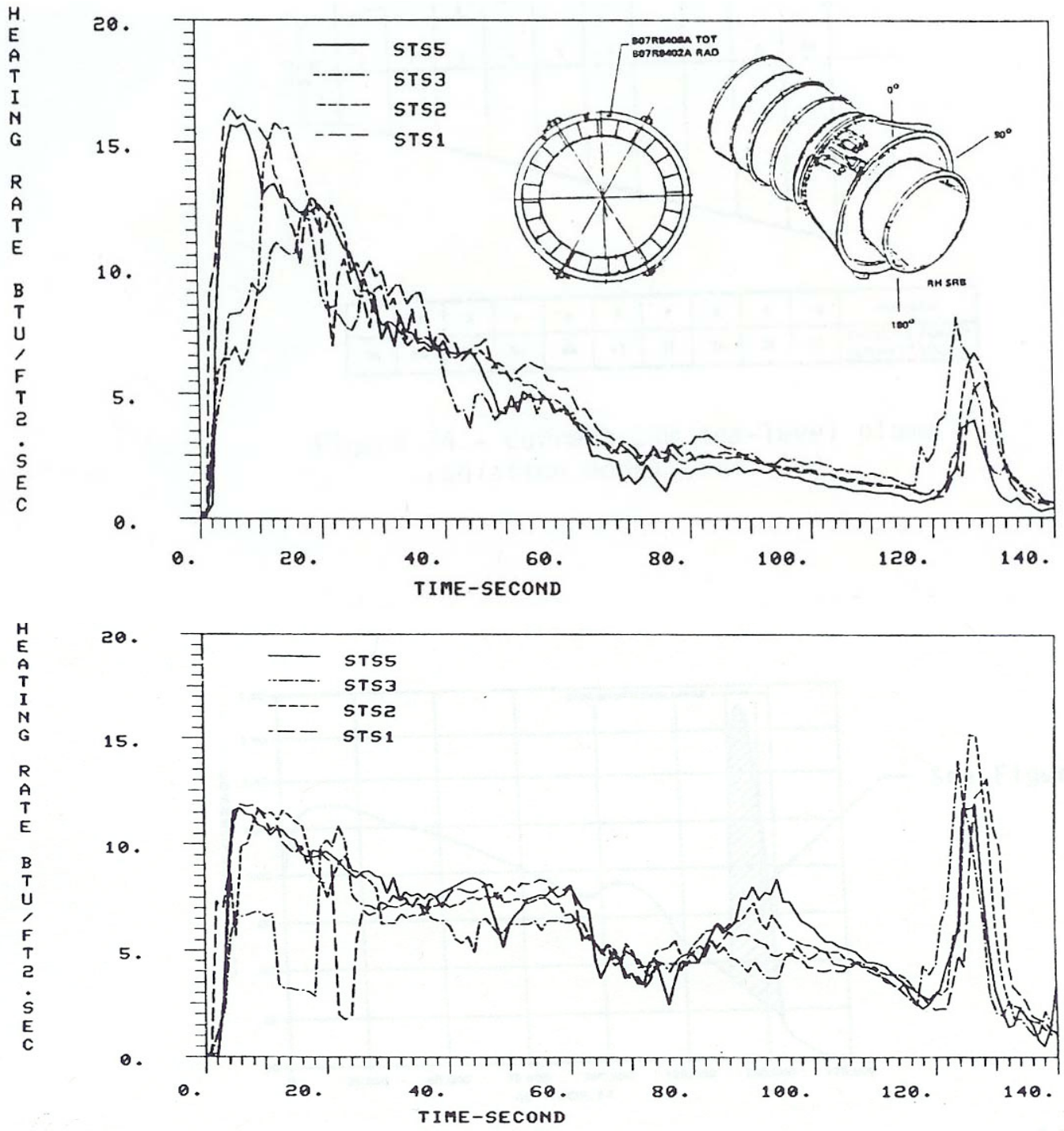

Figure 20. Right SRB Aft Skirt radiation profile. The radiation spike occurs during Tail-off at chamber pressures below 344 kPa (50 psia) and extends to vacuum conditions. Its duration coincides with prodigious solid particulate emissions from SRBs.

C. SRB Data: Ground-Based Imagery -

As discussed above, static ground tests conducted at atmospheric pressure show no significant particulate emissions at Tail-off. This assessment is based upon the presented optical and infrared SRB data provided to NASA, as well as observations reported by Salita (1995) and others. For the vacuum case, data from sub-orbital SRM events has been particularly instructive. In addition to the anecdotal base-heating observations just reported, empirical and extrapolated chamber pressure data coupled with ground-based and in-situ optical observations of SRBs, demonstrate that prodigious Tail-off emissions begin when the chamber pressure drops below approximately 6.9 kPa (1 psia) and continue well into the vacuum state.

Figure 21 shows the chamber pressure (P) for STS-93 (Mark Tobias, PC) with an extrapolation to the SRB post-separation event (ie. <69 kPa (<10 psia)). Although only STS-93 is exhibited, all SRBs have similar time dependent pressure profiles. Figure 22 shows the empirical plus extrapolated pressure profile for the P<241 kPa (<35 psia) regime of interest. Correlating this figure with time-step imagery of SRB ascent, separation (with continued ascent), and eventual descent is particularly instructive for associating Tail-off emission characteristics with SRB chamber pressure. To this end, high resolution ground-based imagery was obtained for a suite of Space Shuttle launches: STS-93, 96, 101, 103, 112, and 113. These missions were chosen because STS-93, 96, 101 and 103 have simultaneous in-situ data available for comparison – enabling a cross-correlation of both near and remote viewing perspectives beginning five to ten seconds after SRB separation. STS-112 and 113 were chosen because of their ease of availability at Johnson Space Center in a low resolution format – which initially prompted this line of investigation.

The ground-based flight imagery shown herein was extracted from original KSC film footage (after Telecine transfer to Digi-Beta tape) acquired with the Playalinda Beach DOAMS Long-Range Tracking telescope (Figure 23). Data was also analyzed from the Cocoa Beach DOAMS tracking telescope, the roof of Vehicle Assembly Builiding (VAB), and several smaller trackers. All data show the same low pressure Tail-off behavior. Playalinda images are shown here due to their exceptional clarity. Figures 24-32 show, in time-pressure sequence, the progression of SRBs through the Tail-off phase. Large particle emissions are absent until chamber pressures are below 6.9 kPa (1 psia) – thus reiterating the tenet that: *significant emissions occur only at Tail-off and only in vacuum conditions.*

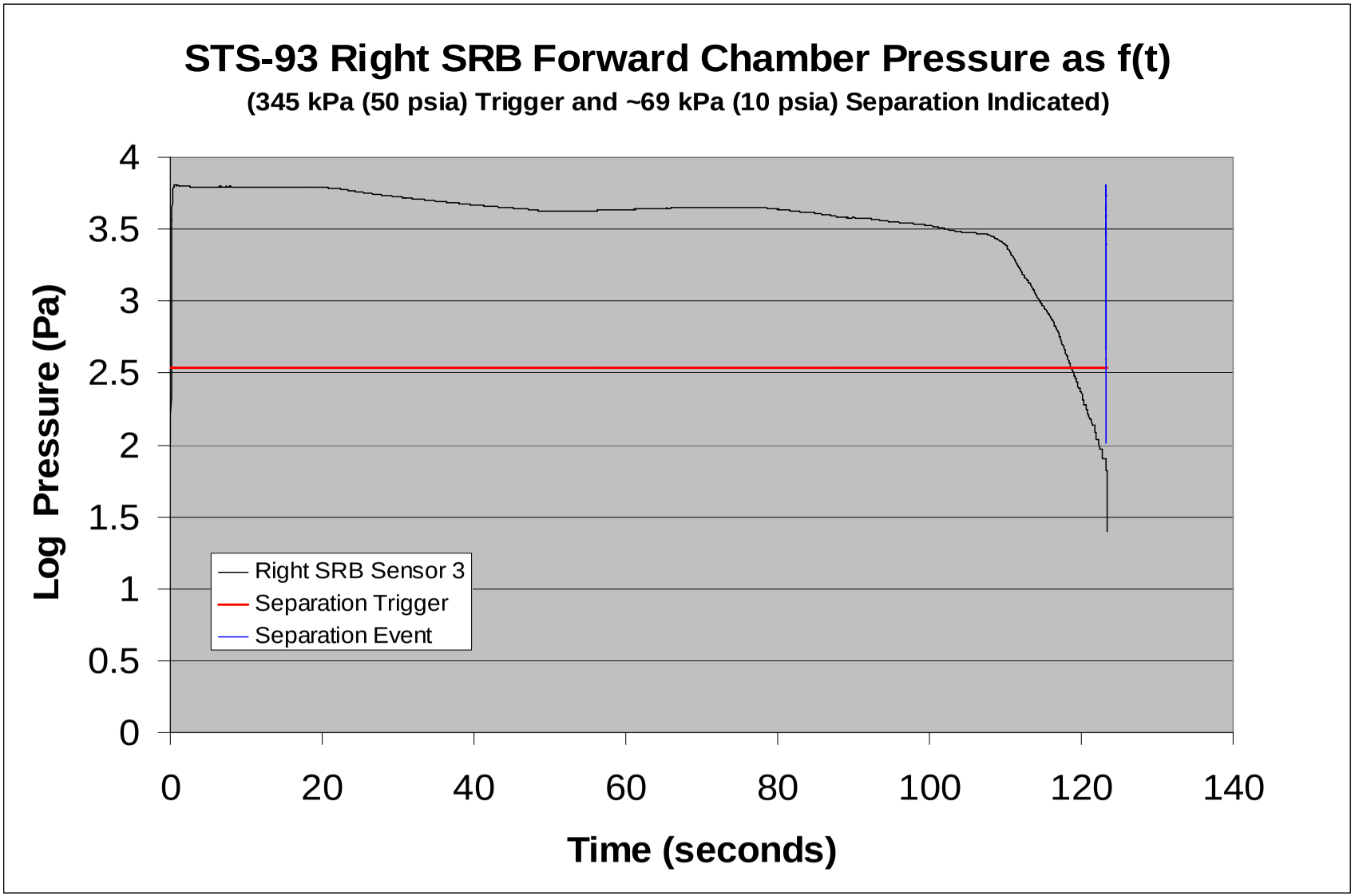

Figure 21. The chamber pressure for STS-93 with an extrapolation to the SRB post-separation event (<69 kPa (<10 psia)). Although STS-93 is exhibited, all SRBs have similar time dependent pressure profiles. Starting at approximately 110 seconds, the pressure drops precipitously through Tail-off - reaching vacuum levels (<< 6.9 kPa (<<1psia)) within 20 seconds. The SRB separation cue is issued at 345kPa (50 psia), actual separation occurs at 6.9 kPa (10 psia), just 4.5 seconds later. (Raw Data supplied by ATK/Thiokol).

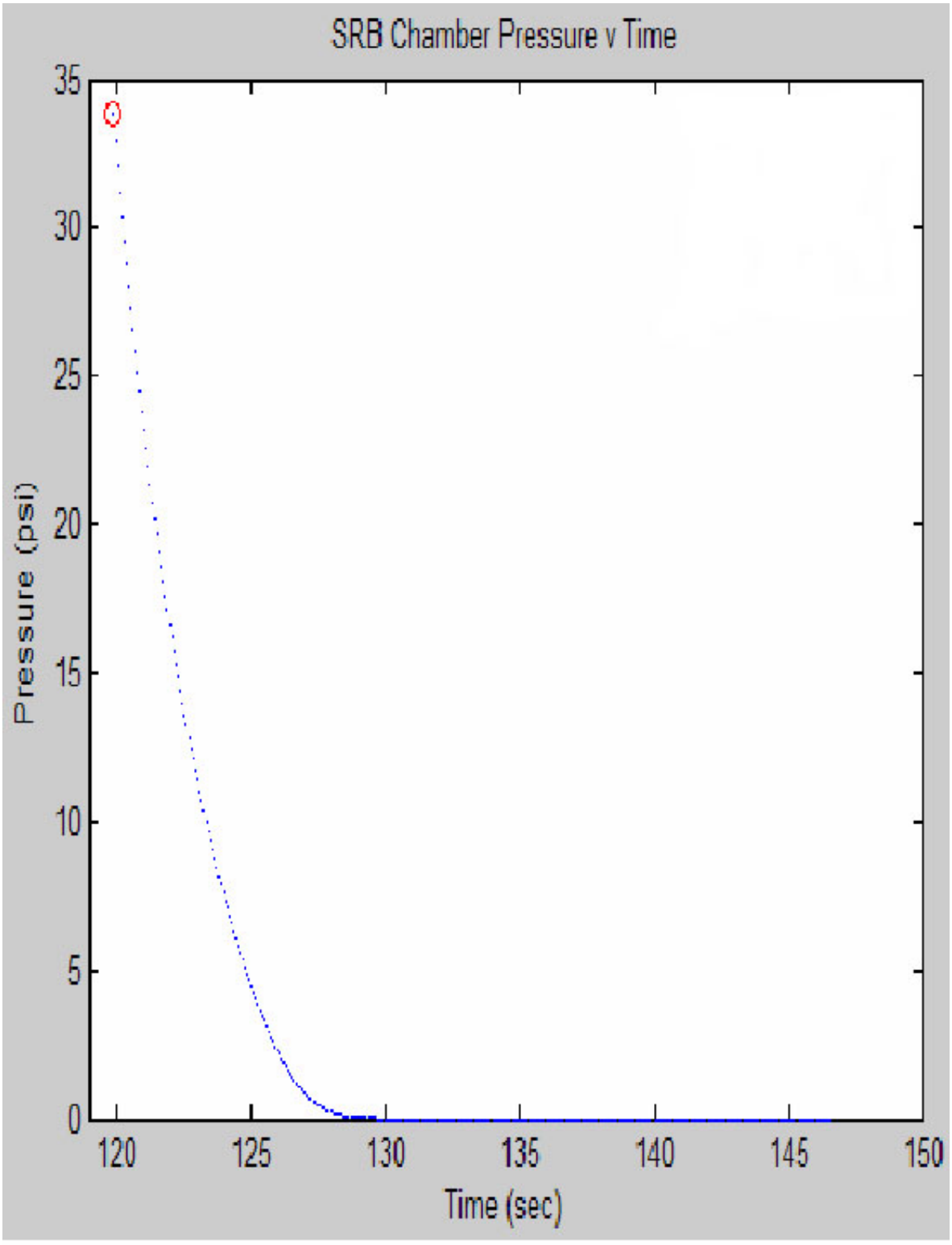

Figure 22. Extrapolated pressure profile for the P<241 kPa (<35 psia) regime. Correlating this figure with time-step imagery of SRB flight reveals that the mass of Tail-off ejection occurs at chamber pressures below 6.9 kPa (1 psia) – consistent with low-pressure boil-over.

Figure 23. Playalinda Beach DOAMS Long Range Tracker [40 cm Aperture Catadioptric; 400” Focal Length (Film)] (NASA)

Figure 24. STS-101 Time Sequence. Separation -4.0 seconds; Chamber pressure ~275 kPa (~40 psia). No Tail-off ejecta present.

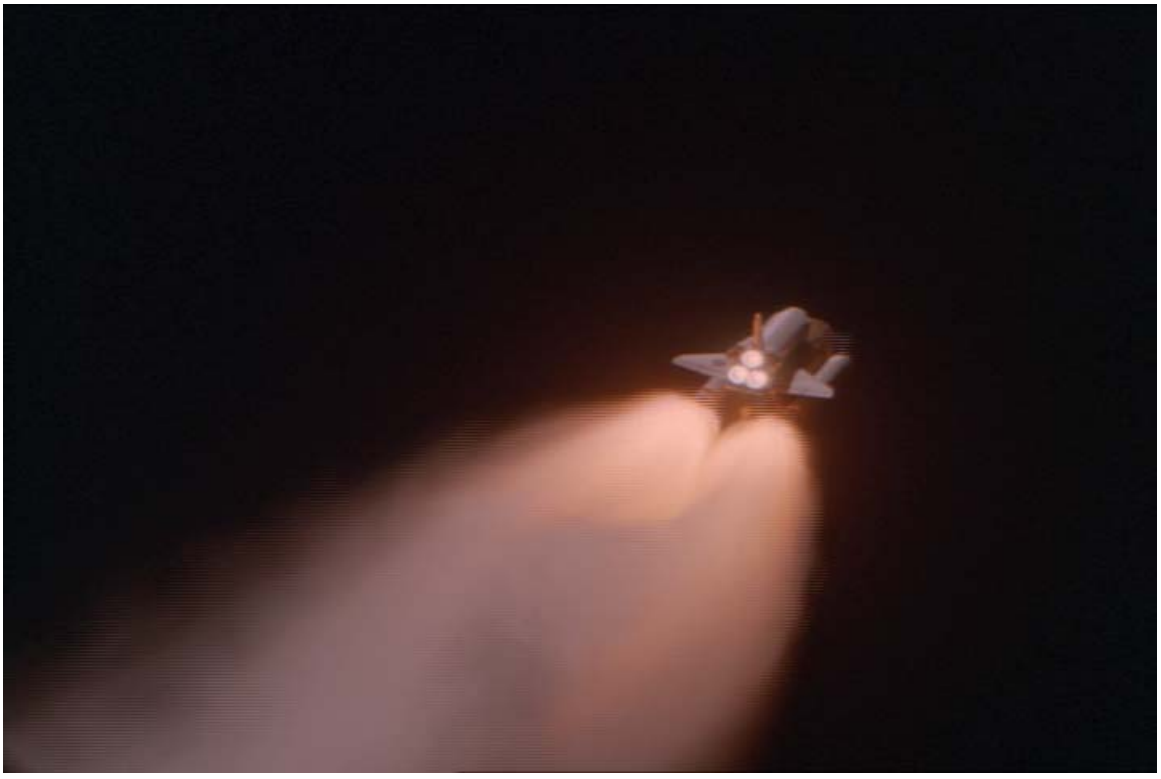

Figure 25. Separation Cue -0.0 second; Chamber pressure 6.9 kPa (10 psia). No Tail-off ejecta present, but shuttle base heating indicates some particulates are present in the plume.

Figure 26. Separation + 1 second; Chamber pressure ~3.4 kPa (~5 psia). Tail-off ejecta are probably present but obscured by the Booster Separation Motor (BSM) plume.

Figure 27. Separation +5 seconds; Chamber pressure < 6.9 kPa (< 1 psia). Tail-off ejecta are present but not yet resolved in the ground-based imagery due to limited dynamic range (blooming) in the image.

Figure 28. Separation +12 seconds; Chamber pressure < 6.9 kPa (< 1 psia). Tail-off larger ejecta are clearly visible, smaller objects are becoming visible at the plume perimeter.

Figure 29. Separation +16.5 seconds; Chamber pressure < 6.9 kPa (< 1 psia). Smaller Tail-off ejecta visible as a mist that is on the cusp spatial resolvability.

Figure 30. Separation +20.5 seconds; Chamber pressure < 6.9 kPa (< 1 psia). Smaller Tail-off ejecta are becoming more clearly differentiated and spatially resolved.

Figure 31. Separation +22.5 seconds. Chamber pressure < 6.9 kPA (< 1 psia). Numerous Tail-off ejecta are clearly resolved as the plume brightness fades.

Figure 32. Separation +24.5 seconds. Chamber pressure < 6.9 kPa (< 1 psia). Numerous Tail-off ejecta are clearly resolved as the plume brightness continues to fade.

Figure 33. Separation +30.5 seconds. Chamber pressure < 6.9 kPa (< 1 psia). Numerous Tail-off ejecta are clearly resolved as the plume brightness fades. Ejecta continue to stream from the SRB, although at a reduced rate, for several minutes.

D. SRB Data: In-Situ Imagery –

In addition to the physical arguments elucidated in Section III, the static SRB tests, the Space Shuttle base heating measurements, and the ground-based optical telescopic imagery have each been consistent with the bulk Tail-off vacuum particulate emission scenario. The available in-situ data is similarly consistent but lends an additional clarity due to the close proximity view it provides of SRM emissions. This in-situ data consists of imagery obtained from small cameras mounted in the forward skirt (just aft of the frustrum) of the Space Shuttle SRBs. These cameras were oriented orthogonal to the SRB axis and pointed at the External Tank (ET) during flight. Upon SRB separation each camera passively followed its opposing SRB fairly consistently until the onset of significant tumbling. These cameras were flown on STS-93, 96, 101, and 103. Data from all four missions were analyzed and, except for variations in ambient lighting and the presence (or lack) of calibration sources, were found to be essentially identical in terms of the SRB behavior they recorded. Data from STS-101 is presented here because it coincides with the exceptional STS-101 ground-based imagery acquired via the Playalinda tracking camera (Section III.C.). It is instructive to compare frames acquired from the ground with those obtained at the same moment in-situ. Such comparison readily reveals the limitations of remote sensing (even with high quality optics and under photometric conditions) relative to the advantages of close proximity in-situ data collection (even with relatively unsophisticated instrumentation of only modest optical quality).

Figures 33-39 show the progression of Tail-off emissions for the Shuttle's STS-101 Right SRB as viewed from the camera mounted on the Left SRB. The SRB nozzle first comes into view nine seconds after separation (Figure 33) at which point chamber pressure is near a vacuum state (< 6.9 kPa (< 1psia)) and Tail-off emission of slag is fully underway. Although the image is saturated, two distinct plumes are visible: one composed of pyrolysis gases and dust-like Al_2O_3 combustion products of high area-to-mass ratio (A/M) and the other composed of primarily solid or rapidly solidifying Al_2O_3 particles. As the image sequence progresses in time, the two plumes diminish in brightness and the latter becomes resolvable into thousands of slag particles. These particles issue from the SRBs at a decreasing rate, until, after approximately 30 seconds post-separation, the rate has dropped from several thousand per second to a few dozen. This entire sequence of behavior is materially different than that observed in static testing particle of SRBs (Section IV.A.). Emissions of this kind are not seen at atmospheric pressure - once again strongly

corroborating the idea that slag is only ejected in significant quantity at Tail-off and only under vacuum conditions.

Because this Tail-off emission behavior is not exhibited in static tests conducted at atmospheric pressure, the large particle distribution function (in terms of size and mass) from those tests is not representative of that obtained under vacuum conditions and thus does not represent a fiduciary reference for accurate orbital debris assessments. To rectify this, Section V describes a method developed to ascertain the size distribution from the in-situ data. The limited but interesting results indicate all detectable particles are within a 2-5cm diameter size range.

It is important to note that in-situ Shuttle SRB audio data indicates that some of the emitted particles either exit the SRBs in a solid state or rapidly solidify (a sharp metallic ping is heard when particles strike the SRB casing – whereas molten particles might be expected to yield a muffled sound). Coupling this observation with the approximately 3500 ^{o}K chamber temperature and Blackbody-based luminosity and cooling rate predictions indicates that theses solid particles probably consist of Al_2O_3 (Melting Point (M.P.) 2072 ^{o}C) rather than pure Aluminum (M.P. 660 ^{o}C). Pure Al ejecta would have insufficient time to solidify before impact, whereas Al_2O_3 solidifies within a few seconds.

Figure 33. STS-101 Right SRB (as viewed from the Left SRB). Separation +9 seconds. (Chamber Pressure < 6.9 kPa (< 1 psia) for this and all subsequent images). Although the image is saturated (due to limited dynamic range and intense emissions), the two gaseous/dust and solid particulate plumes are distinctly visible.

Figure 34. Separation +10 seconds. Solid particulates are visible in the solid particulate plume.

Figure 35. Separation +12 seconds. Dual plumes are well differentiated. Profuse Tail-off emissions are evident (> 1000 particles per second). Compare this with the Figure 28 ground-based view acquired at almost the same instant.

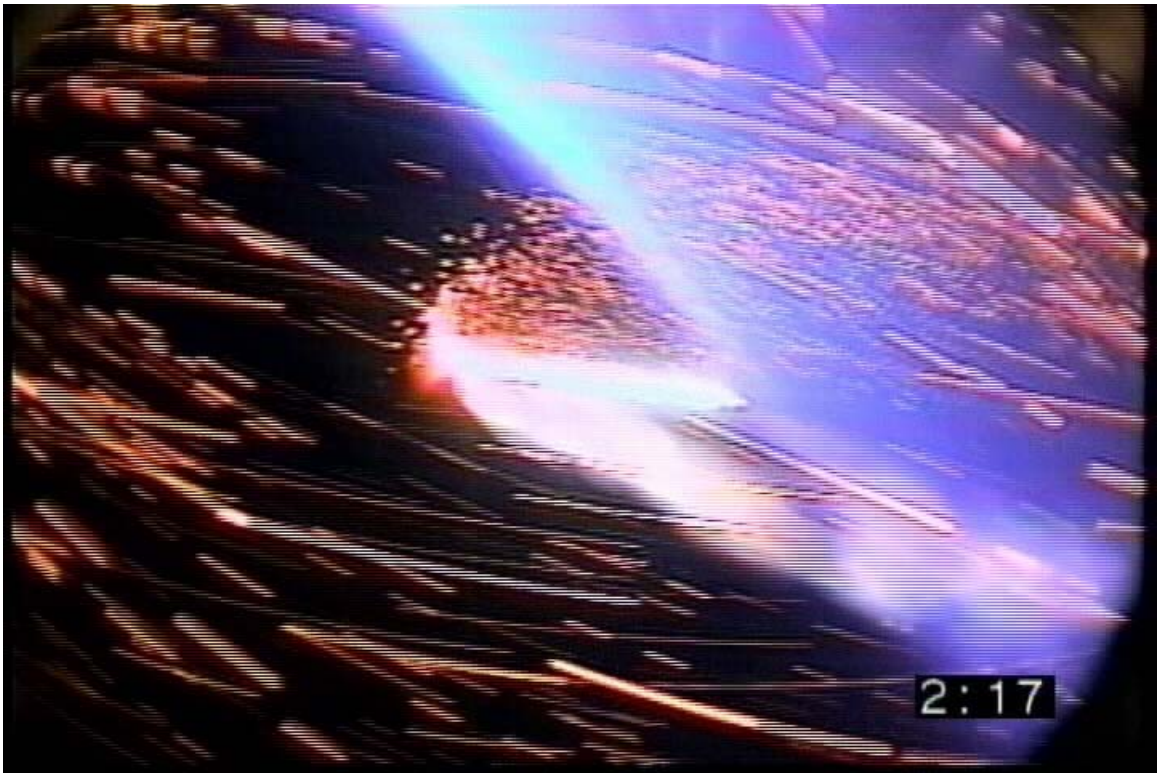

Figure 36. Separation +12.5 seconds. Self-emissions from the Left SRB occupy the foreground. In audio data, a solid metallic ‘ping’ is heard when these particles strike the SRB exterior – indicating the objects solidify quickly and thus have a high melting point (ie. Al_2O_3).

Figure 37. Separation +14 seconds. Emissions continue at a high rate.

Figure 38. Separation +30.8 seconds. Emissions have slowed to a few dozen particles per second.

Figure 39. Separation +40.5 seconds. Emissions are ebbing but continue. These streaks are self-emissions from the descending Left SRB.

E. SRB Data: Post-recovery measurements:

A key test of the vacuum slag loss scenario is the post Tail-off measurement of residual chamber slag for an SRM fired under vacuum conditions. While vacuum static test sources are currently being investigated (Section IV.H.), measurements like these were conducted for the sub-orbitally ejected left SRB on STS-5 after its post-Atlantic recovery (Figure 40). In that instance, no aluminum oxide remained in the chamber – a result indicative of a physical process, such as boil-over, leading to the complete expulsion of residual slag. This is contrasted strongly with the typical (non-vacuum) static ground test result where residual SRB chamber slag masses of hundreds or thousands of kilograms are normally encountered. Table I shows the results of chamber measurements for the STS-1 through 5 SRBs. The weights include liner material in all cases except for STS-5 B (Left SRB) – which measured only slag.

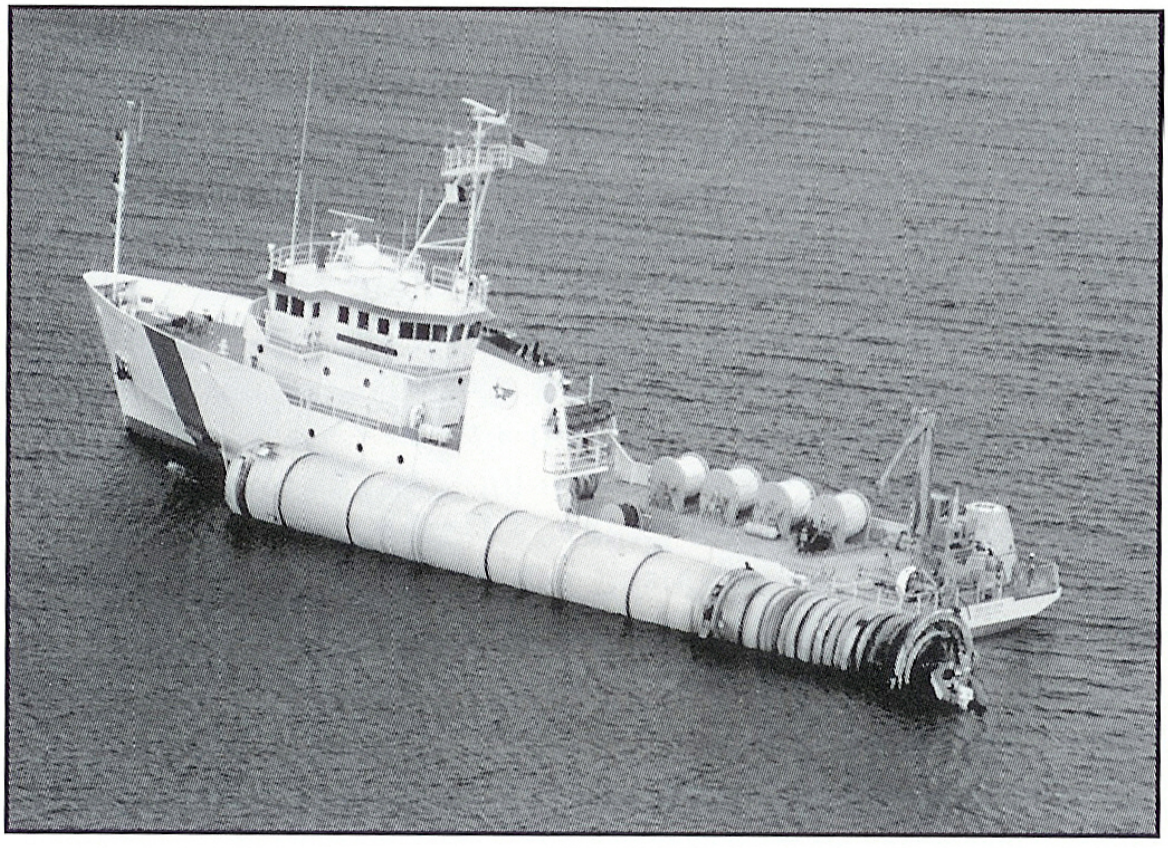

Figure 40. Atlantic recovery of an expended SRB. (NASA Photo).

Table I. Residual SRB Chamber Debris was collected and measured for Post-Atlantic Recovered Right (R) and Left (L) SRBs for STS-1,2,3, and 5. For STS-5(L) only the residual slag was measured – the 0.04 kg value indicates complete expulsion.

Mission	SRB	Mass (kg)	Material Description
STS-1	R	200.5	Aluminum Oxide Slag plus Liner and Nozzle (phenolic)
	L	119.1	"
STS-2	R	185.9	"
	L	126.8	"
STS-3	R	52.7	"
	L	57.3	"
STS-5	R	252.3	"
	L	0.04	Aluminum Oxide (Al_2O_3) Slag Only

F. Pegasus Launch Vehicle –

In-situ observations of Pegasus 1st and 2nd stages, also show profuse large particle emissions commencing during Tail-off. Despite a two order-of-magnitude range for the initial propellant mass between the SRBs and Pegasus, the same phenomenon is observed – slag accumulated during the main burn phase is liberated at Tail-off if vacuum conditions are present. Figures 41-47 show a sequential series of still frames extracted from a video stream acquired by an in-situ camera (Rocket Cam) mounted near the vehicle fairing and facing aft. This 1st stage sequence, selected for its exceptional clarity, is from the 1993 Alexis launch. Several other Pegasus launches sequences have been obtained and all show identical behavior for both 1st and 2nd stages. Third stage data, which is expected to show similar behavior, has not yet been acquired. A photometric size determination (like that performed in Section V for the in-situ SRB data) was not attempted due to the lack of a suitable calibration reference.

Figure 41. Tail-off –1.5 seconds. Pegaus 1st Stage SRM showing main burn phase exhaust plume devoid of any particulates of sufficient size to be individually visible. The plume consists primarily of 5-10 μm diameter Al_2O_3 dust.

Figure 42. Tail-off -0 sec. Approximately 1.5 seconds after the previous photo, the Tail-off phase is underway. The plume is visibly smaller as the propellant is nearing exhaustion. The first large particle emission has begun (short streaks at right and left edges of plume).

Figure 43. Tail-off +1.5 sec. The dust plume has almost disappeared and a few faint sporadic large particles are visible.

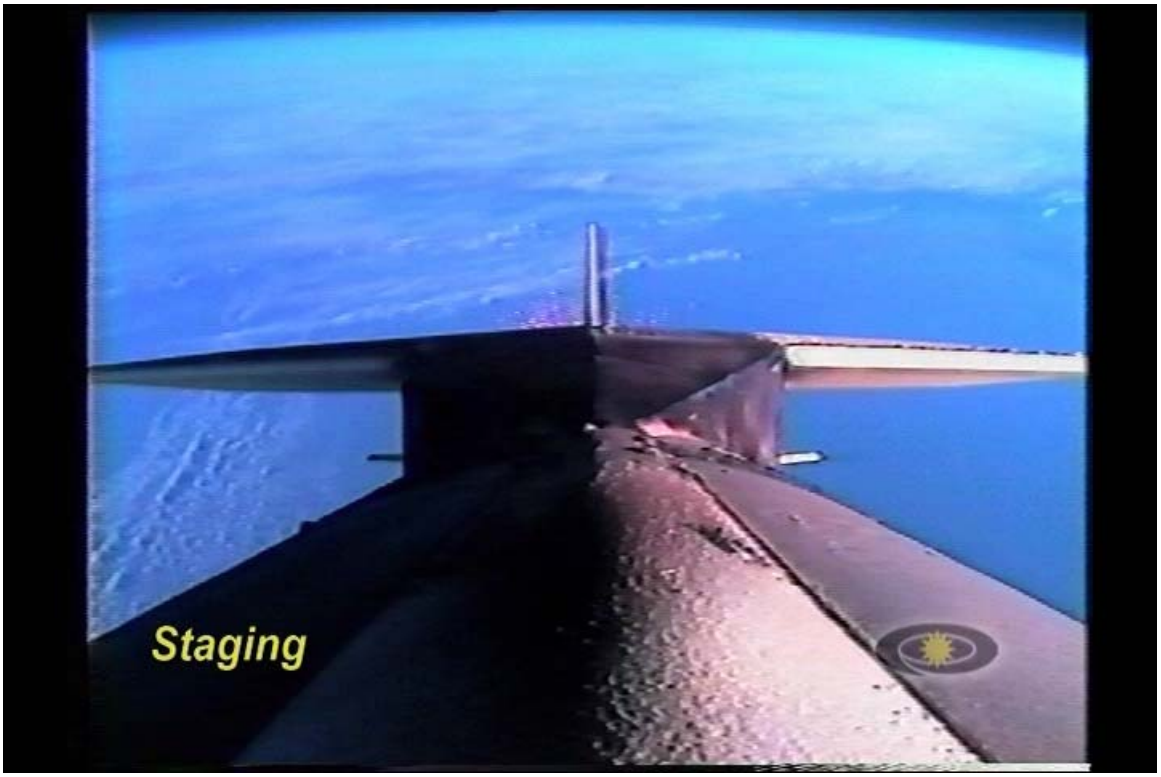

Figure 44. Tail-off +9.5 sec. The first bulk particle emission is visible. Several dozen embers are seen issuing from the 1st stage.

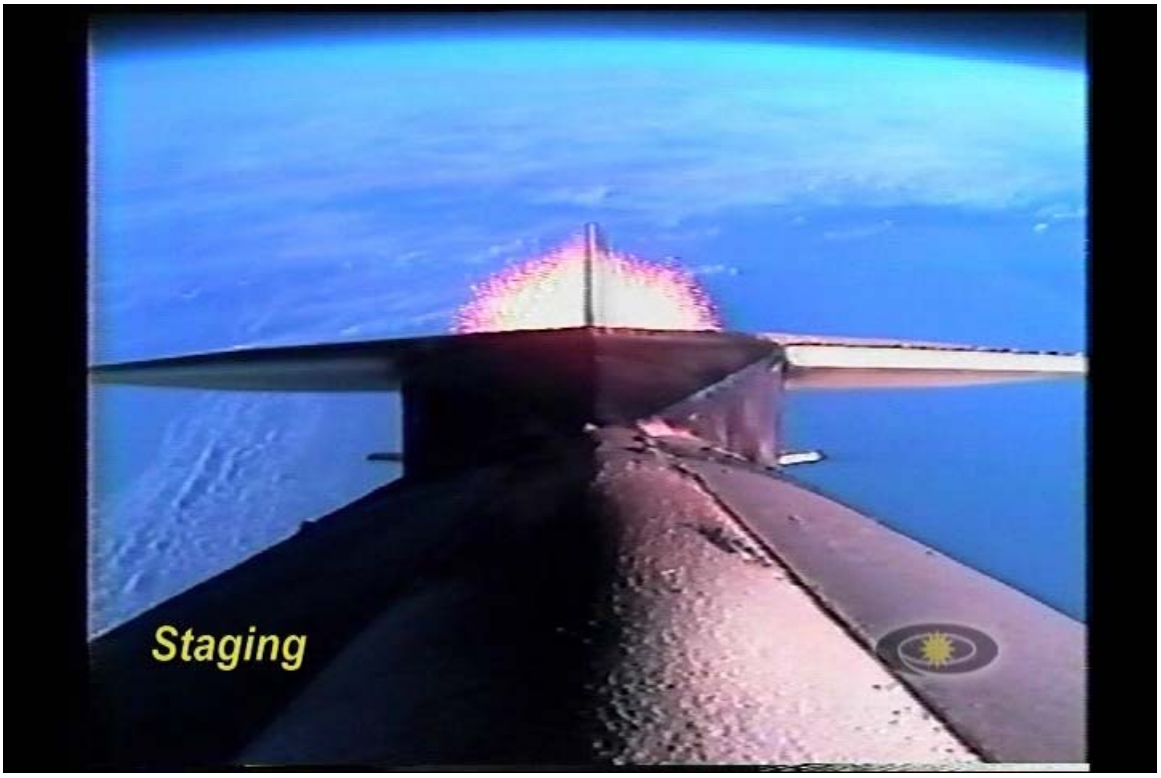

Figure 45. Tail-off +11.5 sec. A burst of several thousand large particles is emitted. Sizes are estimated to be of order 1 cm diameter.

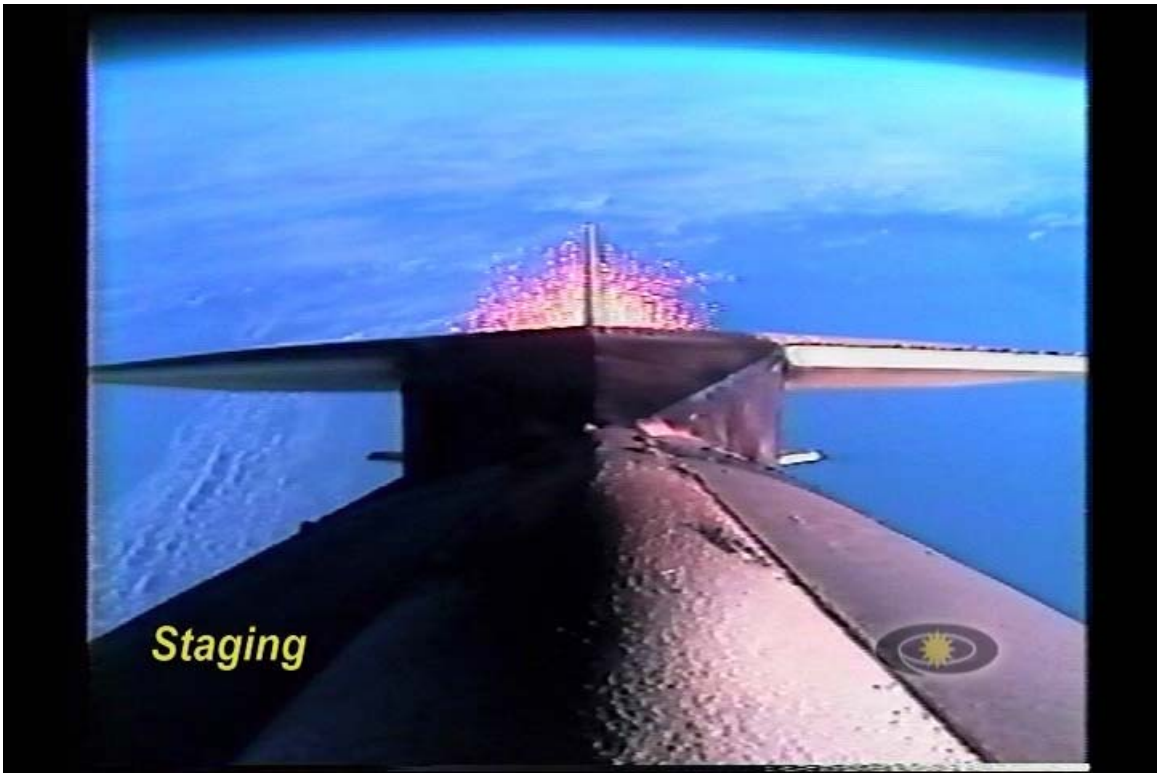

Figure 46. Tail-off +15.5 sec. Bulk large particle emission continues for approximately four seconds before diminishing to a sporadic rate.

Figure 47. Tail-off +20 sec. Sporadic large particle emissions - which may continue for several hundred seconds.

G. Delta II GEM Boosters -

In-situ observations of Delta II GEM burns, obtained with aft facing Rocket Cam's mounted on the Delta II rocket body, also show particle emissions commencing during Tail-off. The behavior with these motors is less consistent and sometimes more difficult to discern however than that of the SRBs or Pegasus vehicles. The motors are smaller and therefore eject much less slag and for much shorter duration. Also, during some flights there are occasional sporadic flashes during primary booster burn phase, but these flashes might result from debris dislodged from the vehicle's ascent. The flashes may also represent slag ejected via the instabilities postulated in Section III.B. Ejection during the main burn phase is not precluded, but the particle diameter is necessarily limited (D< 500 μm) due to shearing forces.

Figure 58-71 represent a suite of images from different launches, day and night, which show Tail-off particulate ejection for both ground-lit (separation altitude ~21.7km; 4.190 kPa (0.6 psia)) and air-lit SRMs. This illustrates that: *as long as near vacuum conditions prevail at Tail-off, large particulate slag ejection occurs - irrespective of the motor's initial ignition altitude or flight environment.*

Figure 58. During the main phase of the booster burn, the plume is devoid of significant large particle content. Sporadic flashes are seen but these may be debris dislodged from the exterior surface. Figs. 58-61: April 7, 2001 Delta II Odyssey.

Figure 59. During the Tail-off phase large particles are clearly evident emanating from the SRM booster.

Figure 60. Tail-off emissions are seen to persist for approximately 1 second before booster separation.

Figure 61. At booster separation, it is difficult to ascertain whether Tail-off emissions continue.

Figure 62. Air-lit SRM boosters exhibit comparable behavior to ground-lit motors. During the main burn phase (shown here), no large particulates are evident. Figs. 62-65: April 7, 2001 Delta II Odyssey air-lit SRM booster on 1st stage.

Figure 63. Tail-off phase of an air-lit Delta II booster. Large particulates are seen issuing from the SRM. Note the bright plume has contracted and darkened significantly relative to the previous frame – indicating that chamber pressures have declined into Tail-off.

Figure 64. Tail-off phase continues for an air-lit Delta II booster. Large particulates issue from the SRM for several seconds prior to separation.

Figure 65. Delta II air-lit booster separation. Large particulate emissions are no longer discernable.

Figure 66. While the viewing angle and resolution are poor, there are brief large particulate emissions less than 1 second prior to booster separation in this June 6, 2003 Delta II Spirit launch (Figs 66-67). Note faint embers between two boosters at left center of photo.

Figure 67. These Delta II booster are essentially completely depleted prior to separation. This may be why Tail-off emissions are sometimes more difficult to discern – the emissions are obscured by the main engine and the air-lit booster plumes.

Figure 68. Night launch of a Delta II (July 16, 2000 GPS IIR-5). This image was acquired during Ground-lit SRM Tail-off at 7 seconds prior to separation. Particle emissions are readily evident.

Figure 69. Night launch of a Delta II (July 16, 2000 GPS IIR-5). This image was acquired during Ground-lit SRM Tail-off at 5.5 seconds prior to separation. Particle emissions are readily evident and persist until separation.

Figure 70. Night launch of a Delta II (July 16, 2000 GPS IIR-5). This image was acquired during Air-lit SRM Tail-off at 5.5 seconds prior to separation. Particle emissions are readily evident and persist until separation. Note the expanded plume under high vacuum.

Figure 71. Night launch of a Delta II (July 16, 2000 GPS IIR-5). This image was acquired during Air-lit SRM Tail-off at 4.5 seconds prior to separation. Particle emissions are readily evident and persist until separation.

H. Star-37: Vacuum Static Test

Static ground tests, when conducted in vacuum, show behavior qualitatively similar to that observed in space events. In particular, prodigious Tail-off slag emissions which are not seen in static ground tests conducted at atmospheric pressure are seen in the same tests conducted in a vacuum. As has been reiterated many times, the reason is clear – the normally accumulated Al_2O_3 slag cannot boil-over if the ambient pressure exceeds approximately 69 kPa (10 psia). Furthermore, due to depletion of the heat reservoir via evaporative losses and the consequent steady decline of the slag vapor pressure, the length of time over which boiling continues is related to the pressure decline within the chamber. Since boiling ceases when the slag cools to the point that its vapor pressure is below ambient, if the chamber pressure decline is truncated, then the boiling period will be curtailed. Only under vacuum conditions is the boiling period maximized and therefore the maximum amount of slag converted to particulate ejecta.

In order to obtain a particle size distribution function that is representative of a space event, and therefore valid as an input for orbital evolution models, test conditions must facilitate the slag ejection comparable to what might be realistically encountered in space. Since evidence indicates that essentially all SRM slag is ejected (e.g. STS-5 SRB) in space events, the test environment needs to be conducive to this. A test cell operated under vacuum conditions is required and the J-6 Altitude Simulation Cell at the USAF Arnold Engineering and Development Center, TN (Figure 72) meets this criteria (Brandon, et al., 2004).

Figure 73 shows the test set-up for a Star-37 SRM with a propellant mass of 1045 kg. The SRM was spun at 60 rpm and fired while near vacuum (< 0.9 kPa (< 0.13 psia)) conditions were continuously maintained for the 66 second test duration. Figures 74-78 show various optical images of the test as viewed from above the horizontally oriented SRM. The images include the main burn (Figure 74) with its laminar plume, the beginning of Tail-off with its attendant turbulence (Figure 75), and various Tail-off slag ejection events (Figure 76-78). These events are assembled in a frame by frame mosaic extracted from the 45 frame-per-second test imagery.

Figure 79 shows a solidified slag particulate collected from the floor of the test chamber. SEM microscopy (Bernhard 2004) shows that it is composed of Al_2O_3. As will be discussed in Section VI, particle collection from multiple vacuum tests of various SRMs should be conducted in a systematic manner in order to assess the percentage of initial propellant mass that is converted to ejecta and to generate a particle size distribution function for SRM ejecta. Space-based in-situ measurements have exceedingly limited efficacy and accuracy by comparison.

Figure 72. The J-6 Altitude Simulation Cell at AEDC is routinely used to test SRMs in a low pressure environment (1.38 kPa (<0.2 psia)) – effectively duplicating space vacuum conditions.

Figure 73. Star-37 SRM with 1045 kg of propellant shown loaded into the J-6 test cell. Various sensors (eg. optical and IR imagers, pressure sensors (cell and chamber)) surround the motor.

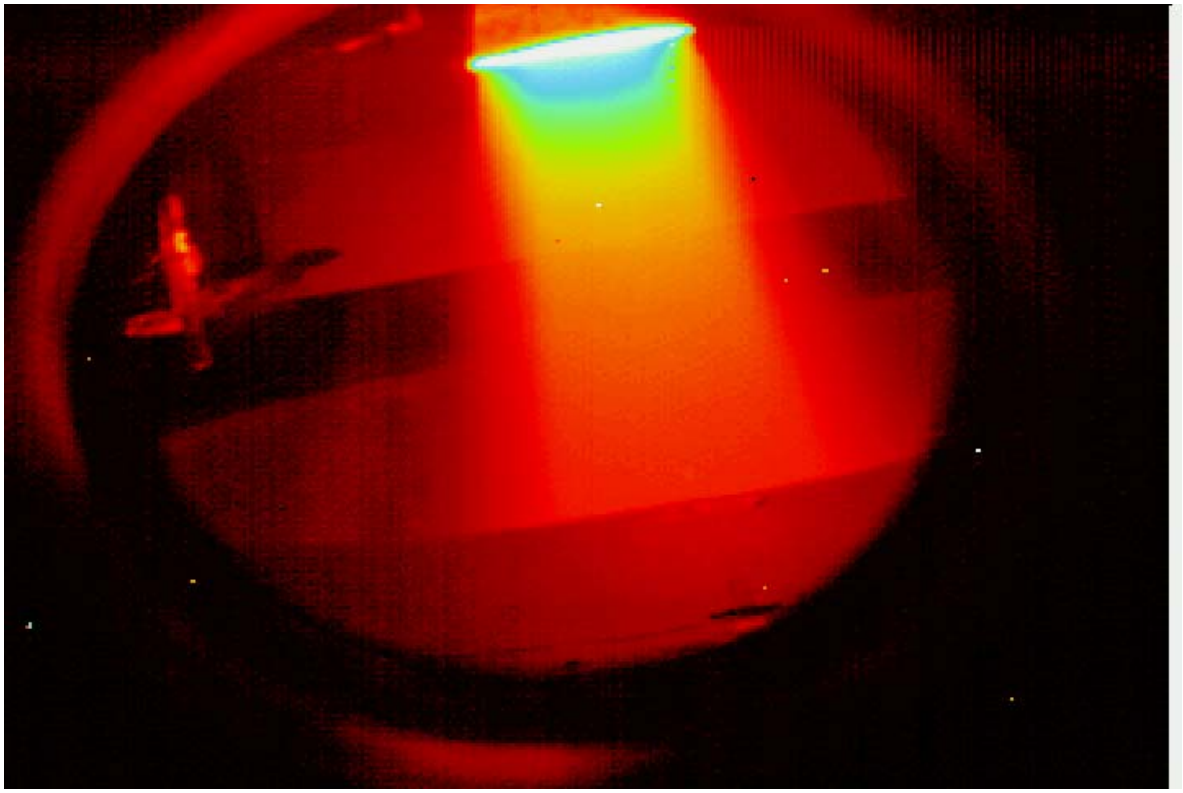

Figure 74. Main burn phase of spinning (60rpm) Star-37 SRM showing laminar plume. (Chamber pressure > 3.1 MPa (> 450 psia)).

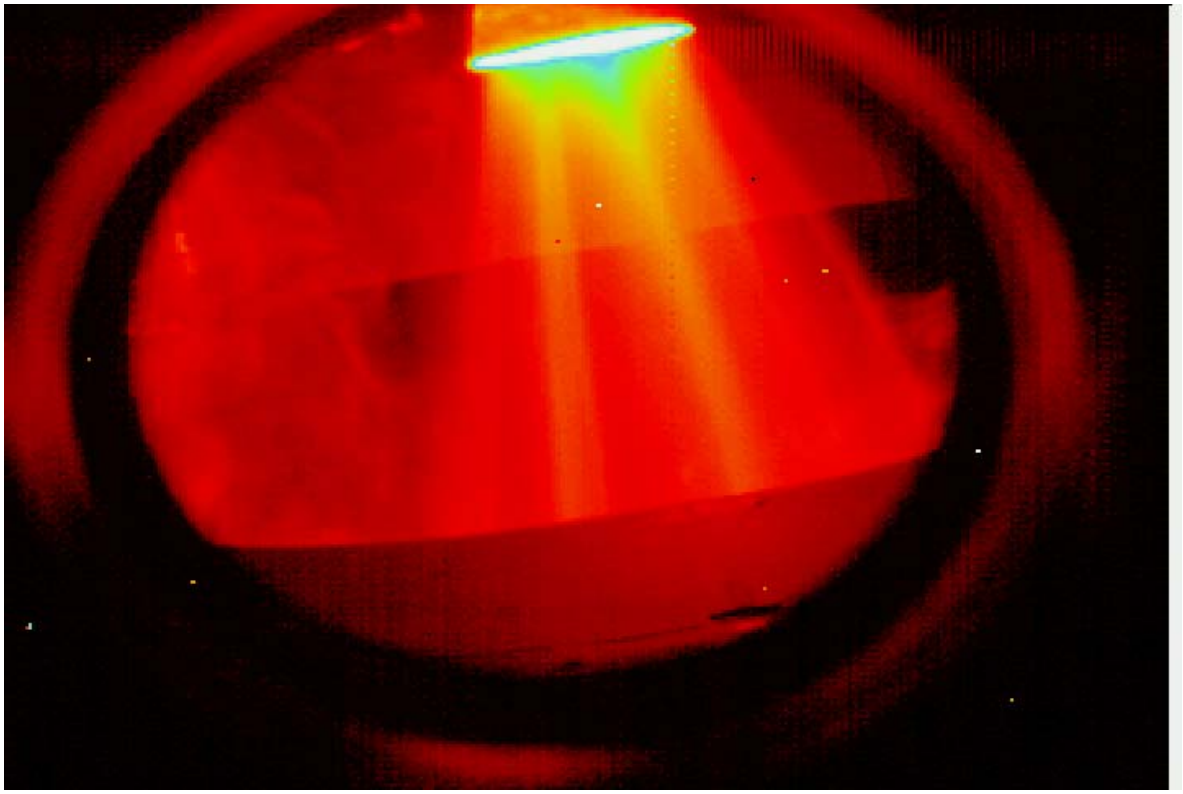

Figure 75. Onset of Tail-off in Star-37 static vacuum test. (Chamber pressure < 344 kPa (< 50 psia)).

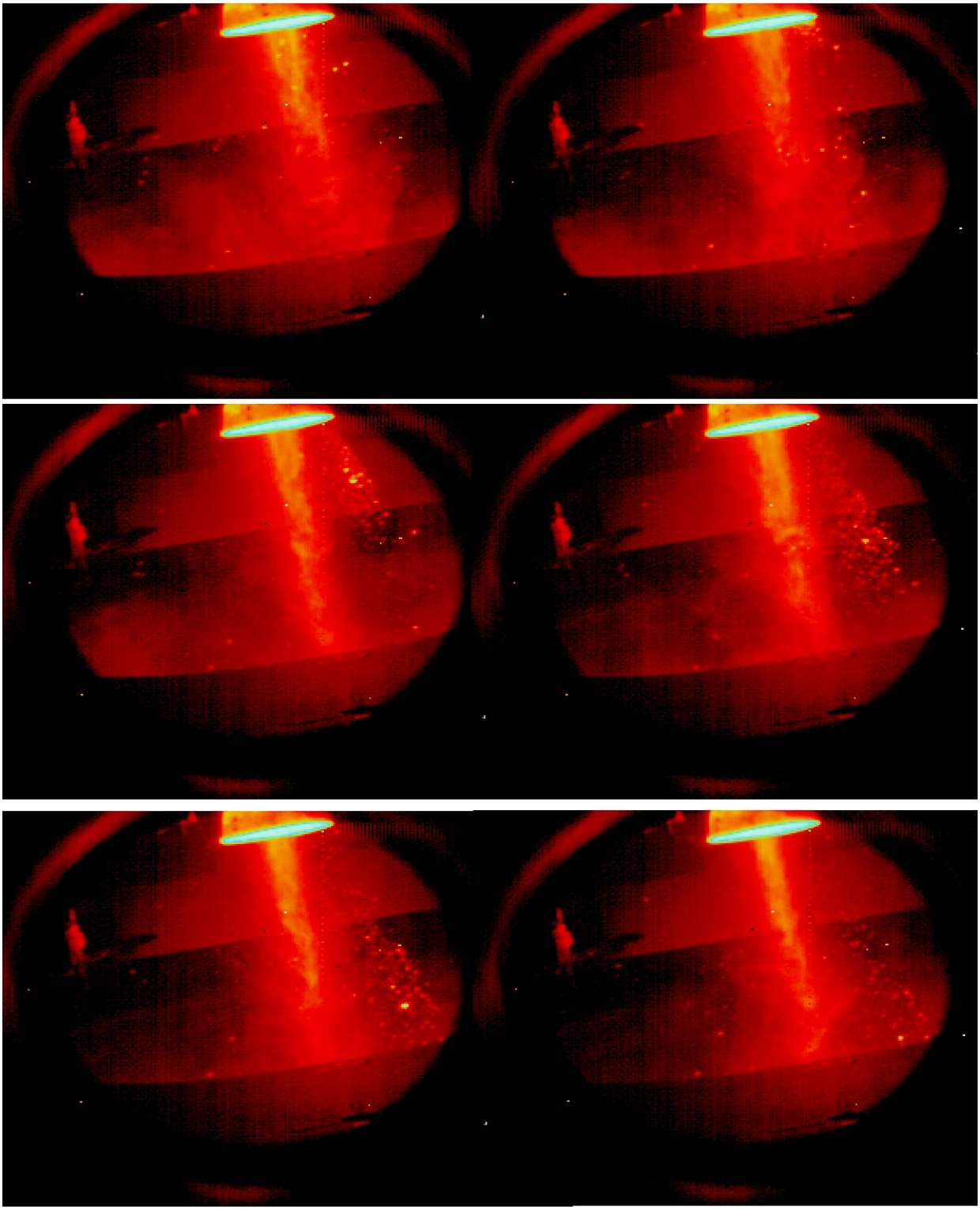

Figure 76. Star-37 SRM static spinning (60 rpm) vacuum test within the AEDC J-6 vacuum chamber. The sequence (read left to right and downward) illustrates a slag expulsion event during the beginning of Tail-off (4 seconds after onset; Chamber pressure < 6.9 kPa (< 1 psia). (Frame rate: 45 frames per second (fps))

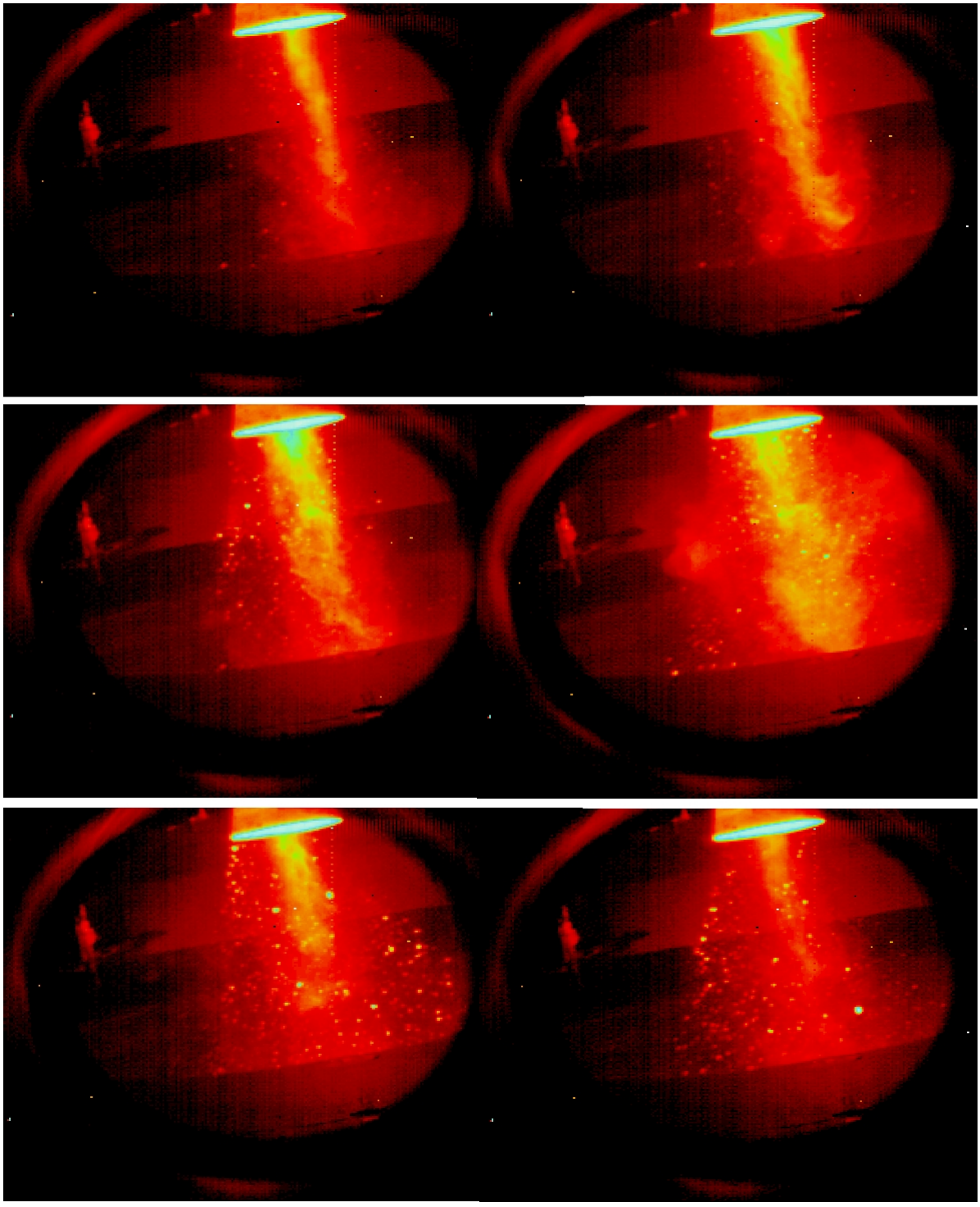

Figure 77. Star-37 SRM static spinning (60 rpm) vacuum test within the AEDC J-6 vacuum chamber. The sequence (read left to right and downward) illustrates a slag expulsion event approximately 6 seconds after the onset of Tail-off. (Chamber pressure < 6.9 kPa (< 1 psia)) (Frame Rate: 45 fps)

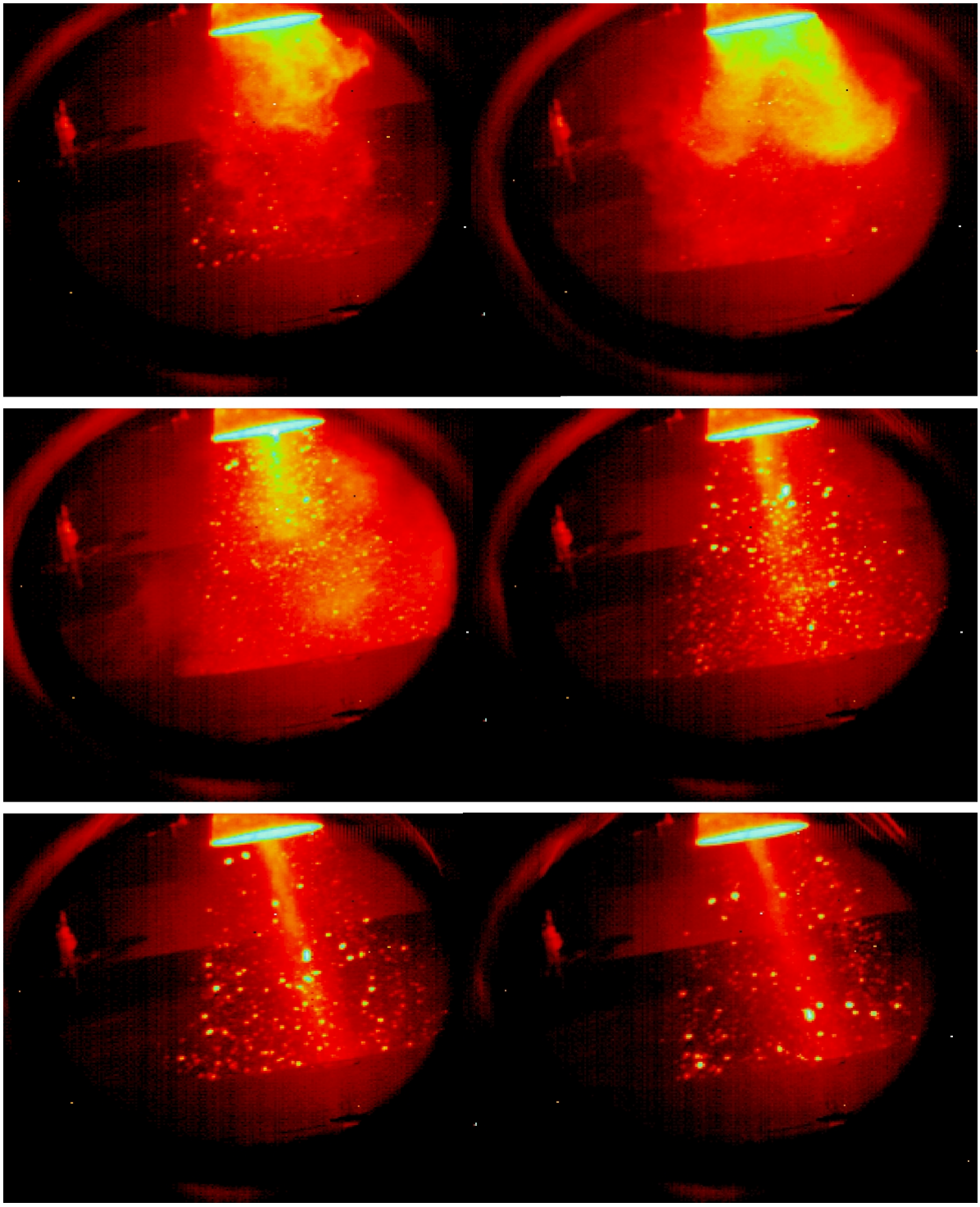

Figure 78. Star-37 SRM static spinning (60 rpm) vacuum test within the AEDC J-6 vacuum chamber. The sequence (read left to right and downward) illustrates a large slag expulsion event approximately 8 seconds after the onset of Tail-off. (Chamber pressure < 6.9 kPa (< 1 psia)) (Frame Rate: 45 fps)

Figure 79. A solidified slag particulate collected from the floor of the AEDC J-6 test chamber after the Star-37 static vacuum test. SEM microscopy (Bernhard 2004) shows that it is composed of Al_2O_3. Its flattened appearance may due to impact with the test chamber floor while still in a molten state.

I. Late Stage Tail-off Emissions

In support of missile defense system development, the U.S. Department of Defense through 1997 conducted a series of 27 missile flight tests to evaluate techniques for discriminating various targets. As part of these tests, the Tail-off phase of SRM burnout was observed repeatedly with both radar, optical and IR sensors. Although the test data available was conducted late in the Tail-off stage (when particulate emissions have significantly diminished), the data is useful in that it shows the types of capabilities which might be employed for assessment of SRMs in flight.

Figure 80 shows a Mid-Wave IR (MWIR) image of a rocket body and associated SRM late stage Tail-off ejecta. This image was acquired by a Fly-Away-Sensor Package (FASP) between 40 seconds and 100 after the beginning of Tail-off (Berstein and Sheeks 1997). Several newly ejected particles with velocities of between 1 and 20 m/s are visible with bright IR signatures indicating temperatures of > 1500 ^{o}K.

Figures 81 and 82 show Real-Time Intensity data acquired in X-Band (3 cm) by the Haystack radar of a SRM launched from Wallops Island, VA. The observations began 80 seconds after burnout at a 280 km altitude. In these traces, acquired at 120 and 134 seconds after burnout, numerous particulates are seen streaming from the SRM both toward and away from the radar. The average RCS values of about 30 separate pieces were determined and found to imply between 0.5 and 3 cm diameter. Detection below this range suffered from poor signal-to-noise ratio (Berstein and Sheeks 1997).

Figure 83 is an estimate of the particle ejection rate based upon radar data acquired in late-stage Tail-off, after bulk emission had abated. These data show the residual emission rate declining to near zero at approximately four minutes after burnout. Even at this late stage, the cumulative number over a five minute time period still exceeds 500 particles.

As evidenced by the type of capability demonstrated by AEDC in the Star-37 test, the in-situ flight assessments performed by instruments such as the FASP, while interesting, may not be necessary for orbital debris studies. As described previously, number counts and size distributions can be measured more accurately in a vacuum static test than any fiscally reasonable in-situ space experiment. The radar observations have measured utility however in that they can reveal the effluent trajectories which may be useful inputs from an orbital evolution standpoint.

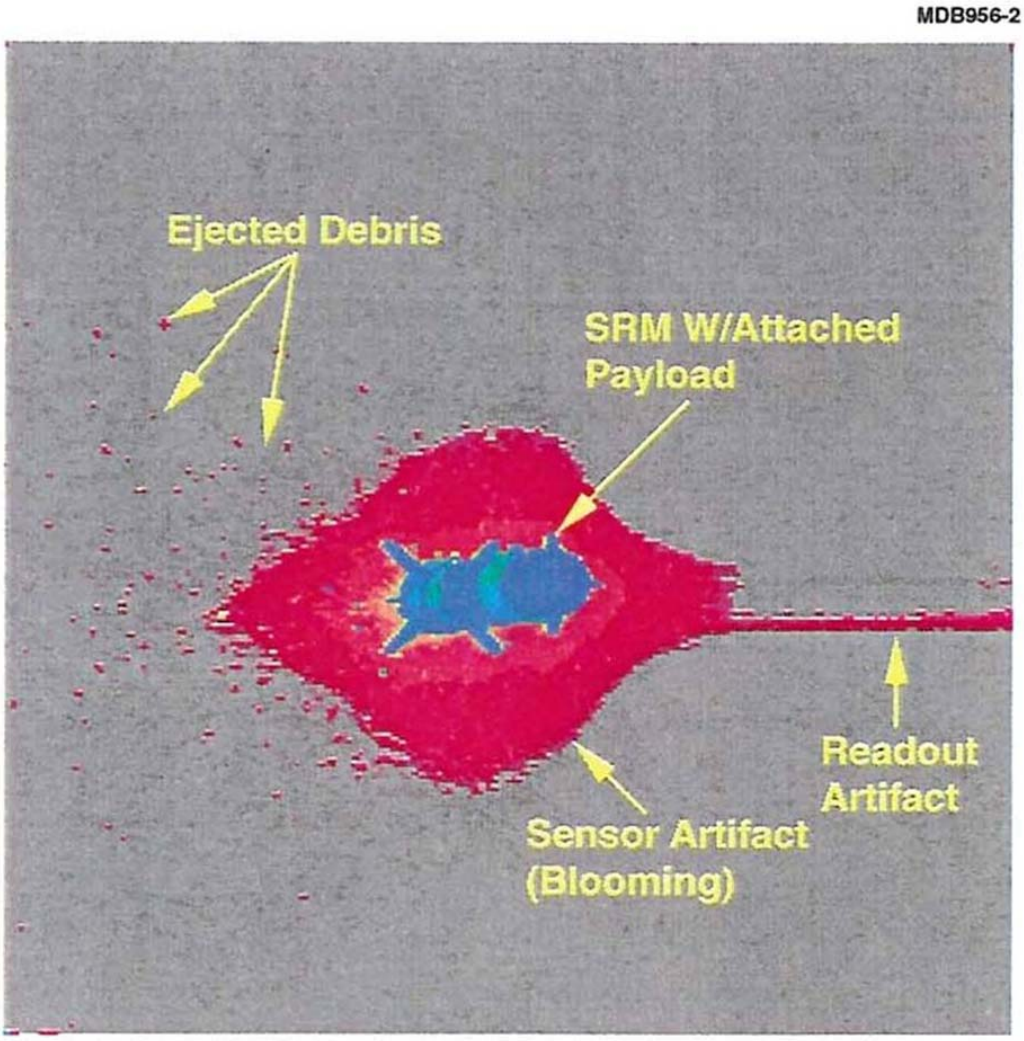

Figure 80. Mid-Wave IR (MWIR 3-5 μm) image of a rocket body and associated SRM late stage Tail-off ejecta. This image was acquired by a Fly-Away-Sensor Package (FASP) between 40 seconds and 100 after the beginning of Tail-off. (Berstein and Sheeks 1997).

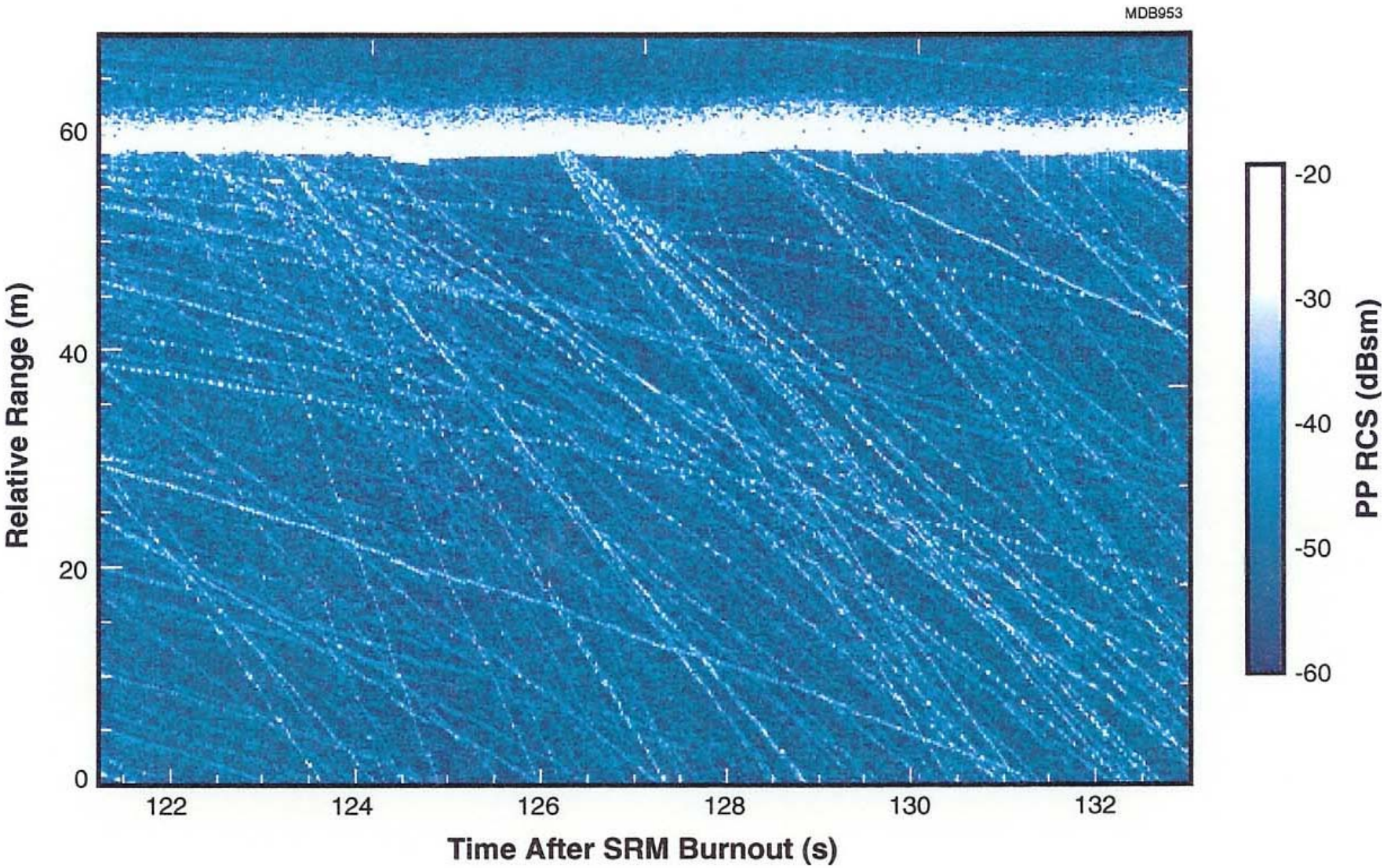

Figure 81. Range-Time Intensity (RTI) data acquired in X-Band (3 cm) by the Haystack radar of a SRM launched from Wallops Island, VA. The observations began 80 seconds after burnout at a 280 km altitude. Even at 122 seconds post-burnout, numerous particulates are seen streaming from the SRM.

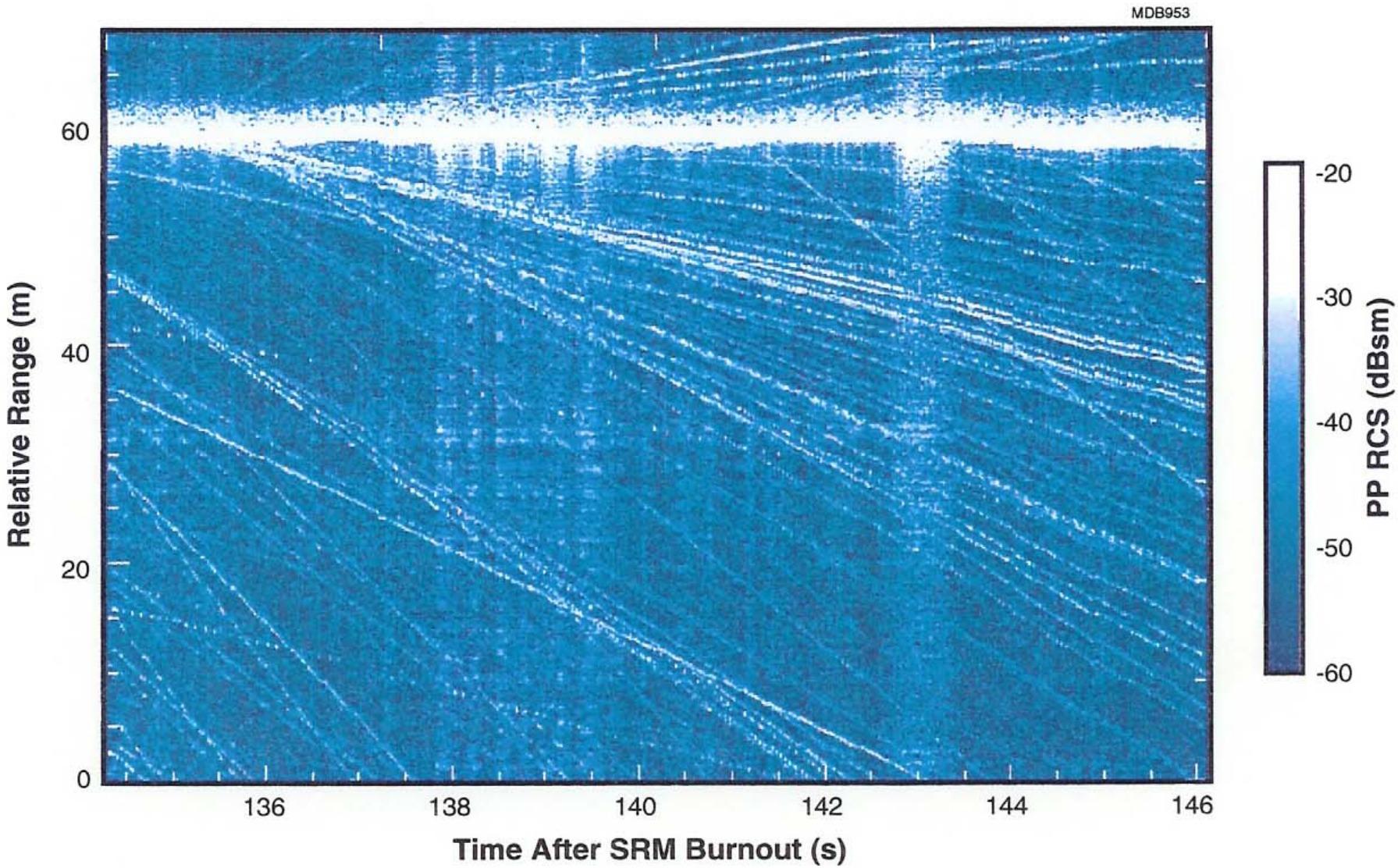

Figure 82. Range-Time Intensity (RTI) data acquired in X-Band (3 cm) by the Haystack radar of a SRM launched from Wallops Island, VA. The observations began 80 seconds after burnout at a 280 km altitude. In this trace, acquired at 134 seconds after burnout, numerous particulates are seen streaming from the SRM both toward and away from the radar.

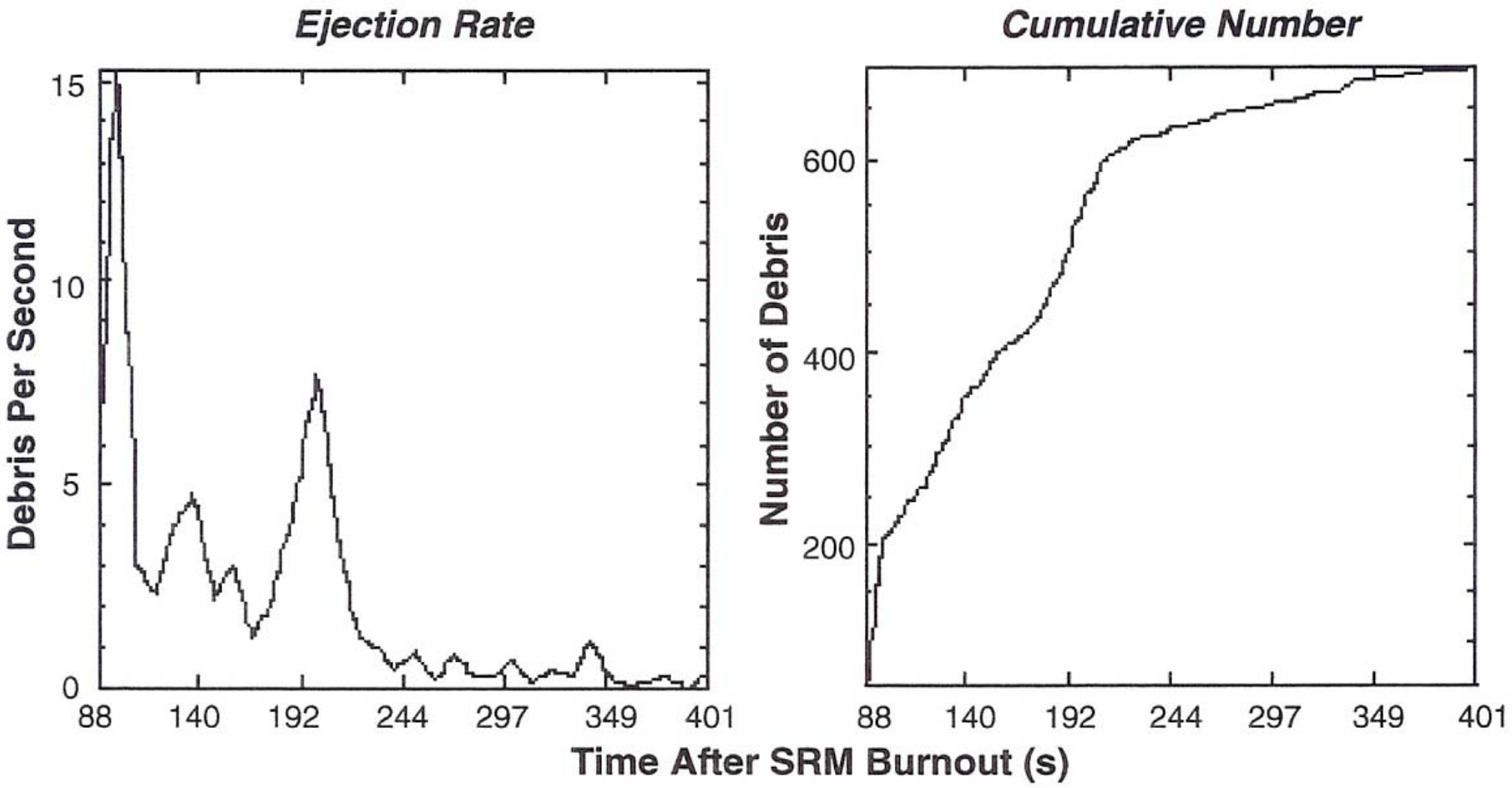

Figure 83. Acquired in the late stages Tail-off, after bulk emission has abated, these data (from radar observations) show the residual emission rate declining to near zero at approximately four minutes after burnout. Even at this late stage, the cumulative number over a five minute time period still exceeds 500 particles.

J. Summary:

The assessment that particle emissions of sufficient size to pose an orbital debris threat are reliably constrained to the Tail-off event is supported by both the physical (shearing) mechanisms as well as the available observational data. The constraint to Tail-off is important since it reduces the scope of the observational data required to assess the SRM emissions (i.e. determining the size distribution function) by emphasizing data collection only during Tail-off, and it defines a time and ejection velocity envelope for modeling purposes. It now remains to define a size distribution function.

V. Particle Size Distribution Function:

Significant effort was expended on developing a means by which in-situ observations of Tail-off emissions could be interpreted to yield an estimate of particle sizes and, ideally, an approximate size distribution function. Although the method developed, based on the time-dependent spectral and luminosity behavior of a blackbody radiator, is capable of giving accurate results, as a practical matter the technique developed has limited utility because of several inherent limitations in the available data.

Of critical importance is the presence of a calibration reference against which the luminosity of various objects can be photometrically determined. Quite fortuitously, the moon was present in the STS-93 and STS-101 in-situ data and thus the luminosity of various Tail-off objects could be determined. However the linearity (or lack thereof) of the camera was not known and the compressed nature of the analog video data probably yielded systematic photometric measurement errors. Additionally because of poor optical spatial resolution and field crowding, the measurement of a representative portion of the entire ensemble of emitted particles at a particular instant in time was problematic. Thus it was not possible to obtain a size distribution function.

Nonetheless, using luminosity and time information for individual objects, a range of particle sizes was obtained from the SRB data as well as a general weighting of object

size. Appendices I and II describe the method employed in more detail, but in summary, photometric measurements were made of the brightness of individual debris particles using the earth's moon as a calibration reference. These brightness values were then converted to luminosities by making range estimates, and then the requisite particle diameters were derived using the blackbody model shown in Figures 84-86. Figures 87-93 demonstrate the application to a set of objects selected to represent the minimum and maximum detectable size in both the near and far field. The resulting measured particle sizes were determined to be in a narrow size window representing a 2 to 5cm diameter regime. The video data itself seemed to corroborate this result, albeit subjectively, in that there seemed to be a uniformity of object size. This is partially due to logarithmic intensity compression of the data, but the overall size uniformity appears to be a real effect. Audio recoding of particulate impacts on the SRBs themselves also support this tenet, albeit loosely, as the individual pings share similar intensity and character.

Although inherent uncertainties in the photometry, range, camera response, object temperature, and object emissivity yield an estimated factor of two error in the size estimates, the results are intriguing because they demonstrate that, even with data of limited quality, in-situ measurements can yield an estimate of particle sizes. To reduce resultant uncertainties future in-situ observations could be performed using cameras with known spectral response and in pairs to yield accurate parallactic ranges. Such observations are now probably unnecessary however in light of the static vacuum test capability at AEDC – which can yield size distributions from various SRMs directly.

Anecdotally it should be noted that first and second time derivatives of the photometrically derived luminosity can also be used to differentiate particles sizes based upon the time evolution of their light curves (Matney PC, 2004). This method has the advantage of being independent of a calibration source but unfortunately requires systematically high photometric accuracy to produce meaningful results.

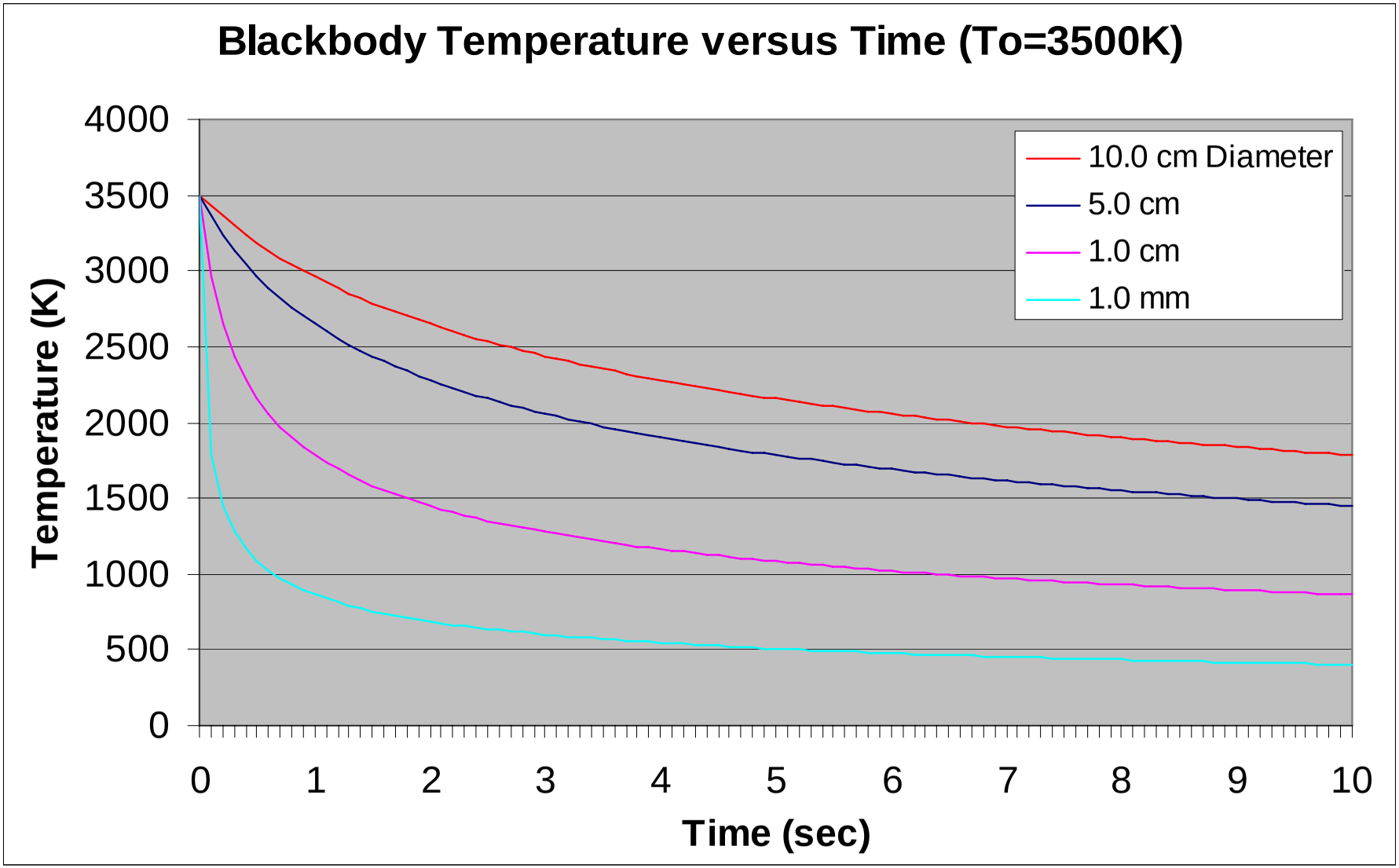

Figure 84. The decline of Blackbody Temperature versus Time for various sized aluminum oxide SRM ejecta.

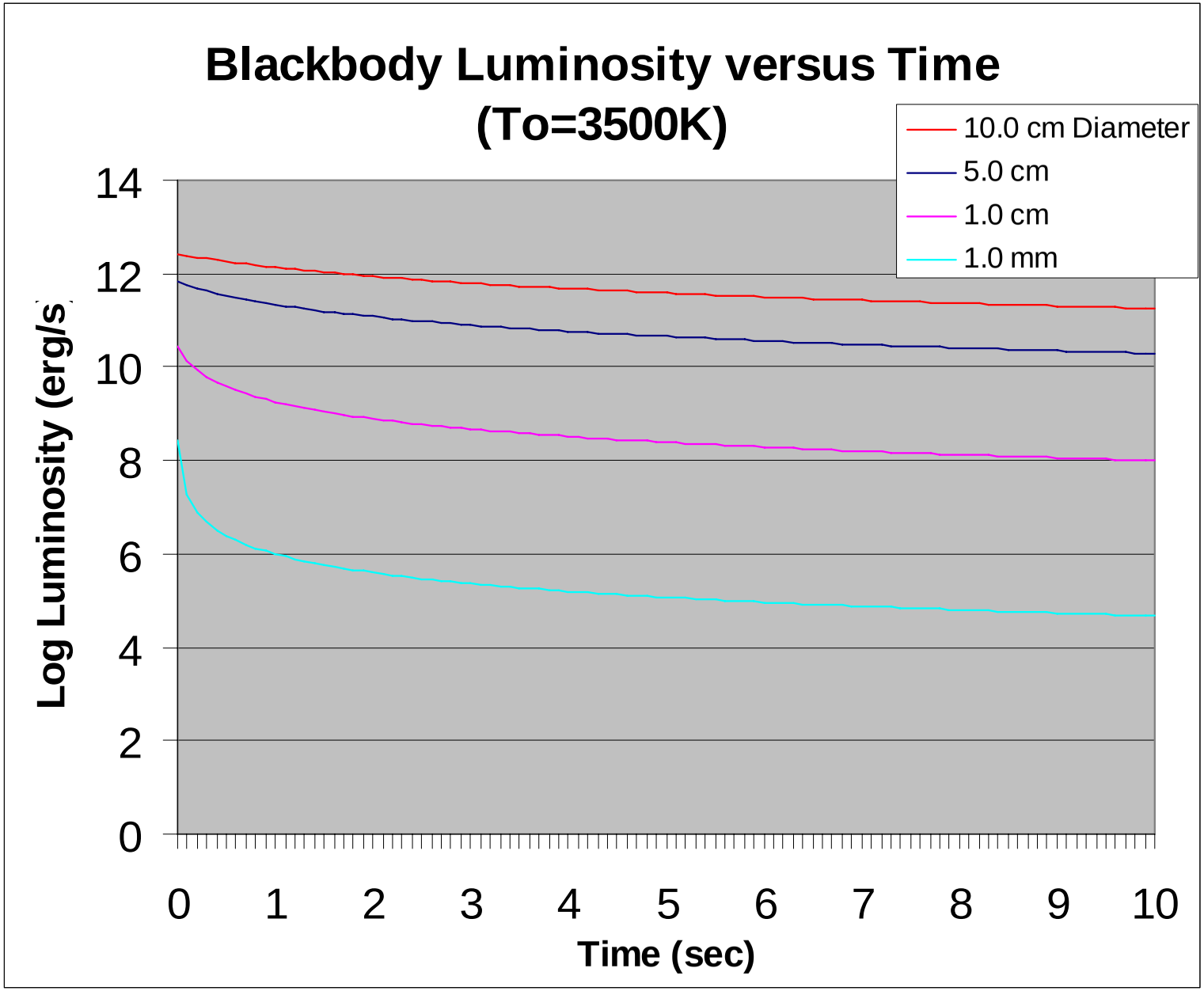

Figure 85. The decline of Total Luminosity versus Time for Al_2O_3 SRM ejecta of various sizes.

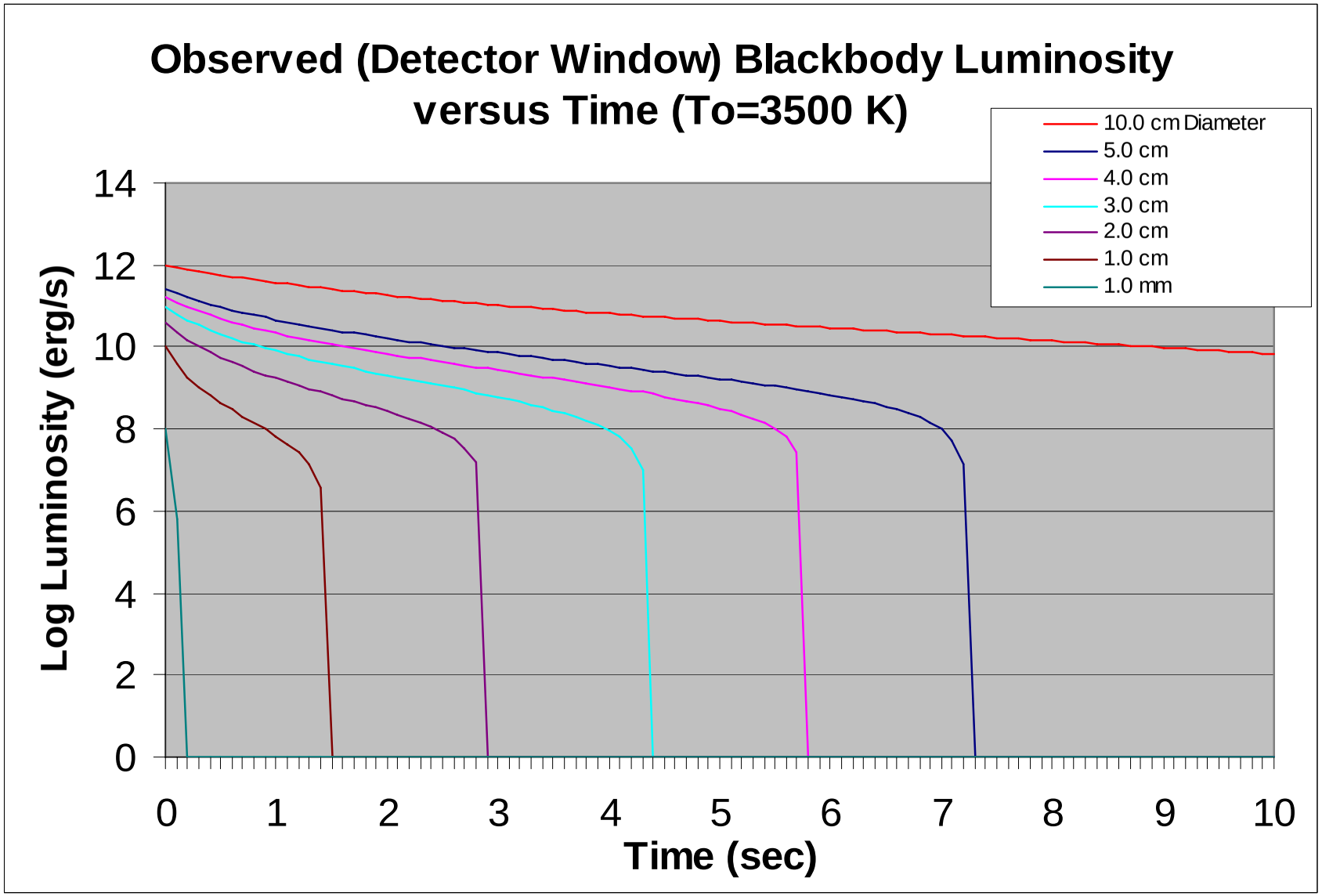

Figure 86. The decline of Observed Luminosity versus Time for Al_2O_3 particles of various sizes. This plot includes the red-ward shift of the blackbody spectrum as the objects cool. As their radiated spectrum moves away from the optical regime, they become invisible to CCD-based detectors.

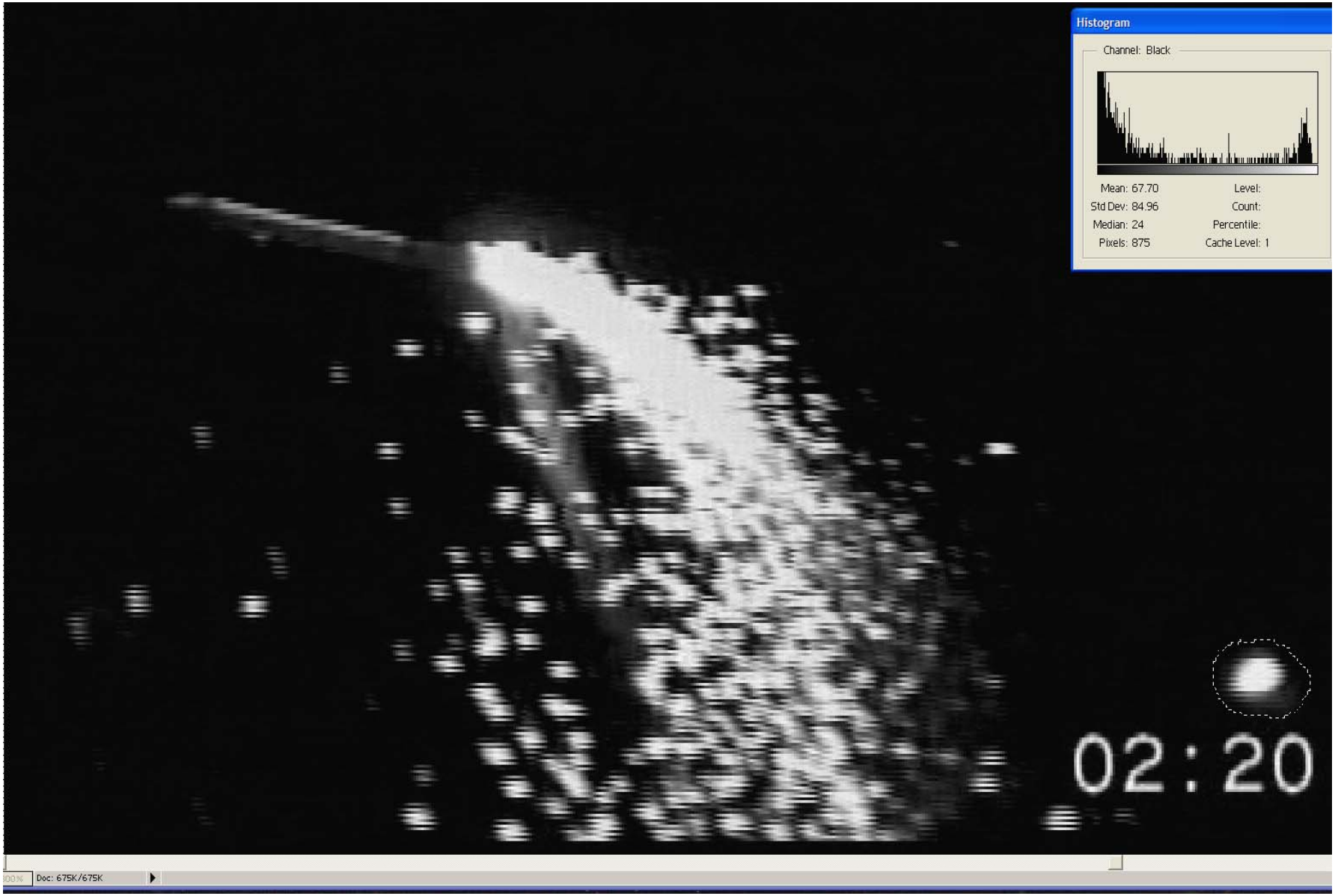

Figure 87. STS-93 Left SRB Plume Image Calibration: Night Launch, Moon Appears in Field (dotted aperture), 67% Illuminated

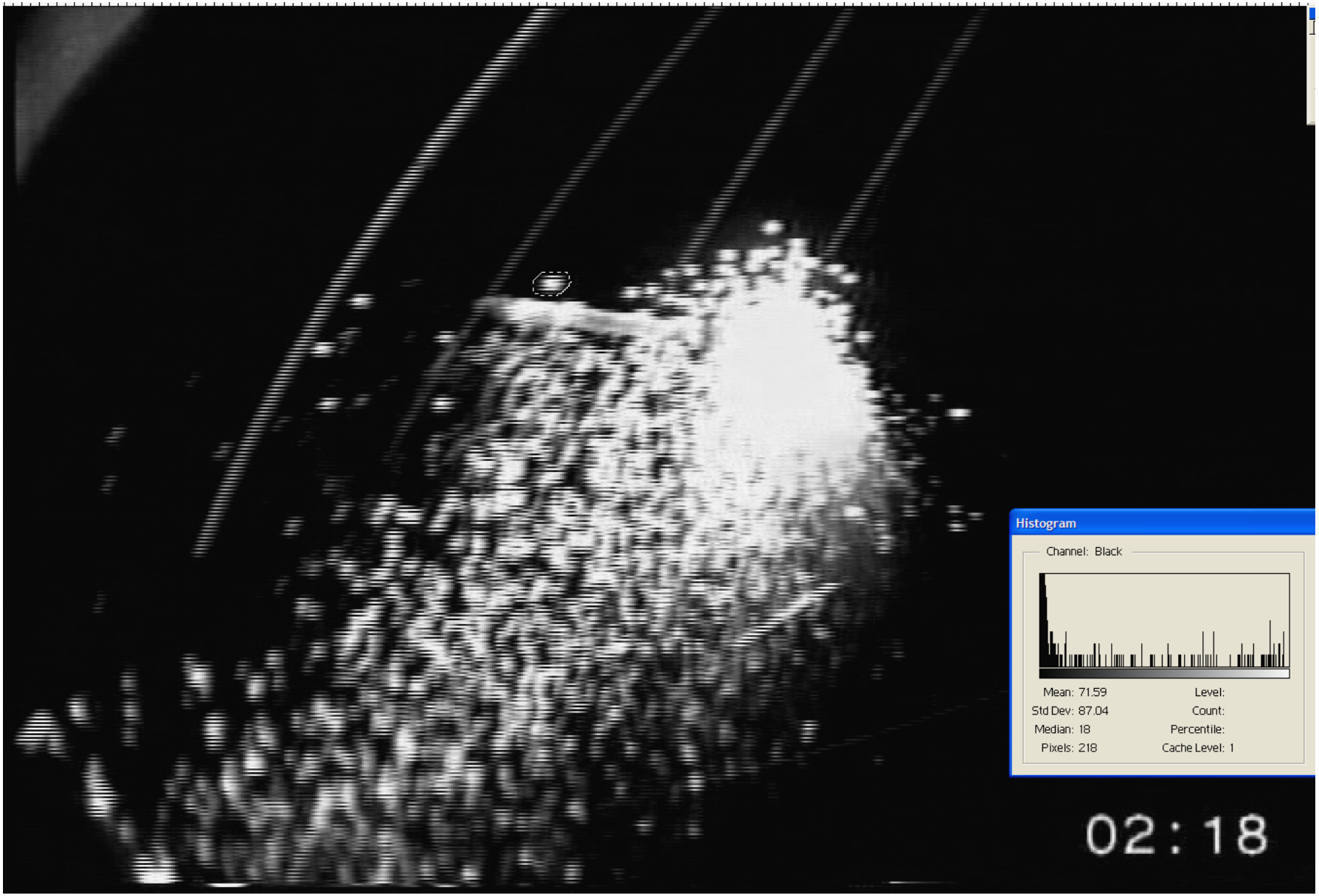

Figure 88. Aperture Photometry of STS-93 Left SRB Plume: Far-Field -Encircled Object (doted circle) is ~4 cm Diameter.

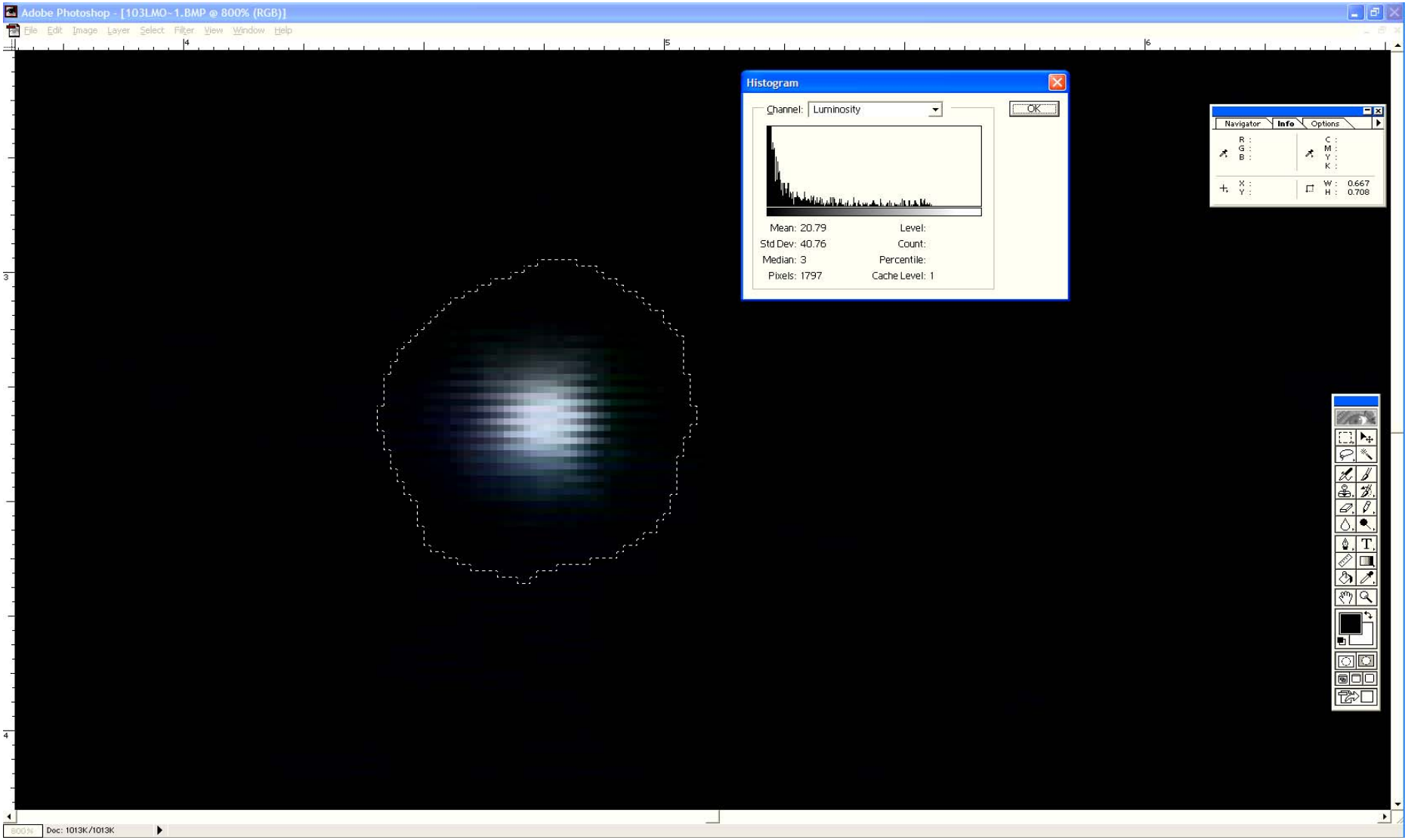

Figure 89. STS 103 Left SRB Lunar Calibration

Figure 90. STS 103 Left SRB. Age Dependent Size - Near Field: 1 to 2 cm Object of Age 1 to 3 seconds.

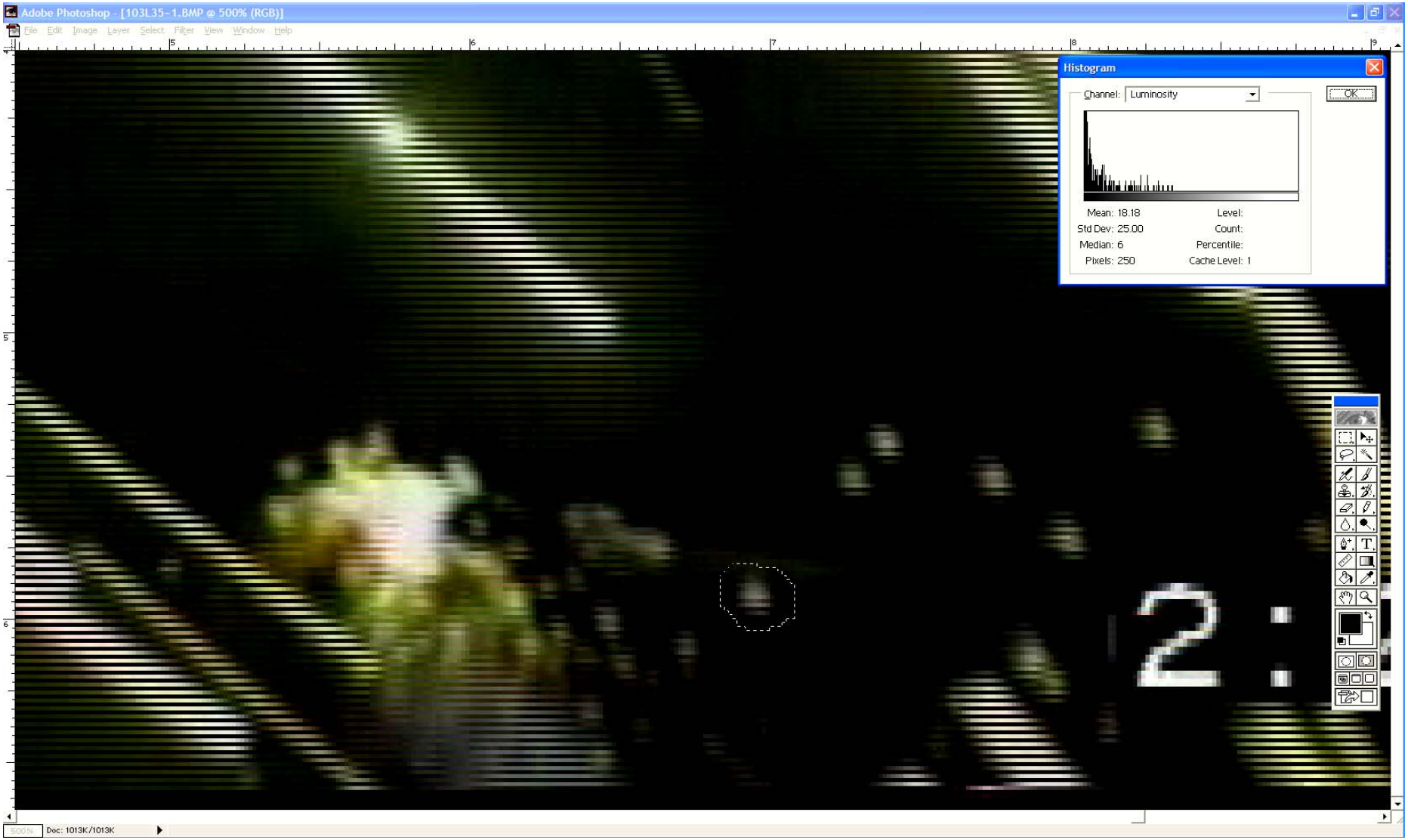

Figure 91. STS 103 Left SRB. Age Dependent Size - Consistency Check: Object Age 5 seconds implies >4cm Diameter; Photometry yields 5 cm Size.

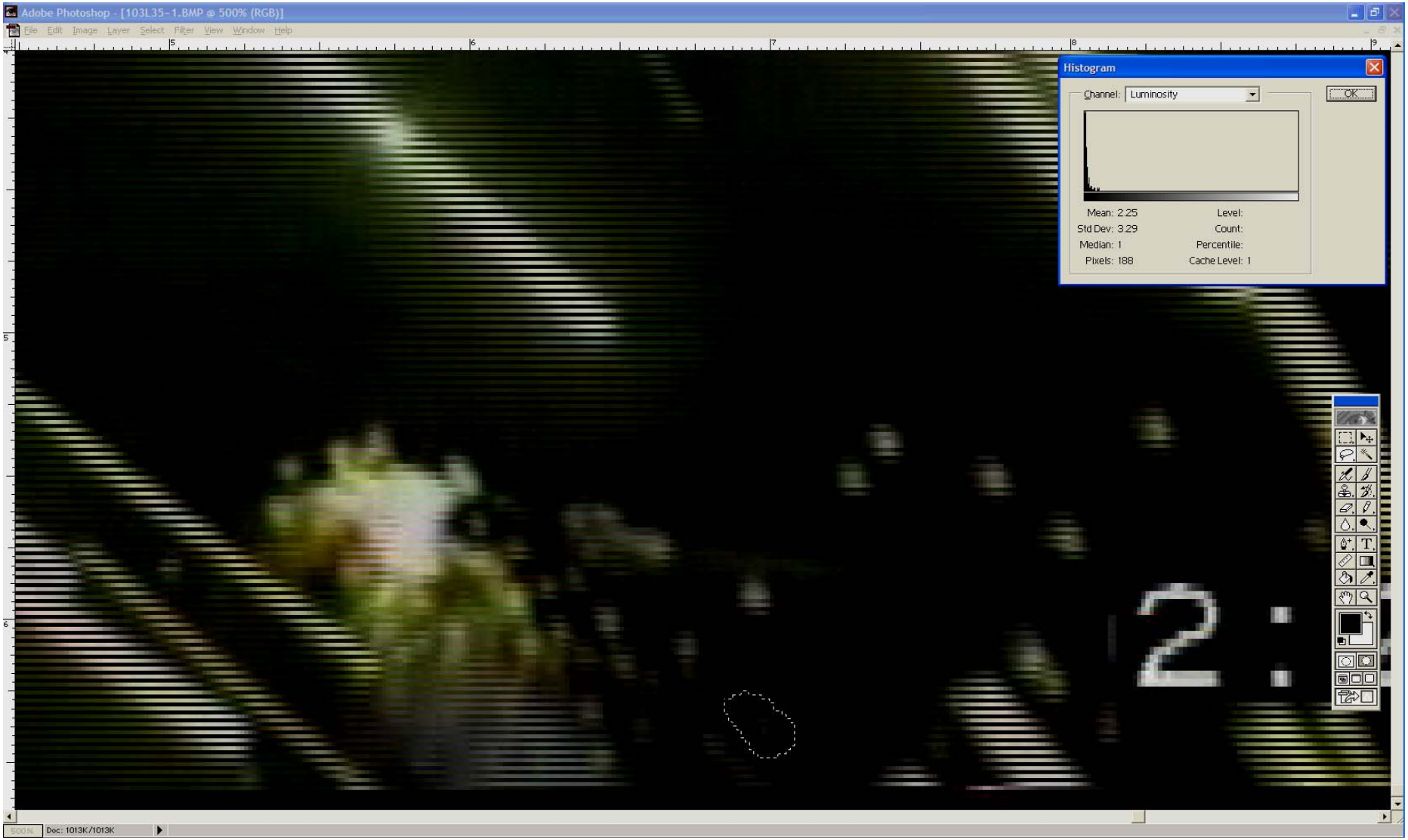

Figure 92. STS 103 Left SRB. Age Dependent Size - Consistency Check: Object Age 3.5 seconds implies >2cm Diameter. Photometry yields 3 cm Size.

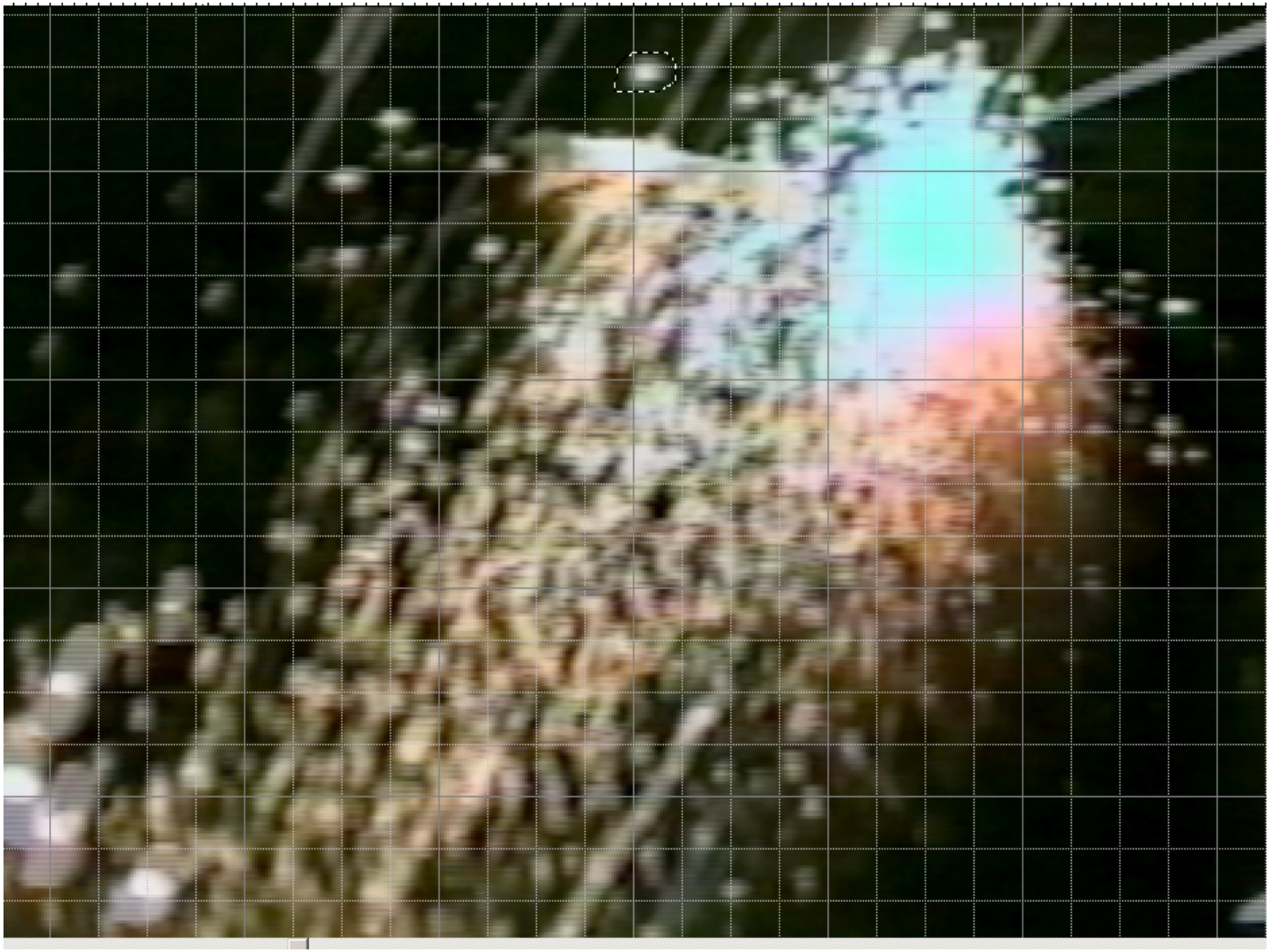

Figure 93. STS-93. This image illustrates the difficultly of generating a size distribution function from current in-situ data. Particle counts are made difficult by line of sight obscuration. Measurements and results are subject to numerous assumptions which are difficult to verify.

VI. Conclusions/Recommendations:

The ultimate objective of this research endeavor into the analysis of SRMs as a potential source of orbital debris has been to provide NASA with information sufficient to enable an incorporation of SRM emissions as a source term in environment definition models. That objective has been achieved in the following respects:

1) It is clear, via both the wealth of empirical and theoretical evidence, that large particle emissions (100 μm < D< ~5cm) from SRMs occur during Tail-off. Furthermore, large particulate emissions do not occur in significant quantity during the main burn phase of SRM activity - including losses via nozzle streaming and bulk slag ejections.

2) The available mass for the generation of large SRM particulates is related to the volume of slag that accumulates in the immersion nozzle reservoir. Static-ground tests and telemetry of flight motors indicates that 0.04 and 0.65% of the initial propellant mass is accumulated as slag. This mass is available for conversion to large Tail-off ejecta.

3) Because large particulates are emitted only at Tail-off, under conditions of reduced chamber pressure (<34.5 kPa (<5 psia)). Empirical measurements, conducted by analysis of time sequences of individual slag particle motions, indicate a representative velocity envelope for these particles of approximately 0-100 m/s. The distribution is weighted toward the lower end of the range possibly because the bulk of observed emissions occur at almost negligible chamber pressures of less than 6.9 kPa (<1 psia).

4) Empirical observations and physical arguments indicate that the majority of Tail-off emissions occur during the 30 second period that begins as the chamber pressure declines below approximately 34.5 kPa (5 psia) and on to ambient (vacuum) conditions. While particles continue to issue forth for several minutes, the flux declines rapidly - from thousands of particles per second to dozens.

5) A luminosity-time blackbody analysis of Space Shuttle SRB ejecta indicates these particulates have diameters of order 2-5 cm. Measurements of Tail-off particulates recovered after a static vacuum chamber ground test of a Star-37 SRM indicated particles diameters from 1 mm to 1.5 cm. Physical arguments place a lower range near 100 μm. Therefore essentially all Tail-off ejecta reside between approximately 100 μm and 5 cm diameter and thus can be of a size sufficiently large to pose an orbital debris threat.

A. Modeling

At this juncture a first order attempt to quantify the contribution of SRMs to the orbital debris environment is possible. Currently an updated catalog of SRM launches including comprehensive data on each individual SRM is in preparation (Anz-Meador, PC June 2004). Using this data particle orbital evolution as performed by Jackson, et al. 1997 (Figures 94 and 95) can be evaluated by initially assuming a set of properties within the parameter space thus far determined herein. For example a trial set could include:

1) Assume the full 0.65% of each SRM's propellant mass is liberated as particles.
2) A distribution function (e.g. 1/m, mass independent, or as m) ranging from 100 μm to 1 cm particles sizes,
3) A flat (or weighted) velocity distribution from 0 to 100 m/sec.
4) Emissions over a period of 30 seconds at the time and position in orbit of each SRM Tail-off phase (neglecting to first order the minimal efflux that occurs after this time window).

In light of the arguments presented here, all critical parameters are reasonably well constrained with one major exception: the size distribution function. Although various forms functional forms can be evaluated, more empirical data is needed. In this connection several collection efforts are recommended:

B. AEDC J-6 Altitude Cell Particle Collections:

It is highly recommended that a comprehensive collection regimen be employed to determine the quantity and size of particulates ejected from SRMs undergoing static tests in vacuum chambers such as the AEDC J-6 high-altitude test cell. Tail-off ejecta should be collected then separated according to size by sifting via mesh screens of descending aperture. Particles should then be sorted according to material type and then counted to yield a size distribution function for propellant-based ejecta and liner-based ejecta (if significant). Although likely labor intensive, such a process should be performed for different SRMs (propellant weights) and for different spin rates. Such an endeavor would be richly rewarding in terms of more accurately assessing both the overall SRM debris problem and constraining the size distribution function. It will also be more cost-effective

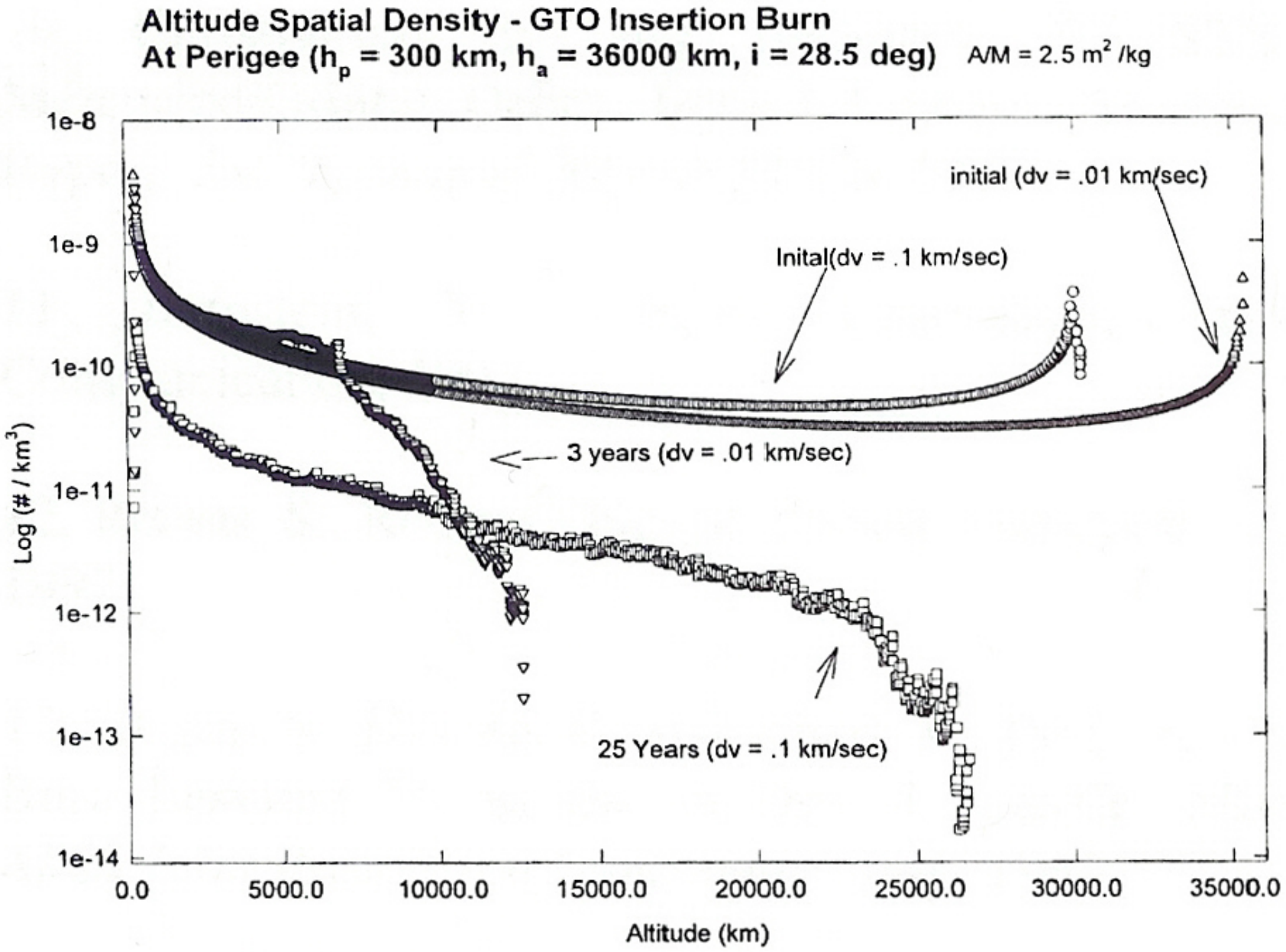

Figure 94. GEO Transfer Orbit – particulate expulsion at perigee at 10 and 100 m/sec. (Jackson, et al., 1997).

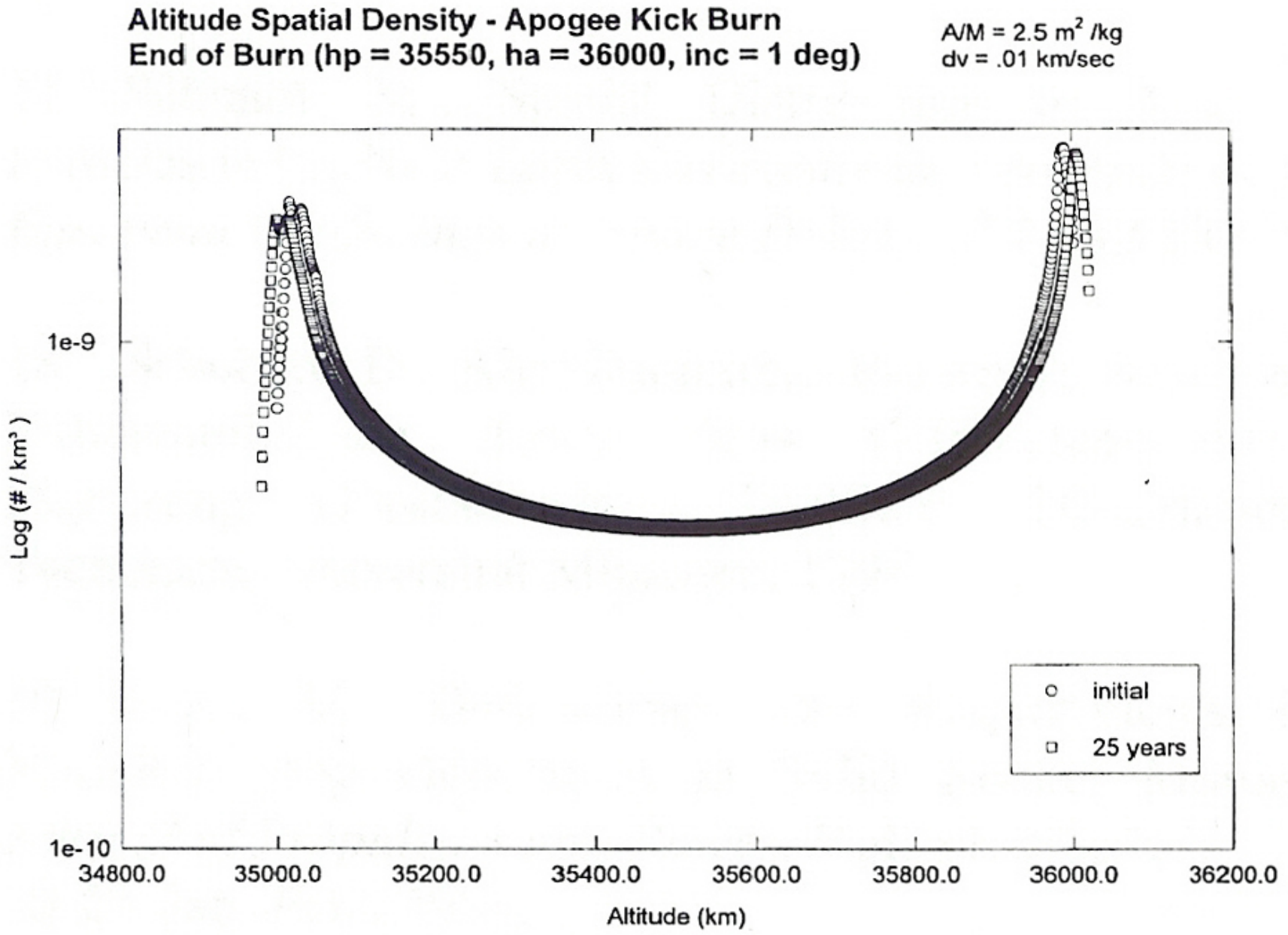

Figure 95. Apogee-Kick burn. Spatial density evolution over 25 year time. (Jackson et al., 1997).

and accurate than any conceivable in-situ mission tailored for this purpose.

It is important to note that while spin is important, its effects are of second order. The mass of evidence to date indicates that: 1) spin causes the accumulation of additional slag in SRMs during their main burn phase (Figure 96), and 2) spin tends to reduce slag emissions somewhat. This emission reduction has been observed in the very late stages of Tail-off (Bernstein and Sheeks, 1997), a minute or more after the bulk of ejection has occurred. Although ostensibly more slag is accumulated than in a non-spinning motor, there appears to be a net reduction in emissions due to coalescence on the chamber walls and a consequent inhibition of scattering and liberation from the nozzle. Lack of a complete understanding of spin's effect should in no way preclude attempts to model SRM ejecta as a significant source of orbital debris.

C. Pegasus radar and Optical Observations

Planned observations of a Pegasus launch from Kwajelein Atoll in 2005 should provide useful information about both main burn and Tail-off particulate emissions. Apart from previous high-altitude sampling, which indicated the absence of large (D>100 μm) particulates, no coordinated campaign has been conducted to fully assess the main burn phase plume content of an SRM in flight. Data from radar capable of millimeter sized detections (e.g. GBR-P) should help resolve the issue of main burn slag ejection: does it actually occur and are the resultant particles large enough to constitute an orbital debris hazard.

The generation of Range-Time-Intensity plots for the 1st stage Tail-off event should be helpful in providing a good constraint on its duration, the range of particle velocities, their angle of emission, and a limited assessment of the particle size distribution. As with optical data, number counts will likely be difficult due to congestion, but this could be rectified by tracking the descending first stage as it progresses through Tail-off rather than maintaining track on the 2nd stage. Slant range distance evaluation of the 1st and 2nd stages will resolve the optimum operating procedure. Third stage tracking is probably not practical due to range constraints (Figure 97).

To assist mission planners a very preliminary prediction of particle size and number count was made for the Tail-off phase of each stage assuming 0.5% of the propellant mass was converted to slag and that this was fully liberated as ejecta with a 1/m size distribution. The results which indicate the very large number anticipated are listed in Table II.

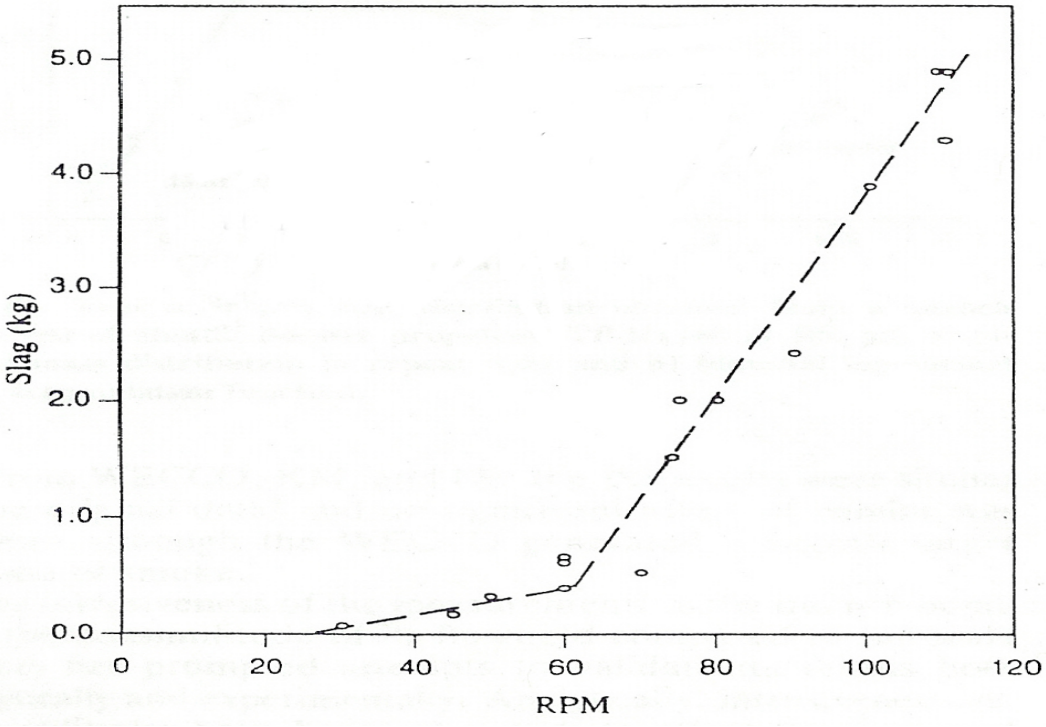

Figure 96. Slag deposition history or a Star-48 SRMs spinning at various rates. Agglomerates, that would otherwise escape through the nozzle during the main burn, are driven outward to the chamber walls by centrifugal force (e.g. 2 Gs for a 1 m diameter motor spinning at 60 rpm). At Tail-off, although more slag is ostensibly available for ejection, centrifugal effects may recapture many of the particulates leading to a net reduction of emissions. (Salita 1995)

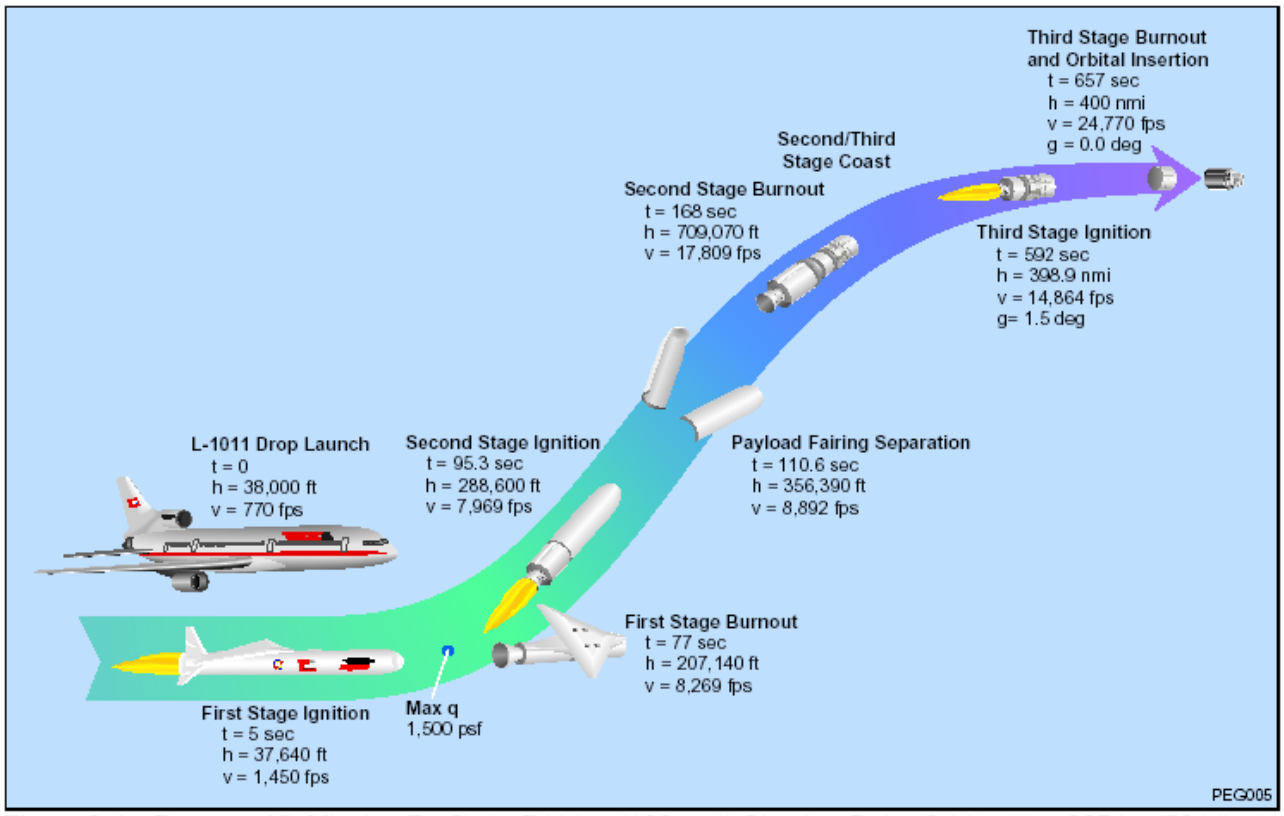

Figure 97. Flight profile for the Pegasus Launch vehicle.

Table II. Anticipated Tail-off particle production for Pegasus 1st, 2nd, and 3rd stages, assuming 0.55 conversion of propellant to ejected slag and 1/m mass distribution.

First Stage – Orion 50S w/ 12,000 kg propellant
→ 60 kg available slag mass at ~4 grams/cc
→ 3000 particles > 1 cm diameter particles at Tail-off
300,000 > 1 mm diameter,
30,000,000 > 100 μm diameter

Second Stage – Orion 50 w/ 3,000 kg propellant
→ 15 kg available slag mass at ~4 grams/cc
→ 750 particles > 1 cm diameter particles at Tail-off
75,000 > 1 mm diameter,
7,500,000 > 100 μm diameter

Third Stage – Orion 38 w/ 700 kg propellant
→ 3.5 kg available slag mass at ~4 grams/cc
→ 170 particles > 1 cm diameter particles at Tail-off
17,000 > 1 mm diameter,
1,700,000 > 100 μm diameter

The bulk ejection of the particles listed in Table II will occur over a 10 to 20 second period with delta velocities of 0 to 100 m/sec (relative to the vehicle). For the volume of interest the line-of-sight range (radial dimension of plume) will expand to ~200 meters in 20 seconds (based on Haystack RTI data of other events – Figures 81 and 82). For stages 1, 2, and 3 this yields particle densities of 10,000 to 1 particles per cubic meter for sizes > 1mm depending primarily on the proximity to the nozzle (ie. time for diffusion).

Optical observations are also planned but will be of limited utility. Based upon data already acquired (Section IV.F.), the particles ejected from Pegasus are small and the largest particles are not particularly luminous or numerous (<3000 @ 1+ cm diameter). Optical observations similar to shuttle SRB observations will probably not resolve individual objects (e.g. a moderate aperture telescope (10-50 cm) with a long focal length (10 m) and high speed CCD with 1 arcsec pixels will have a ~25 cm spatial resolution at 60 km.) Due to the extended range (> 80 km), the situation is even more untenable for the 2nd and 3rd stages. Although the idea of simultaneously observing an ejected SRM particle both optically and with radar is tantalizing, ideal circumstances will be required including primarily a plethora of very large particles – which is unlikely. A night launch would greatly enhance the possibility of optical detection.

D. Other Observations (Ground-Based or In-situ; Optical/IR or Radar) and SRM Physical Modeling

In light of the existence of the AEDC J-6 test cell, and the planned Pegasus observations, the author is dubious as to whether an investment in additional enhanced observations via remote sensing or in-situ (Optical/IR or Radar) is worthwhile. The existing data available regarding SRM emissions, acquired with the highest-quality assets and at prodigious expense, has been more than adequate in facilitating a reasonable assessment of all essential characteristics with only one exception - the size distribution function. Tangible empirical data is difficult with which to argue and J-6 particle collection can constrain the size distribution more directly than any conceivable cost-effective sensing operation. The methods applied herein to SRB in-situ data analysis, although useful in the absence of tangible data, are prone to high uncertainties when applied to size estimation and illustrate the problems which must be overcome. In the author's opinion, with the availability of ground vacuum test data, the need for observations, beyond what already exists or is planned, is not supported.

Arguably the test cell cannot duplicate the high axial accelerations experienced during a space firing, however this should only affect the size of the slag pool, not the boil-over and liberation mechanisms. Telemetry data already assesses slag pool masses in space-fired SRMs and this accounting has been made in the 0.65% upper constraint on accumulated slag mass as a percentage of initial propellant mass. At this time, remote or in-situ measurements simply cannot feasibly derive a distribution function as reliably as a (vacuum) static test.

These statements only support static vacuum testing. Non-vacuum static testing at atmospheric pressure has been immensely useful for evaluating slag formation, but because boil-over either does not occur or is severely curtailed, the size and mass distribution functions derived from such tests cannot represent the vacuum or actual space distribution functions. The extent to which the space motor distribution function is skewed relative to atmospheric ground test results cannot be known without a greater understanding and integration of the physical processes involved than is currently the case. Therefore the testing effort should be directed to static vacuum condition. Since these tests (from a performance perspective) are performed routinely at AEDC, data collection may be possible at quite minimal cost.

Lastly the issue of theoretical size distribution modeling should be addressed. Some effort was expended trying to approach the determination of an SRM particle size distribution via analogs to comparable physical systems. For example the closest identifiable analogy to an on-orbit boil-over mechanism was the 1997 work of C. Wiedemann and P. Wegener (IFR/TUBS) who modeled violent boil-over in RORSAT NaK coolant ejection based upon the behavior of liquid water flash evaporating into a vacuum. The assumptions built into such models and those that must then be employed to make the extrapolation to the behavior of SRM slag render such an approach unreliable in this application. Once again tangible data from a ground vacuum test cell is the best available source for generating the necessary size distribution function.

This discussion is not intended to imply that more data, regardless of its nature, is not useful. The return to flight of the Space Shuttle in the wake of the Columbia catastrophe will be supported with numerous in-situ cameras with views like that shown in Figure 98. Data from these cameras will certainly assist incrementally in a more complete understanding of SRM (SRB) behavior. Specifically, some of these cameras should contain views of the SRB aft end during the first five seconds after SRB separation and thus show the earliest phase of SRB Tail-off emissions. Ancillary SRM data from sources with alternate primary objectives can still contribute meaningfully to our understanding.

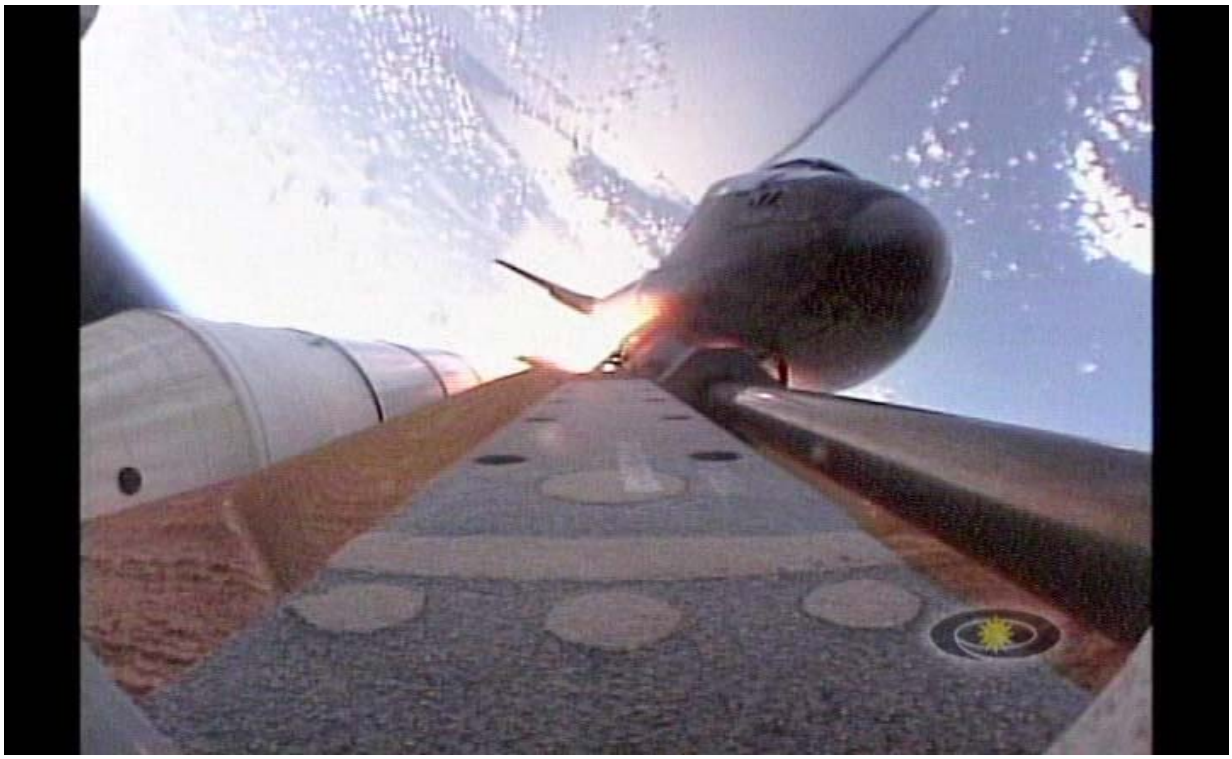

Figure 98. Space Shuttle Reurn-to-flight mission will have multiple camera enhancements (three per SRB with one aft pointed). (STS-112 Rocket Cam Image by Ecliptic Enterprises Inc.).

References

Akiba, R,, and Inatani, Y., Alumina Particles Exhausted from Solid-Propellant Rocket Motors as a Potential Source of Space Debris, Unpublished, January 1990.

Anz-Meador, Personal Communication, Embry-Riddle, 2004.

Bendisch, J. et al., Final Report: Upgrade of ESA's MASTER Model, ESA, June 2000.

Bernhard, R., SEM Analysis of SRM Slag Debris, NASA Internal Report, 2004.

Bernhard, R., and Christiansen, E., STS-73 Meteoroid/Orbital Debris Impact Damage Assessment Report, JSC Technical Report 27323, 1995.

Bernstein, M.D. and Sheeks, B.J., Field Observations of Medium-Sized Debris From Post-Burnout Solid-Fuel Rocket Motors, SPIE Vol. 3116, July 1997.

Blomshield, F.S., Kraeutle, K.J., and Stalnaker, R.A., Shuttle Redesigned Solid Rocket Motor Aluminum Oxide Investigations, 21st JANNAF Plume Conference, October 1994.

Brandon, M., Davis, C., Fette, M., Reed, R., Wilcher, G., Winkleman, B., Star-37 Plume Radiative Heat Transfer Test, AEDC Internal Document, 2004.

Burris, R.A., Orbiter Surface Damage to SRM Plume Impingement, MDTSCO Design Note No. 1.4-3-016, December 1978.

Drakes, J.A., Pruitt, D.W., Reed, R.A., McGregor, W.K., Hiers, R.S., and Fulkerson, S.A., Sensitivity of SRM Plume Radiation to the Details of Aluminum Oxide Crystallization, 22nd JANNAF Plume Meeting, October 1995.

Girata, P.T., McGregor, W.K., and Quinn, R., AEDC-TMR-E55, Arnold Air Force Station, 1981.

Greenwood, T.F., Lee, Y.C., Bender, R.L., and Carter, R. E., Calculation of Shuttle Base Heating Environment and Comparison With Flight Data, Proceedings of NASA Langley Research Conference, Publication 2283, 1983.

Hill, J.A., Ruttenberg, E.C., and Netzer, D.W., Spatial Variations In Aluminum Oxide and Zirconium Oxide Particle Sizes In Rocket Motors and Plumes, 23rd JANNAF Conference, April 1997.

Horz, F., Bernhard, R.P., See, T.H., Kessler, D.J., Metallic And Oxidized Aluminum Debris Impacting The Trailing Edge Of The Long Duration Exposure Facility(LDEF), Space Debris, 2, 51-66, 2002.

Horz, F., Bernhard, R.P., See, T.H., and Brownlee, D.E., Natural and Orbital Debris Particles on LDEF's Trailing and Forward Facing Surfaces, LDEF – 69 Months In Space, Levine, A.S, editor, Third Post-Retrieval Symposium, NASA CP 3275, pp.415-430, 1993.

Hunley, J.D., "The History of Solid-Propellant Rocketry: What We Do And Do Not Know", NASA Dryden Flight Research Center, AIAA, 99-2925, June 1999.

Jackson, A., Eichler, P., Reynolds, R., Potter, A., and Johnson, N., The Historical Contribution of Solid Rocket Motors to the One Centimeter Debris Population, NASA Internal Document, 1997.

Jenkins, D., R., "Space Shuttle: The History of the National Space Transportation System – The First 100 Missions", ISBN 0-9633974-5-1, Voyageur Press, 2002.

Kavanaugh, D.J., and Nichols, C.C., A Post Burn Out-gassing and Thrust Prediction for the IUS Solid Rocket Motors, AIAA-80-1104, 16th Joint Propulsion Conference, 1980.

Kessler, D., Origin of Orbital Debris Impacts on LDEF's Trailing Edge, LDEF – 69 Months In Space, Levine, A.S, editor, Second Post-Retrieval Symposium, NASA CP 3194, pp.585-594, 1992.

Laredo, D., Kellman, L., Eno, T., and Netzer, D., Particulate Behavior in Exhasut Nozzles and Plumes, 19th JANNAF Plume Conference, May 1991.

Liou, J.C., Matney, M.J., Anz-Meador, P.D., Kessler, D., Jansen, M., Theall, J.R., The New Orbital Debris Engineering Model ORDEM2000, NASA/TP-2002-210780, May 2002.

Loftus, J.P., and Brasher, W.L., Beyond Low Earth Orbit: An Overview of Orbit-To-Orbit Stages, IAF-85-141, 1985.

Matney, Mark, Personal Communications, NASA-JSC, 2004.

Mueller, A.C. and Kessler, D., The Effects of Particulates From Solid Rocket Motors Fired In Space, Space Review, Vol.5, No. 9, pp. 77-86, 1985.

Myer, R.X., In-Flight Formation of Slag in Spinning Solid Propellant Rocket motors, Journal of Propulsion and Power, Vol. 8, 45-50, 1992.

Ojakangas, G.W., Anderson, B.J., and Anz-Meador, P.D., Solid-Rocket-Motor Contribution to Large-Particle Orbital Debris Population, Journal of Spacecraft and Rockets, Vol. 33, No. 4, July- August 1996.

Oliver, S. M., Reed, R. A., Hiers, R. S., and Simmons, M. A., Super-cooling of Liquid Al_2O_3 Droplets in Solid-Propellant Rocket Exhaust Plumes: Fact or Fiction?, 18th JANNAF Plume Conference, November 1989.

Price, E.W., and Sigman, R.K., The Al and Al_2O_3 Droplet Cloud in Solid Rocket Motors, 21st JANNAF Plume Conference, October 1994.

Reed, R. A., Summary of Al_2O_3 Plume Characteristics and Behavior, 21st JANNAF Plume Conference, October 1994.

Reed, R.A., Cox, D.B., Wilcher, W.A., Watkins, W.A., Truesdale, M.A., Simmons, M.A., and Roberds, D.W., Solid-Propellant Rocket Motor Exhaust Plume Measurements and Analysis, 19th JANNAF Plume Conference, May 1991.

Reed, R.A., Possible Effects of Solid Rocket Motor Slag Ejection Upon the Space Station Environment, NASA Private Communication, January 1991.

Reynolds, R., Johnson, N., Potter, A., Orbital Debris From Solid Rocket Motor Slag, IAF-96-V.6.04, 47th International Astronautical Congress, Beijing, October 7-11, 1996.

Rudman, S., Mead, H., and Pagnutti, M., Particle Agglomeration Effects in Solid Rocket Motor Nozzles and Plumes, 19th JANNAF Plume Conference, May 1991.

Salita, M., Deficiencies and Requirements in Modeling of Slag Generation in Solid Rocket Motors, Journal of Propulsion and Power, Vol. 11, No.1, pp. 10-23, Jan-Feb 1995.
Salita, M., Predicted Slag Deposition Histories in Eight Solid Rocket Motors Using The CFD Model "EVT", AIAA-95-2728, JANNAF Propulsion Conference, July 10-12, 1995.

Salita, M., Survey of Recent Al_2O_3 Droplet Size Data in Solid Rocket Chambers, Nozzles, and Plumes, 21st JANNAF Plume Conference, October 1994.

Salita, M., Workshop Report: Modeling of Slag Generation in Solid Rocket Motors, 30th JANNAF Interagency Combustion Meeting, October 1994.

Sambamuthi, J., Al_2O_3 Collection and Sizing from Solid Rocket Motor Plumes, Journal of Propulsion and Power, Vol. 12, May-June 1996.

Stansbery, et al., Haystack RADAR Measurements of the Orbital Debris Environment: 1990-1994, NASA-JSC Technical Report JSC-27436, April 1996.

Thompson, D.W. and Schade, C.C., Pegasus and Taurus Launch Vehicles, American Institute of Aeronautics and Astronautics (AIAA), 1990.

Tobias, Mark, Personal Communications with ATK/Thiokol 2004.

Varsi, G., Particulate Measurements, Space Shuttle Environmental Assessment Workshop on Stratospheric Effects, JSC TM X-58198, 1977.

Wiedemann, C., and Wegener, P., United Nations Document, IFR/TUBS, 1997.

Appendix I

Derivation of Time-Dependent Blackbody Luminosity Function

The general expression for the Energy (E) of a radiating blackbody of Luminosity (L) at Time (t) is given by:

$$E(t) = E_0 - \int_0^t L(t)dt$$

The energy of the object can be related to its Mass (m), Heat Capacity(c), and Temperature (T) by the expression:

$$E(t) = mcT(t)$$

The luminosity is given my the Stephan-Boltzman Law:

$$L(t) = 4\pi r^2 \sigma T^4$$

Substituting and differentiating this becomes a 4th order differential equation of form:

$$T' = -\alpha T^4 \qquad \alpha = \frac{3\sigma}{r\rho c}$$

Where c = 9M erg/g-^{o}K for Al; r is the particle radius (cm); σ =5.67E-5 erg/cm^2-s-^{o}K^4; and rho = 1.6 g/cm^3 for Al_2O_3.

With solution for Temperature as a function time T(t):

$$T(t) = (3\alpha t + \frac{1}{T_0^3})^{-\frac{1}{3}}$$

The total integrated Luminosity (L) is thus given by:

$$L(t) = 4\pi r^2 \sigma (3\alpha t + \frac{1}{T_0^3})^{\frac{-4}{3}}$$

Because the Detector has limited Spectral Sensitivity, the actual luminosity perceived is given by integrating the Planck function over the detector (assumed linear) wavelength response (0.4 to 1.0 μm). This is the Video Camera Optical Region Spectral Response Convolved with BB Spectrum:

Speed of Light c = 2.99810 cm / s
Planck's Constant h = 6.626 E - 27 erg - s
Boltzman's Constant k = 1.38 E - 16 erg / K
Temperature (K) T

Planck Function Integrated over Video Camera Spectral Response
(Averaged Flat from 0.4 to 1.0 um)

$$\text{Interated Windowed response} = \int_{c/10^{-4}}^{c/4\,E10^{-5}} \left[\frac{2\,\pi\,h\,\nu^3}{c^2\,(e^{((h\,f)/(k\,T))}-1)}\right] d\nu$$

```
=   4.631994583599643`*^-47
  (-7.687123044616528`*^58 - 5.612063034856628`*^53 T Log[1 - e^(14394.744927536234` /T)] +
    8.768848491963482`*^54 T Log[1 - e^(35986.86231884058` /T)] -
    1.1696066300114376`*^50 T^2 PolyLog[2, e^(14394.744927536234` /T)] +
    7.310041437571484`*^50 T^2 PolyLog[2, e^(35986.86231884058` /T)] +
    1.6250466901626774`*^46 T^3 PolyLog[3, e^(14394.744927536234` /T)] -
    4.0626167254066933`*^46 T^3 PolyLog[3, e^(35986.86231884058` /T)] -
    1.1289166277994034`*^42 T^4 PolyLog[4, e^(14394.744927536234` /T)] +
    1.1289166277994034`*^42 T^4 PolyLog[4, e^(35986.86231884058` /T)])
```

The Detector Window to Full Spectrum Ratio ($F\{T(^oK)\}$) is thus given by the ratio of the convolved response to the full response:

Integrated Over All Frequency

$$\int_0^\infty \left[\frac{2\pi h \nu^3}{c^2 \left(e^{((h f)/(k T))} - 1\right)}\right] d\nu = \sigma T^4 \qquad \sigma = 5.67\,E-5 \;\; erg/cm2-s-K$$

Window / Full Spectral Response Ratio =

$$\frac{1}{T^4}$$

```
(8.169302616577854`*^-43
  (-7.687123044616528`*^58 - 5.612063034856628`*^53 T Log[1 - e^(14394.744927536234` /T)] +
    8.768848491963482`*^54 T Log[1 - e^(35986.86231884058` /T)] -
    1.1696066300114376`*^50 T^2 PolyLog[2, e^(14394.744927536234` /T)] +
    7.310041437571484`*^50 T^2 PolyLog[2, e^(35986.86231884058` /T)] +
    1.6250466901626774`*^46 T^3 PolyLog[3, e^(14394.744927536234` /T)] -
    4.0626167254066933`*^46 T^3 PolyLog[3, e^(35986.86231884058` /T)] -
    1.1289166277994034`*^42 T^4 PolyLog[4, e^(14394.744927536234` /T)] +
    1.1289166277994034`*^42 T^4 PolyLog[4, e^(35986.86231884058` /T)]))
```

This function is plotted below and represents the relative response of the camera to the Ideal Full Spectrum Detector (ie. Detector Window / Full Spectrum Ratio as F{T(^{o}K)})

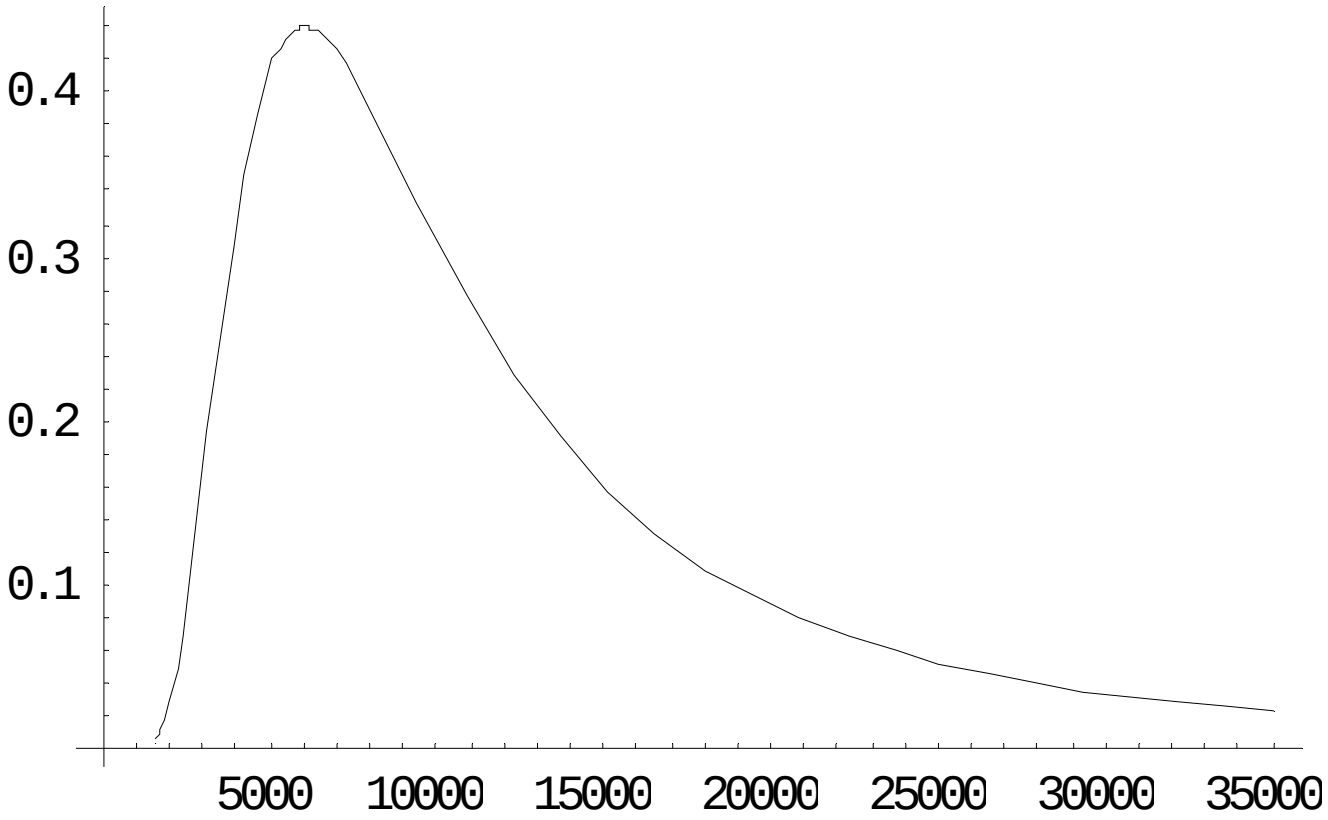

Over the temperature range of interest for SRM ejecta (1500<T<4000 ^{o}K), this function can be approximated by the linear equation:

$$R=0.0002*(T-1600)$$

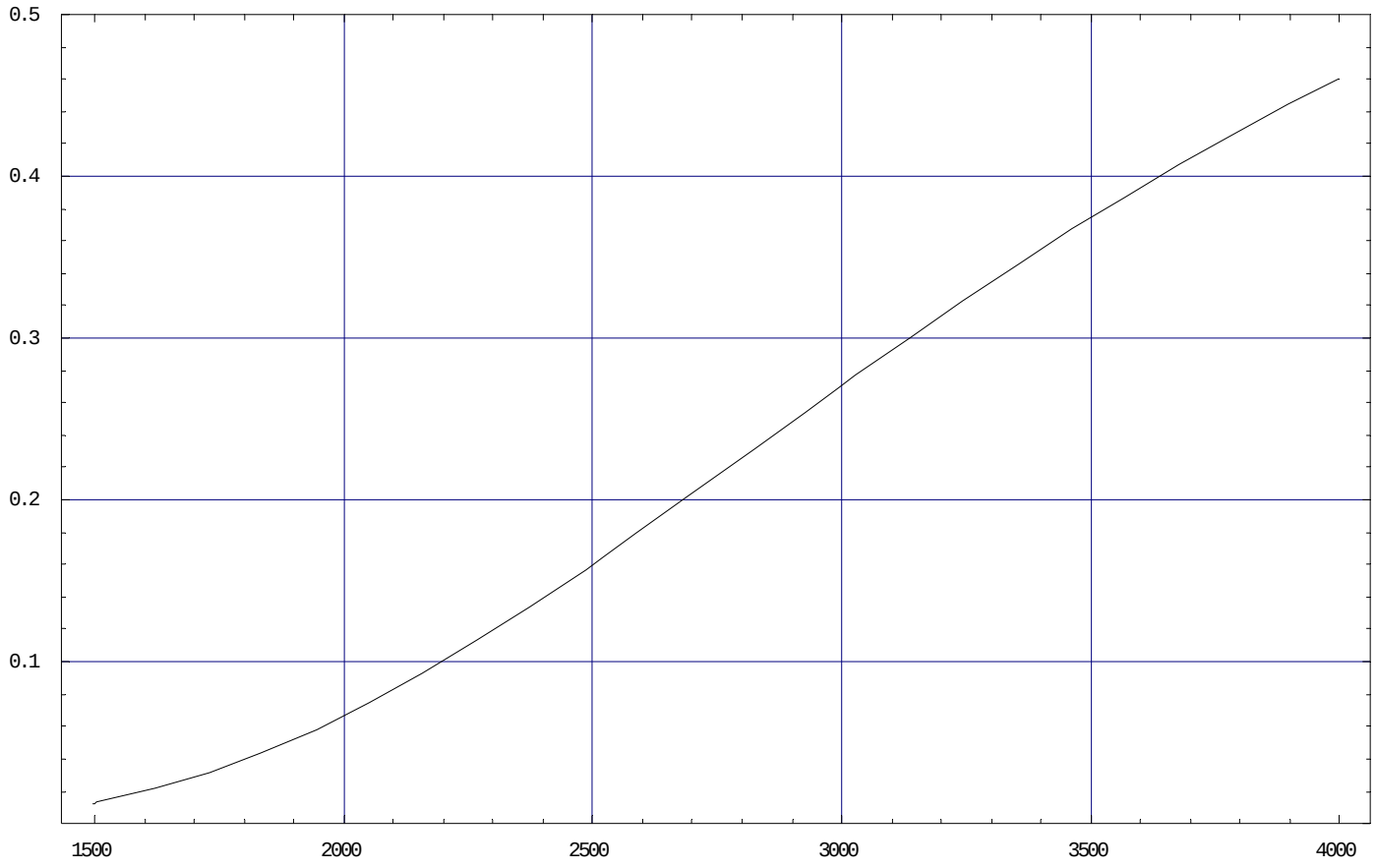

Thus L(t) in the fully time and luminosity dependent case, upon allowing for limited detector response and spectral shift (redward as the object cools) becomes:

$$L(t) = 4\pi r^2 \sigma (3\alpha t + \frac{1}{T_0^3})^{\frac{-4}{3}} \{0.0002[(3\alpha t + \frac{1}{T_0^3})^{\frac{-1}{3}} - 1600]\}$$

Which when plotted for the initial temperature (3500 ^{o}K) of potential SRM Emissions becomes Figure 86:

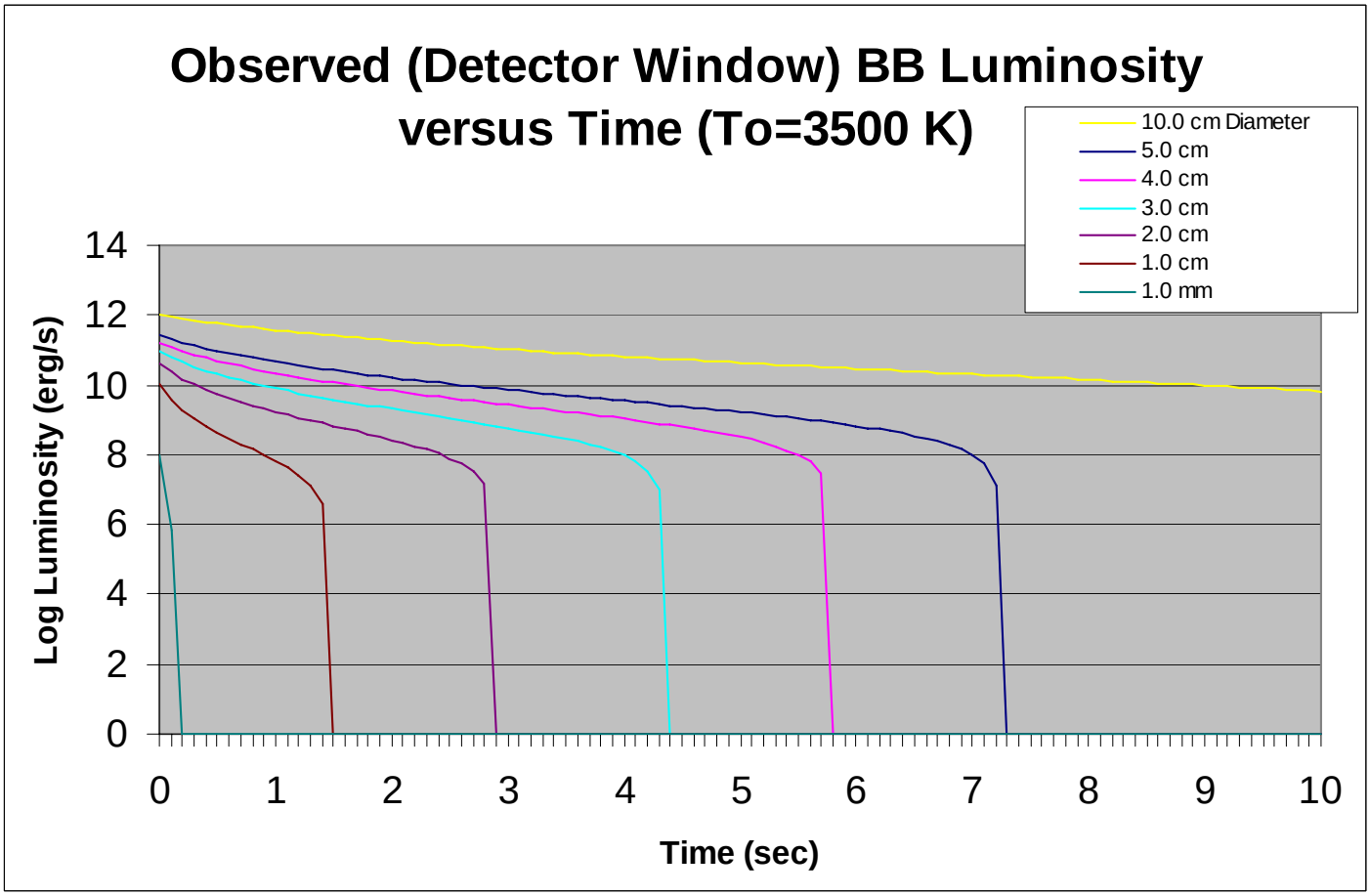

Appendix II

Photometric Calibration and Size Estimates for STS-93 In-situ Video Data

Slag Object luminosities are derived by performing aperture photometry, converting to flux using a calibration source, and then assigning an object distance to get total luminosity. This derived luminosity is then associated with a unique object size in accordance with time of observation post-emission and the BB luminosity function with correction for the limited (windowed) detector response.

Fortuitously, STS-93 in-situ data has a calibration source present – this was a night launche with the moon present in the field of view. This in-situ imagery can be calibrated in the conventional fashion by performing aperture photometry of the moon and then equating that with the lunar flux.

The lunar illumination for a given launch date and time was obtained from http://ssd.jpl.nasa.gov/cgi-bin/eph:

STS-93 Right SRB camera - Moon present, 67% illuminated

The Lunar Flux is given by:

$$F_{Lunar} = F_{Sun} 10^{-0.4(m_L - m_s)}$$

Where:

$$F_{Sun} = 1.73E + 7$$

$$m_{sun} = -26.80$$

The Lunar Apparent Magnitude of -12.70 (m_l)corresponds to a lunar flux (F_{Lunar}) at the earth of:

F_{Lunar} = 39.7 erg/s-cm^2.

The detector was assumed linear and of uniformly (flat) chromatic response from 0.4 to 1.0 μm.
For STS-93, the moon was 67% illuminated, thus the flux at the Right SRB detector was approximately 26.6 erg/s-cm^2. Since the lunar photometric measurements yielded 58,100 counts/frame, the calibration constant is:

STS-93 Calibration Constant: 4.58E-04 erg/s-cm^2-count.

Far-Field Size Estimations

For the measured far field objects associated with the STS-93 Left SRB and observed 14 and 17 seconds after SRB separation, the range was approximately 200 meters (based upon angular separation as viewed from the E222 ground based imagery and angular size/FOV estimations based upon the in-situ SRB data.)

The Brightest object measured in the far field contained 15,420 counts, and thus had a flux at the detector of 7.1 erg/s-cm^2.

At a range of 200 meters, the object luminosity was thus 2.8E+9 erg/sec.
The object was measured 4 seconds after emission from the SRB. Utilizing the time dependent, detector corrected BB luminosity function (Figure 86), this corresponds to an object diameter of 4.0 cm .

A similar calculation for the Faintest far field object (151 counts =>2.7E+7) yields a diameter of approximately 3 cm.
This Lower size limit is constrained by detector sensitivity, but the upper (4 cm) limit is possibly profound in terms of the ostensible upper limit of the size distribution.

To better ascertain the lower size limit, perform the same analysis for the Near Field.

Near-Field Size Estimations

Summary Boundary conditions and results for Right SRB (Near Field) Measurements:

Estimated Range: 1 and 10 m
Estimated Age of particles 4 seconds

Luminosity of Brightest Particle at 10m: 1.3E+8 erg/sec
-> 3 cm Diameter

Luminosity of Brightest Particle at 1m: 1.27E+6 erg/sec
-> ~3 cm diameter

Luminosity of Faintest Particle at 1m: 4.1E+4 erg/sec
-> ~ 3cm diameter (Extremely Age Sensitive)

- So, including all representative particles over all available missions, the photometric analysis of in-situ observations of SRB particulate ejection indicate an approximate size range of: $2 \leq D \leq 5$ cm. A distribution that is clearly appears weighted towards large particulates, but this is possibly an artifact of limited detector sensitivity.